

Picosecond time-resolved transport studies in a two-dimensional electron system

**Von der Fakultät Mathematik und Physik der Universität Stuttgart
zur Erlangung der Würde eines Doktors der Naturwissenschaften
(Dr. rer. nat.) genehmigte Abhandlung**

vorgelegt von

DENIS MARYENKO

aus Kiew, Ukraine

Hauptberichter:	Prof. Dr. K. v. KLITZING
Mitberichter:	Prof. Dr. H. GIESSEN
Tag der Einreichung:	25. Februar 2010
Tag der mündlichen Prüfung:	26. März 2010

**MAX-PLANCK-INSTITUT FÜR FESTKÖRPERFORSCHUNG
STUTT GART, 2010**

Contents

Symbole und Abkürzungen	4
1 Introduction	6
2 Experimental Method and Technique	1
2.1 Metal–Semiconductor–Metal–Switch	1
2.2 Coplanar waveguide	2
2.3 Sampling technique	4
2.4 Experimental setup	5
2.5 Experiments on pulse propagation along CPW	6
2.5.1 CPW with a bent parasitic waveguide	8
2.6 Sample Design	10
2.7 Coplanar waveguide with four switches	13
3 DC-Experiment	19
3.1 Introduction	19
3.2 Quantum Point Contact	19
3.3 Caustic	20
3.4 Transverse magnetic focusing device	21
3.5 Corner Device	23
3.6 Experimental results	24
3.7 Numerical transport simulation in disorder-free landscape	28
3.8 Numerical transport simulation in disordered landscape	29
3.9 Comparison of experimental results with simulation	31
3.10 Ballistic cavities	33
4 Time Resolved Experiments	39
4.1 Time-dependent measurement on a corner device	39
4.1.1 Gate defined corner device	39
4.1.2 Etched corner device	40
4.2 Time-dependent transport on a stripe of the 2DES	44
4.2.1 Plasmon modes in 2DES	46
4.2.2 Fourier spectrum	48
4.2.3 140 μ m long stripe	56
4.3 Pulse propagation velocity in a stripe	62

4.4	Temperature dependence	64
5	Correlation of electrical pulses on a 2DES	67
5.1	Idea behind the electrical pulse correlation technique	67
5.2	Correlation in magnetic field	69
5.3	Excitation spectrum	73
6	Summary and Outlook	75
A	Calculations for CPW	87
B	Fiber Alignment and Gluing	89
C	Sample Fabrication	91
C.0.1	Mesa definition	91
C.0.2	Ohmic contacts	92
C.0.3	Alignment marks for ebeam lithography	93
C.0.4	Pads	93
C.0.5	Coplanar waveguide	94
C.0.6	Three-chip assemble	94
	Acknowledgements	103

Symbol table

2DES	two-dimensional electron system
B	strength of the magnetic field
CF	composite fermion
CPW	coplanar waveguide
LT-GaAs	low temperature grown GaAs
MSM switch	metal-semiconductor-metal switch
TMF	transverse magnetic focusing
QPC	quantum point contact
c	velocity of light in vacuum
E_F	Fermi energy
ω_c	electron cyclotron resonance frequency
ω_p	plasmon frequency in zero magnetic field
ω_{mp}	magnetoplasmon frequency in the magnetic field

Chapter 1

Introduction

The discovery of the Integer and Fractional Quantum Hall Effects [1, 2] inspires the research in semiconductor electron systems confined to two dimensions already for 30 years. While a picture of non-interacting electrons is sufficient to explain the Integer Quantum Hall Effect (IQHE) [3,4], electron-electron interaction effects are essential for the Fractional Quantum Hall Effect (FQHE) [5]. For an intuitive understanding of the FQHE, J. Jain introduced the concept of Composite Fermions [6]. These are quasi-particles, each of which is assembled from one electron and two magnetic flux quanta pointing opposite to the perpendicularly applied magnetic field. Within this framework, the FQHE can be understood as the IQHE of Composite Fermions (CF) in an effective magnetic field, which is zero at the Landau level filling factor $1/2$. Furthermore, Halperin et al. predicted the existence of the Fermi surface for CFs [7]. This led to the experiments which are analog to the experiments for the electron systems at low magnetic field; the commensurability oscillations in periodic structures and transverse magnetic focusing for CFs were demonstrated [8, 9]. Composite Fermions precess, like electrons, along circular cyclotron orbits with a diameter given by the effective magnetic field. The frequency of the cyclotron motion is determined by the effective mass, which is no longer related to the conduction band properties of the host material, but is governed entirely by Coulomb interactions. Kukushkin et al. devised an experiment to measure the cyclotron resonance for CFs, from which the effective mass could be extracted [10].

An alternative approach to measure the mass of CFs is to perform time resolved transport experiments for CFs in ballistic regime. The measurement of the transit time in a well defined structure, e.g. transverse magnetic focusing device, provides information about the quasi-particle dispersion, Fermi velocity and mass. For samples based on the well established GaAs/AlGaAs heterostructure such measurements require subkelvin temperature and high magnetic field. Furthermore, the transient time of CFs in transverse magnetic focusing device is expected to be on the order of 10 ps. Therefore, the experimental arrangement for time resolved transport experiment has to fulfill several requirements:

- picosecond time resolution in order to access the characteristic transit time scales
- compatibility with the cryogenic environment
- applicability of high magnetic field.

These requirements exclude all-electronic means and the use of the coaxial cables. They are, however, conformed when using an all-on-one-chip photoconductive sampling technique. Here, we make use of photoconductive switches that are operated by femtosecond laser pulses guided via optical fibers. The switches are positioned in the vicinity of the device under study and act as a source of electrical pulses as well as a detector of the ultrafast signal that probed the device under study. Propagation of the pulses proceeds across a coplanar waveguide.

This thesis is an intermediate step toward ballistic time resolved transport experiments for CFs and ties in with the work of our predecessor Martin Griebel [11], who worked out the photoconductive sampling technique in our group. The scope of the thesis reaches from the introduction and the demonstration of the photoconductive sampling technique, over DC transport experiments in several ballistic devices, which are suitable for time resolved studies, to the application of the time resolved photoconductive sampling technique to investigate the excitation of the two-dimensional electron system.

The thesis is organized into four main chapters:

- **Chapter 2** Photoconductive sampling technique is the basis for the time resolved transport experiments. We introduce the photoconductive switches which are used to generate short electrical pulse and to detect the ultrafast signal. We demonstrate that the electrical pulses can be launched into the coplanar waveguide and be detected several millimeters away from the source.
- **Chapter 3** We perform DC transport experiment on ballistic devices, which can be employed for ballistic time resolved experiments. These devices are corner device and different cavity geometries. A large part of the chapter is devoted to the experiments in the corner device, as it has surprisingly allowed to observe the branched electron flow in a conventional DC transport experiment.
- **Chapter 4** Time resolved transport experiments are performed in a corner geometry and on a stripe of a two-dimensional electron system. We observed the excitation of various modes of magnetoplasmon and measured the pulse propagation velocity in the stripe. The experiments are performed for stripes of different length and for two values of electron density in the stripe.
- **Chapter 5** Another measurement method for time resolved studies is electrical pulse correlation measurement. To our knowledge, this method is applied for the first time in two dimensional electron system to probe its non-linearity.

Chapter 2

Experimental Method and Technique

This chapter introduces and explains in an intuitive way the sampling technique that is employed for the time-resolved measurements. In particular, a photoconductive switch, which acts both as a source of the short electrical pulses and as a detector, is briefly discussed. Thereafter a short discussion on a waveguide, which facilitates the propagation of a terahertz broadband signal over distances of several millimeters, is enclosed. It is followed by the demonstration of the sampling technique to detect the pulse propagation along the waveguide with integrated photoconductive switches. Finally, arguments are brought forward for and against different approaches to integrate the two dimensional electron gas into the waveguide geometry.

2.1 Metal–Semiconductor–Metal–Switch

An ultrafast metal-semiconductor-metal (MSM) switch ([12, 13, 14]) is a configuration consisting of two electrodes structured on top of a photoconductive material. The light shining on the gap between the electrodes excites electrons into the conduction band and holes in the valence band. The transient current starts flowing through the switch when a voltage is applied across the switch (Fig. 2.1). The time span over which the electrical current persists sets, obviously, the duration of the electrical pulse. To find the process which governs the pulse duration several time scales have to be compared among each other. One of them is the optical pulse duration, since the current can at least persist as long as the electrons are being excited into the conduc-

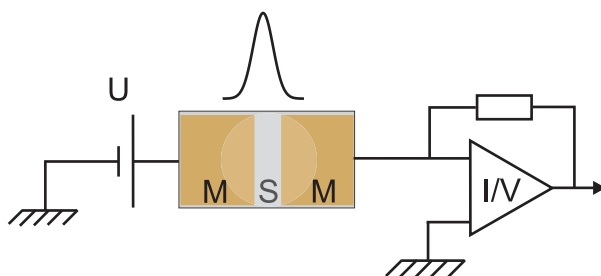


Figure 2.1: Schematic of a metal-semiconductor-metal switch and the electrical circuit to characterize it. Typical experimental parameters are: gap between electrodes $3 \mu\text{m}$, width of the electrodes $20 \mu\text{m}$, applied bias voltage 10 V and optical power 1 mW.

tion band. Because of a capacitive coupling between the electrodes the RC-time of the capacitor discharge needs to be considered as well. Another important time scales are the electron life time and the transient time to cross the switch. If the distance between the electrodes is so small that the electrons can drift from one electrode to the other within their life-time, then this switch is called transient-time limited switch [15, 16]. If this condition is not met, the current will disappear because the electrons are captured by impurities or get trapped at predefined structures. These switches are referred to as life-time limited switches. Note that the electron-hole recombination time can be up to nanoseconds in high quality semiconductors. Short life-times are only obtained in defect rich materials. For our experiment the electron capture time dominates the other time scales. The life-time limited switches have several advantages. They are structured with optical lithography, which makes them robust against electrostatic discharge. In contrast, the other types of switches involve usually an e-beam lithography step and thus these structures are more sensitive to electrostatic discharge. The operation of a life-time limited switch is independent of an applied magnetic field, while the operation of a transit-time limited switch is affected by the magnetic field.

Two photoconductive material systems were available for the experiments at 800 nm wavelength; they are GaAs grown at low temperature (LT-GaAs) and GaAs with periodically embedded layers of ErAs islands (ErAs:GaAs). GaAs grown at low temperature contains a lot of defects, which are arsenic clusters embedded inside GaAs semiconductor matrix ([17, 18]). These clusters act as traps for the electrons in the conduction band. The growth temperature of GaAs and the subsequent annealing step determine the electron life time in the material. The low temperature control during growth is however difficult and challenges the grower to achieve reproducible results. The ErAs:GaAs material system offers a better control over the electron life-time. Similar to the arsenic clusters in LT-GaAs, the layers of ErAs islands periodically incorporated into the GaAs matrix assume the role of the electron traps. The distance between the adjacent layers of ErAs controls the electron life time. Its tunability from about 400 fs up to 5 ps was reported by Griebel et al [19]. For the experiments at 1550 nm wavelength $\text{In}_{0.57}\text{Ga}_{0.43}\text{As}$ can be used as the semiconductor matrix instead of GaAs. The life time tunability by controlling the period of the ErAs:InGaAs superlattice was reported for this material by Ospald et al [20] and Driscoll et al [21].

For time-resolved studies the short electrical pulses must be delivered to the active device. As the typical duration of an electrical pulse can be on the order of 1 ps or even less, its spectral content covers the terahertz frequency range. A waveguide type that operates with acceptable dispersion for this spectral bandwidth is the so called *coplanar waveguide*.

2.2 Coplanar waveguide

Though there are several different types of waveguides that can conduct a signal at frequencies up to the terahertz range, the coplanar waveguide (CPW) offers the best trade-off between dispersion, damping properties and ease with which it can be integrated into the circuit and fabricated. Reference [22] gives more details on the properties of the coplanar waveguides. The coplanar waveguide (Fig. 2.2) consists of a conducting central line of width s and ground planes separated by a distance w on both sides of the central conductor. Those planes shield the propagating wave from the environment to some extent and thus lower its damping. Additionally,

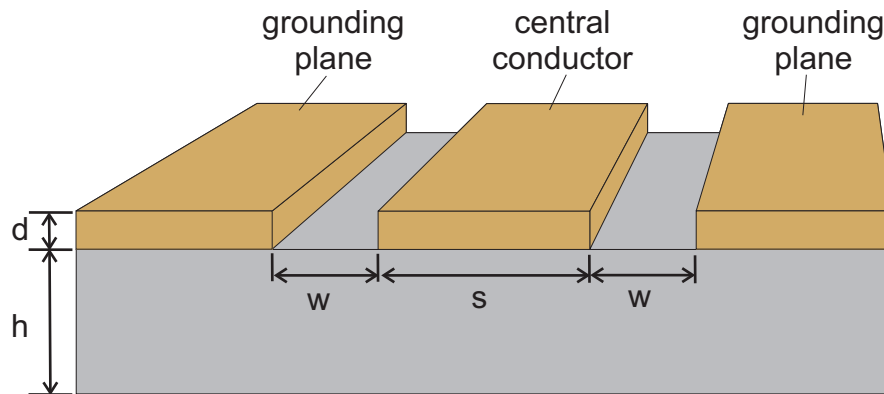


Figure 2.2: Schematic of a coplanar waveguide. h is the substrate thickness, d is the thickness of the evaporated metal. The waveguide dimension used in the experiments are $d = 300$ nm, $s = 20$ μm , $w = 10$ μm .

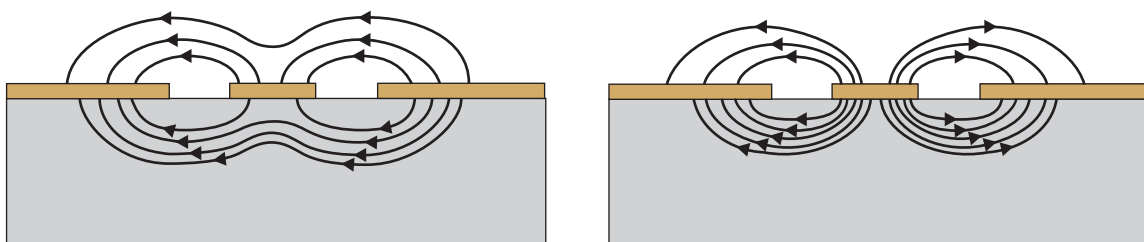


Figure 2.3: A coplanar waveguide supports two types of principal modes. They differ by the symmetry of the electrical field with respect to the central conductor of the CPW. a) Electric field lines of the slotline mode (even mode). b) Electric field lines of the CPW mode (odd mode)

because of its geometry the coplanar waveguide supports two types of principal modes: the desired quasi-TEM CPW mode (odd mode) and a parasitic slotline mode (even mode). They differ by the symmetry of the electric field with respect to the CPW's central conductor (Fig. 2.3). The characteristic dimension for the even mode is the distance between the two ground planes, while the odd mode's characteristic dimension is the distance between each ground plane and the central conductor. Because of its larger spatial distribution the even mode is subject to a stronger dispersion and damping than the odd mode. Since the two modes have different propagation characteristics, any asymmetry or discontinuity in a CPW structure that mixes the modes causes distortions and thus alters the pulse shape. The dispersion on a CPW, which mostly consists of quasi-static $\frac{\omega}{c} \sqrt{\epsilon_{qs}}$ and modal dispersion $\frac{\omega}{c} \sqrt{\epsilon_{mod}}$, also affects the shape of the propagating pulse [11]. Appendix A contains calculations for both types of dispersion. Quasi-static dispersion dominates for signals, whose wavelength is larger than the lateral dimension of the CPW, while the modal dispersion becomes important for higher frequencies. When an electromagnetic wave propagates on a CPW, the electric fields above the conducting layers experience the permittivity of the air, while those below the conductors experience the permittivity of the substrate. The effective permittivity thus takes on a value in between that of air and substrate. When the frequency of the propagating wave increases, the effective permittivity approaches that of the substrate $\sqrt{\epsilon_r}$, as the density of electric field lines below the conducting layers increases. This stronger binding of the electrical field lines to the substrate at higher frequencies is the origin of modal dispersion. Figure 2.4 shows $\sqrt{\epsilon_{qs}} + \sqrt{\epsilon_{mod}}$ for 20 μm and 40 μm width of the CPW's central conductor. The pulse dispersion during the propagation along the CPW limits the time resolution in the propagation experiments. Since the electrical pulses generated with the photoconductive switch have frequencies up to 1 THz and more, CPW with a width smaller than 20 μm are needed to avoid excessive dispersion. For practical reasons the CPW with a 20 μm wide central conductor is a suitable geometry.

2.3 Sampling technique

We considered so far how to create short electrical pulses and introduced a waveguide which can propagate the pulse. To wind up the introduction of the main tools the detection scheme of the signal needs to be discussed. Fortunately, a photoconductive switch can also be employed as a detector. However, in contrast to a pre-biased source switch, the electrodes of the detector switch are grounded; one is grounded directly, the other is grounded via a current-voltage converter. Even though an optical pulse, which illuminates the grounded MSM switch, excites the electrons into the conduction band, no current flows because of the absence of an electric field across the switch. However, once an electrical signal passes the detector switch, it changes the local electrostatic potential on the electrode of the illuminated detector. The current, which flows then across the switch, depends on the amplitude of the passing signal. In case that an electrical signal passes a non-illuminated switch, no current flows across the switch because there are no carriers available in the conduction band. This allows for a time-resolved measurement of the signal. To measure the signal at later times the optical pulse, that gates the detector switch, has to be delayed. Hence, the shape of the transient signal reaching the detector switch is sampled in time by delaying the incident optical pulse.

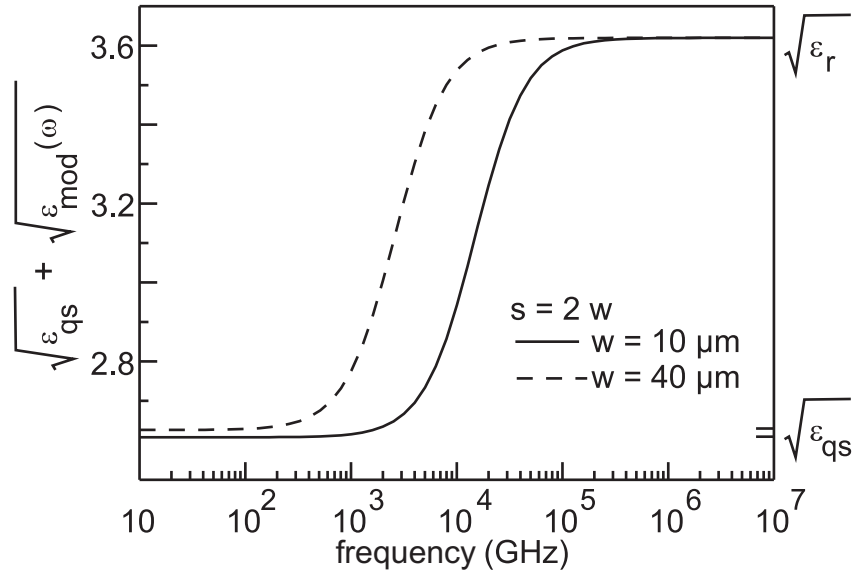


Figure 2.4: $\sqrt{\epsilon_{qs}} + \sqrt{\epsilon_{mod}(\omega)}$ as a function of frequency for two coplanar waveguides with a different width of the central conductor. This dependence accounts for the pulse broadening during the propagation along CPW.

2.4 Experimental setup

The optical setup shown in Fig. 2.5 enables the realization the sampling of the fast electrical pulses. The use of optical fibers is helpful to implement the sampling technique in a cryogenic environment with high magnetic fields. The optical fibers guide the optical pulses toward the photoconductive switches. More details about the setup are given here.

Two short pulse laser sources are available for our propagation experiments: a Ti:Sa laser operating at 800 nm is suitable for use with GaAs based materials and a fiber laser operating at 1550 nm for InGaAs based materials. The Ti:Sa laser has a repetition rate of 76 MHz. The outgoing pulses are horizontally polarized and their duration is on the order of 150 fs. To compensate for the pulse dispersion in the fiber, that guides the pulses to the switch, a Grating Dispersion Compensator (GDC) is used to impose a negative dispersion onto the pulses. The stretched pulses are split in two pulse trains with a beam splitter. One pulse train follows a trajectory that contains a shaker (retroreflector vibrating at a fixed low frequency). It produces an oscillating delay between the pulse trains of up to 50 ps. The other pulse train follows a trajectory that contains a retroreflector positioned on a stepper motor. This arrangement can introduce an additional delay of up to 2 ns. Each of these pulse trains is coupled into the optical fiber¹. The adjustment of the GDC proceeds by optimizing the pulse duration measured at the fiber's end. The pulse duration is measured with the help of a commercial autocorrelator². The fiber laser³ with a repetition rate of 72 MHz operates at a central wavelength of about 1550 nm. The outgoing pulses are prechirped to compensate for a dispersion in a roughly 5 m long fiber. Since the total fiber length amounts to 8 m, an additional compensation needs to be introduced. The

¹purchased from Thorlabs, Fiber Type HP780

²purchased by APE-Berlin

³Menlosystem GmbH

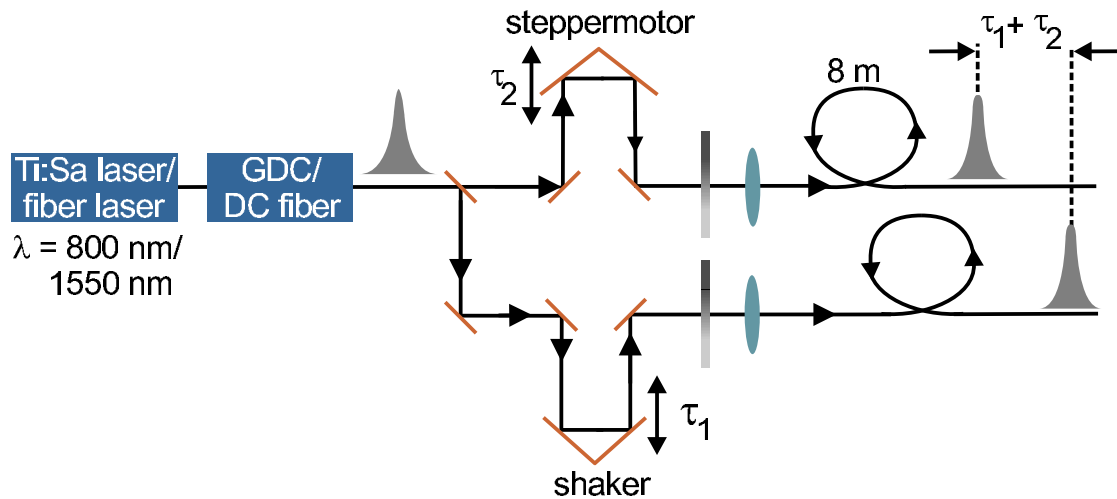


Figure 2.5: Optical setup for time-resolved transport experiments. A grating dispersion compensator (GDC) or a dispersion compensating fiber (DC fiber) imposes a negative dispersion on the optical pulse train coming from a Ti:Sa or fiber laser correspondingly. They allow to compensate the dispersion of an 8 meter long fiber needed to run the optical pulses from the optical set-up to the cryostat. The pulses run in a modified Mach-Zehnder interferometer and are coupled into the optical fiber. The shaker in one of the interferometer arms oscillates at low frequency and spans a delay time τ_1 on the order of 50 ps. The stepper motor in the other arm can produce an additional delay between both interferometer arms of up to 2 ns.

use of the dispersion compensating fiber (DC-fiber) is an elegant way to design a dispersion compensating scheme in the infrared region. The DC-fiber imposes a negative dispersion on the pulses. Therefore, the adjustment of the fiber lengths with normal and negative dispersion relative to each other controls the final pulse duration. In the experimentally designed compensation scheme the DC-fiber is connected directly at the laser output. Thereafter, the pulses run in the optical setup described above, whose components are optimized for the infrared wavelength. And finally, the pulses couple into the fibers with normal dispersion. Note, the fiber length may not be varied much, since the compensation scheme is optimized only for a fixed fiber length.

To equate the length of the optical arms the pulse trains from both fibers are detected on a fast photodiode with 12 GHz bandwidth; its signal is displayed on a real time oscilloscope with 4 GHz bandwidth. The overlap of two pulse trains with a precision of better than 50 ps is achieved by changing the position of the stepper motor.

2.5 Experiments on pulse propagation along CPW

One possible CPW configuration with embedded photoconductive switches is shown in Fig. 2.6a. The optical fibers are coupled to the switches as described in Appendix B. A DC-voltage is applied across the left switch. It serves as the source of the electrical pulses. The right switch assumes then the role of the detector. It is grounded via the current-voltage converter. The

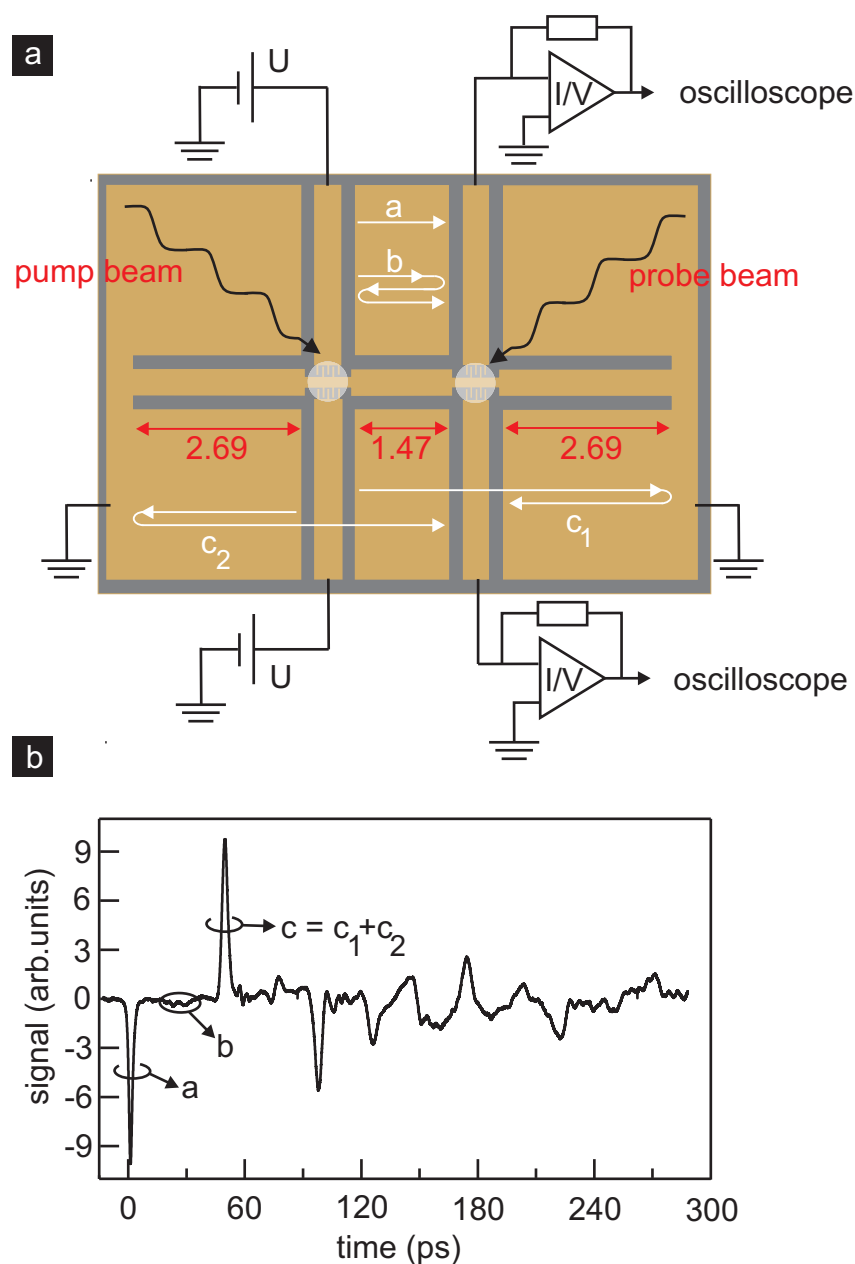


Figure 2.6: a) A coplanar waveguide arrangement with integrated switches. The width of the central conductor $w = 20 \mu\text{m}$, the distance to the ground planes $s = 10 \mu\text{m}$. The voltage is applied to the left switch. This switch acts as a source of short electrical pulses. The right switch assumes the role of the detector, whose signal is output on an oscilloscope. Also shown are the pulse paths, which are associated with the peaks of the trace presented in panel b. b) The pulse propagation trace along the coplanar waveguide. The peaks denoted (a), (b) and (c) correspond to pulse pathes drawn in panel a.

signal from the converter is visualized on an oscilloscope. The oscilloscope is triggered on the shaker's reference signal, which is fed into another oscilloscope channel. The amplitude of the shaker displacement is reflected in the amplitude of the reference signal and defines the time axis of the experiment. Therefore the signal displayed on the oscilloscope screen spans over the time interval given by the amplitude of the shaker oscillation. To increase the signal to noise ratio the signal is averaged over several oscillation cycles of the shaker. To monitor the signal at another time interval the stepper motor position can be changed to introduce a fixed extra delay. The traces at different positions of the stepper are concatenated and are shown as a single trace in Fig. 2.6b. The first pulse (a) is the result of direct pulse propagation from the source to the detector switch. The switches are separated by 1.47 mm. The next feature (b) appears at a delay time of 30 ps and is caused by the reflection between the photoconductive switches as shown in Fig. 2.6a. A more pronounced peak (c) appears at 49.8 ps and is attributed to the reflection at the short circuited end of the parasitic waveguide with length 2.69 mm (trajectories c_1 and c_2 in Fig. 2.6a). The peaks which appear at later times arise from the multiple pulse reflections while propagating along the CPW. This interpretation is adopted from the work of Griebel [11], who performed similar pulse propagation experiments on a CPW fabricated on GaAs-based photoconductive material. Figure 2.6 a shows that the amplitude of the reflection peaks, for instance the amplitude of peak (c), is comparable to the amplitude of the first peak. In time-resolved magnetotransport experiments the reflected peaks can cause a multiple excitation of the active device which then complicates the data interpretation. Therefore it is desirable to search for a solution where reflections are avoided or reduced in amplitude as much as possible.

2.5.1 CPW with a bent parasitic waveguide

In a geometry with a bent central conductor, as shown in Fig. 2.7, the amplitude of the reflections is reduced compared to the geometry with a straight central conductor. Indeed, the trace measured on this geometry is depicted on the positive part of the time axis in Fig. 2.8a and shows only the small peaks (b) and (c) at 59.3 ps and 96.4 ps correspondingly. The first peak

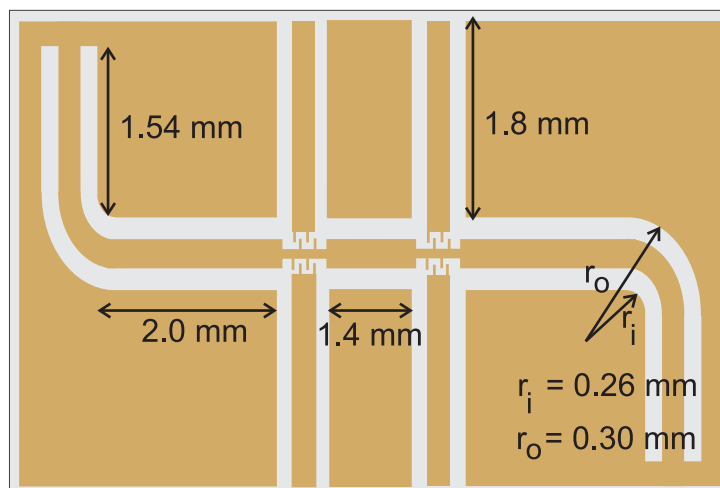


Figure 2.7: Schematic of a CPW in which the total length of the central conductor has been increased by introducing two bends.

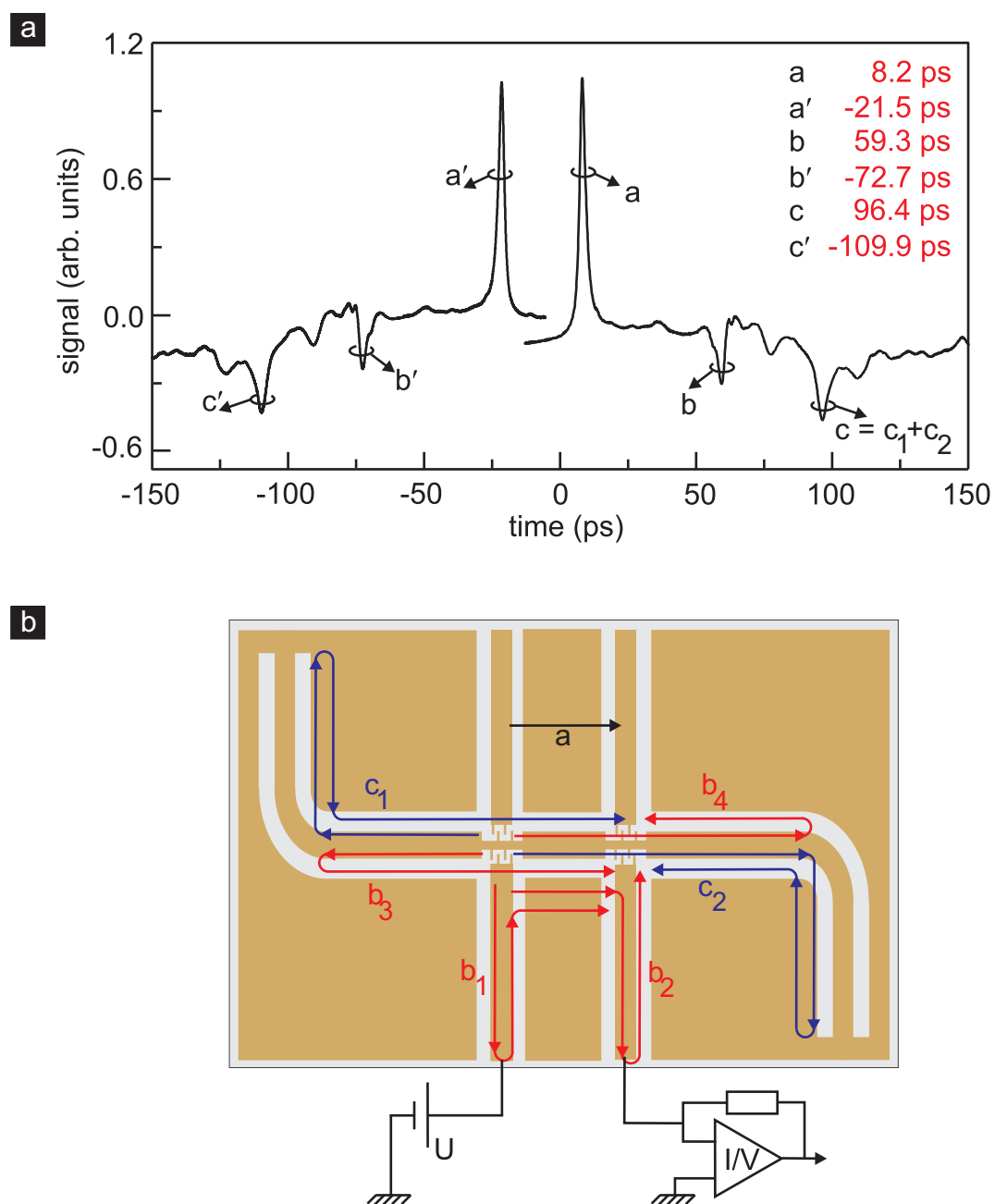


Figure 2.8: a) Pulse propagation traces on the CPW with bends shown in panel b. The bias voltage on the switch is -2 V and the optical power of the pump and probe beam is 0.8 mW. For the trace going to the right the left switch acts as a source, while the right switch is used as a detector. For the trace going to the left the role of the switches is swapped. The zero time point on this axis is chosen arbitrarily. b) Pulse paths associated with the peaks denoted a, b, c in the trace in panel a.

(a) positioned at 8.2 ps is the result of direct pulse propagation from the source switch to the detector switch (trajectory a in Fig. 2.8b). This trace is obtained for the case when the left switch acts as a source and the right as a detector. Note, the zero time point is chosen arbitrarily and is given only by the position of the steppermotor at the beginning of the experiment.

For the interpretation of time-resolved experiments it is beneficial to know the propagation velocity along the waveguide. The value of the velocity alleviates also the identification of the reflection peaks. This is achieved by exploiting the system's symmetry. For this, the roles of the switches are exchanged, i.e. the right switch acts as a source, and the signal is monitored at the left switch. Note, for this experiment only the DC-bias source and the current-voltage converter are exchanged. Neither the optical setup nor the fibers are modified in any way. The trace of this experiment is plotted on the same time axis as the previous experiment and goes to the left along the time axis in Fig. 2.8a. For this inverse pulse propagation the symbol "/" is attached to the peak labels in the propagation trace. The first peak (a') positioned at -21.5 ps corresponds to the direct pulse travel from the source to the detector. The time difference between the peaks (b') and (a') is the same as between the peaks (b) and (a). The same holds for the other features in both traces. Therefore the outcome of both experiments is essentially identical and the CPW does not exhibit any preferred direction for pulse propagation. This fact yields immediately the zero time point; the time when the optical pulse trains arrive simultaneously at both switches. Since peak (a) appears at 8.2 ps and peak (a') appears at -21.5 ps, the zero time point lies in-between at -6.65 ps. The distance between the switches is 1.4 mm and therefore the propagation velocity amounts to $0.315c$, where c is the velocity of light in vacuum.

While propagating along the waveguide the pulse reflects wherever the impedances are not matched. This might be a short circuited end of the waveguide, an open end of the side arms etc. A reflection in the waveguide appears as an additional peak in the propagation trace. The peaks (b),(b') and (c),(c') in Fig. 2.8a can be attributed to reflections along the waveguide. Here we try to identify the location where reflection takes place. The pulse trajectories, which reflect at the open end of the waveguide, are labeled as b_1 and b_2 in Fig. 2.8b. Their length is 5 mm each. It takes 53 ps to travel this distance. The bend in the waveguide may also cause pulse reflection. The corresponding pulse trajectories are labeled b_3 and b_4 . Their length is 5.4 mm and it takes 57 ps to travel this distance. Peak (b) in Fig. 2.8a appears at $59.3 \text{ ps} + 6.6 \text{ ps} = 65.9 \text{ ps}$ when taking into account the zero time point. In the simple picture of pulse trajectories neither trajectories b_1/b_2 nor b_3/b_4 can explain the appearance of peak (b). Further, if the pulse reflects on the short circuited end of the waveguide it travels paths c_1 or c_2 . The length of each of the trajectories is 9.35 mm and it takes 98 ps to travel it. Peak (c) in Fig. 2.8a appears at 102 ps when taken into account the zero time shift. The deviation from the experimental value is only 2% and thus peak (c) can be thought as a composition of trajectories c_1 and c_2 , which are shown in Fig. 2.8b.

2.6 Sample Design

To perform the time-resolved studies on a two-dimensional electron gas, it is necessary to combine the photoconductive material, on which the photoconductive switches are patterned, with the GaAs substrate containing the 2DES. This can be accomplished in several ways.

One of the approaches starts with the epitaxial growth of either LT-GaAs or an ErAs:GaAs

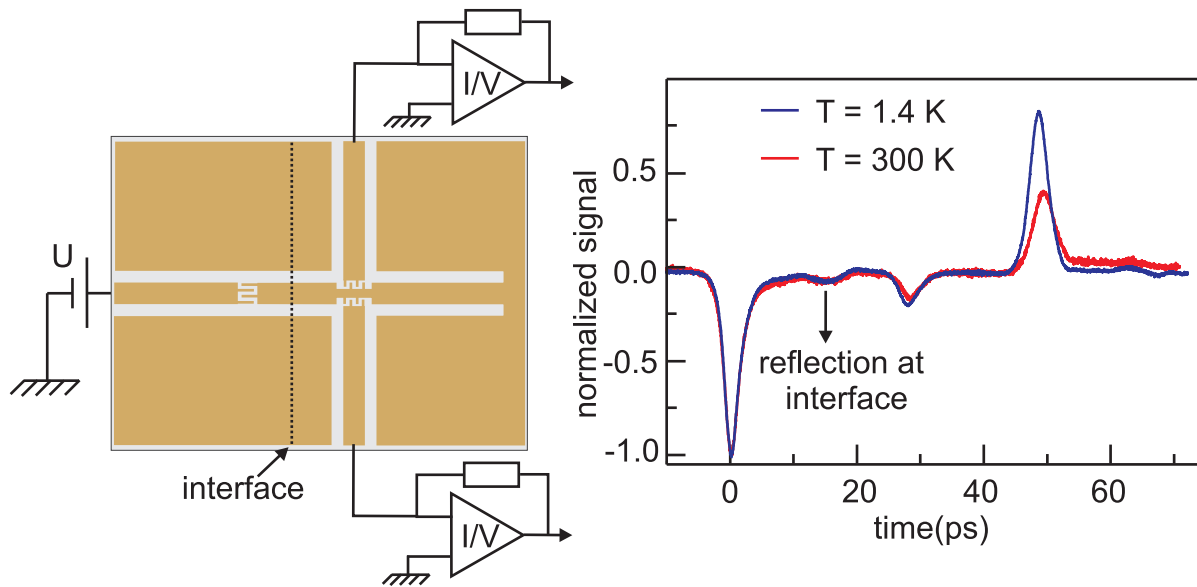


Figure 2.9: CPW scheme with integrated photoconductive switches to study the pulse propagation across the interface (dashed line). Electrical contact between the two halves of the CPW is established by applying silver epoxy droplets between the corresponding parts of the CPW. The right panel compares the pulse propagation traces at room and at low temperatures. The feature around 15 ps is attributed to the reflection at the interface.

superlattice. On top of these photoconductive materials a heterostructure, which contains the 2DES, is grown. This monolithic approach is difficult. The properties of LT-GaAs will change during the heterostructure growth. During the growth the temperature is high and the LT-GaAs will be effectively annealed. This leads to a prolonged electron life time in LT-GaAs. If alternatively the heterostructure is grown on top of ErAs:GaAs layers, the quality of the heterostructure is limited by the achievable quality in a system that contains erbium. However, since high quality 2DEGs are fabricated using the GaAs/AlGaAs heterostructure and to keep the lattice mismatch to a minimum between the heterostructure and the photoconductive material, this approach is limited to GaAs-based photoconductive materials and thus to the operating wavelength of 800 nm. The other two approaches are also limited to the 800 nm operating wavelength. They are described briefly here:

- one etches a mesa containing the high-mobility 2DES based on GaAs/AlGaAs heterostructure. After the mesa is covered with a protecting layer, the sample can be overgrown then either with LT-GaAs or ErAs:GaAs.
- Instead of etching and overgrowth steps, ion implantation into the high-mobility material can be considered to reduce the electron life time in the material. However, the ions have to be implanted at high energies in order to achieve an implantation depth of roughly $1 \mu\text{m}$. This depth is desirable as the characteristic absorption length for GaAs at 800 nm is on the order of $1 \mu\text{m}$. If the implantation depth is smaller than $1 \mu\text{m}$, then the 800 nm light will also be absorbed in the defect-free material with a long electron life time. This could cause a long tail in the electric transient pulse.

To overcome the limitation of using only GaAs-based photoconductive materials, we follow in this work a more elegant way to combine GaAs/AlGaAs heterostructure and photoconductive material. Here, the active device based on a 2DES is fabricated on a heterostructure with a subsequent structuring of CPW, which leads to the device. Separately from this processing step the photoconductive switches and the waveguide are structured on a photoconductive material. Thereafter the chip with a photoconductive material is cleaved and the active device is placed between the two halves. The coplanar waveguide is aligned at the interface between the separate chips and the corresponding part of the coplanar waveguide are contacted by applying silver epoxy. This enables a reflection-free [23] electrical pulse propagation across the interface. Since the device under test is placed between two photoconductive materials, this assembly is addressed as a three-chip configuration. The technical details on this configuration are summarized in Appendix C. This configuration is flexible in the choice of the optical wavelength. In fact, a replacement of ErAs:GaAs with ErAs:InGaAs enables a quick change of the working wavelength and partially solves the problems with the 2DES arising from the illumination of the photoconductive switches with the 800 nm wavelength⁴. Such a three-chip configuration is also flexible on the choice of the device under test; it might be a material which is different from a GaAs/AlGaAs-heterostructure containing the 2DES. The only restriction is that the dielectric constant of this material is comparable to that of GaAs.

The next experiment demonstrates that electrical pulse propagates across the interface between two separate chips without substantial reflections. To simplify the experiment only two chips are used: one containing the source switch, the other the detector switch. Since this experiment was done in the early stage of this work the photoconductive switches are integrated differently into the CPW as shown in Fig. 2.9a. The coplanar waveguide is cleaved in two halves between the switches as the dashed line in panel a shows schematically. Thereafter the two halves are brought together and the silver epoxy droplets are applied between corresponding parts of the waveguide to provide electrical contact. The experiments are performed for fiber coupled photoconductive switches at room temperature and at 1.4 K temperature. For comparison of both traces at different temperatures the signal is normalized to the amplitude of the first peak. The first peak at zero time is the result of direct pulse travel from the source to the detector switch. A small peak around 15 ps is caused by the reflection at the interface. Note that the relative intensity of this peak does not change as the sample is cooled down. This shows that the transmission properties of the interface are stable with temperature. The peak at 28 ps is due to pulse reflection between the switches [11]. The peak at 50 ps is due to pulse reflection at the short circuited end of the coplanar waveguide. The data show that for these reflections requiring larger travel distances the relative peak intensity grows as the sample is cooled. This indicates that damping due to ohmic losses is lower at lower temperature. Other peaks involve multiple reflections along CPW.

⁴The later experiments showed an influence of the scattered 800 nm light on the electron density. Additionally the scattered 800 nm light caused a leakage current between the 2DES and the top gates evaporated on top of the mesa. The leakage current disappears when one works with 1550 nm laser light.

2.7 Coplanar waveguide with four switches

There are several configurations how the photoconductive material and the active device can be combined. One of them is the reflection configuration, where the active device is positioned on one side of the photoconductive switches. In this configuration both the incident signal on the device and the reflected signal from the device can be monitored. The other is the transmission configuration, where the active device is positioned in between the switches. Here, only the transmitted signal, which has passed through the device, can be monitored. In order to measure both reflected and transmitted signals a more complex configuration with two switches on one side and one switch on the other side of the device should be implemented. However, for increased flexibility two switches are positioned on each side of the device. Such a coplanar waveguide with four photoconductive switches is shown in Fig. 2.10. For this geometry, a total of four fibers, one for each switch, are glued on top of the sample. To monitor all signals simultaneously, an extension of the optical setup with extra delay lines would be necessary. This is, however, not pursued in this work. Instead, the signals at every detector switch are monitored successively. The switches are denoted as switch 1, 2, 3 and 4 as shown in Fig. 2.10.

The first experiment involves switches 1 and 2 acting as the source and the detector respectively. The experimental outcome is depicted in panel a of Fig. 2.11 on the positive direction of the time axis. The role of the switches is swapped for the trace plotted along the negative part of the time axis. The time axis is shifted so that the traces are positioned symmetrically with respect to the zero time point. The peaks (a) at 12.4 ps and (a') at -12.4 ps correspond to direct pulse propagation from the source to the detector (trajectory a in Fig. 2.11b). From these first peaks we deduce a propagation velocity of $0.32c$. This velocity is the same as in the CPW arrangement with two switches. The reflection peak (b) appears at 48 ps, which corresponds to

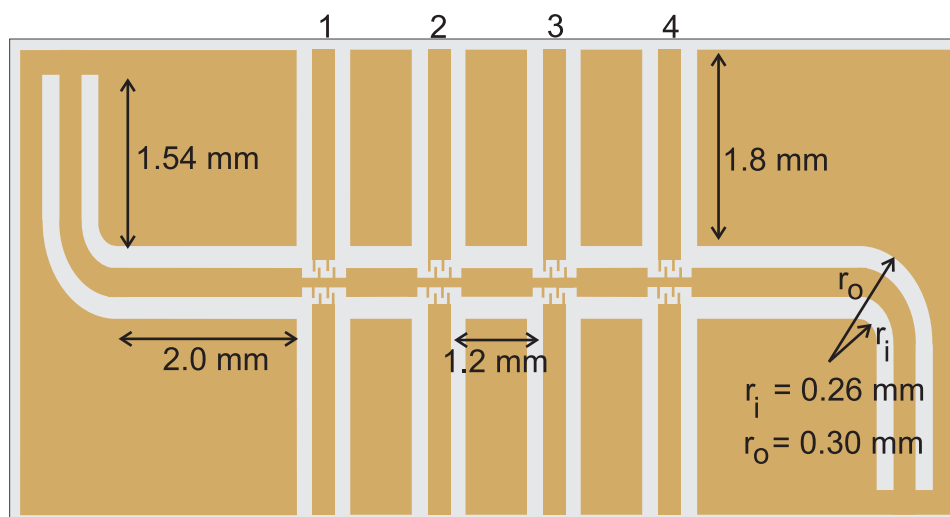


Figure 2.10: The coplanar waveguide arrangement with four integrated photoconductive switches. Each switch is driven by an optical fiber glued above it. The distance between the switches is 1.2 mm. This CPW design allows for a simultaneous measurement of the transmission and the reflection properties of the active device under study. Such a device would be placed between switches 2 and 3.

a traveled distance of 4.6 mm. The length of the trajectories b_1 and b_2 is 4.8 mm and is close to this value for peak (b). Thus the peak (b) can be thought as a composition of contribution of b_1 and b_2 . Also the bend in the coplanar waveguide may cause a reflection (indicated by trajectory b_3 whose length is 5.2 mm in Fig. 2.11b). This reflection would appear at 54 ps. As in the CPW arrangement with two integrated switches the pulse trajectories c_1 and c_2 bring about peak (c). These trajectories are also included in Fig. 2.11b. Due to the different length of these trajectories two peaks are expected, each of which is attribute either to the trajectory c_1 or to the trajectory c_2 . The peak associated with trajectory c_1 is expected at 95.3 ps, while the one associated with trajectory c_2 should appear at 145 ps. The peak (c) appears however at 85.8 ps. Even though there is a clear discrepancy with the estimated time based on the sample geometry, it is still legitimate to state that the origin of this reflection is somewhere on the parasitic waveguide (along trajectory c_1 or c_2). In order to understand the discrepancy experiments on a CPW with different dimensions, e.g. different length of parasitic waveguide or/and different length of the side arms, are needed.

An interruption in the waveguide geometry, as introduced for instance by integrated photoconductive switch, may cause a change in the spectral content of the pulse. Its consequence may be both the change of the propagation velocity and the pulse broadening.

In the experiment, which involves switches 1 and 3, the electrical pulse passes an interruption in the waveguide imposed by switch 2. The trace going along the positive direction of the time axis in Fig. 2.12 is acquired for the case, when switch 1 is the source and switch 3 is the detector. The other trace in this figure goes along the negative direction of the time axis and is acquired when the roles of the switches are reversed. The peaks (a) at 24.6 ps and (a') at -24.6 ps are assigned to direct pulse propagation between the source and the detector. We again obtain a propagation velocity equal to $0.32c$. The experiment, which involves switches 1 and 4, yields also the propagation velocity of $0.32c$. The traces of this experiment are not shown here. Hence, we conclude that the propagation speed does not change for signals passing from switch 1 to switch 4.

In Fig. 2.13 we compare traces recorded with switches 2, 3 and 4 as detector switch. They are normalized by making the amplitude of the first peak equal. Moreover, they are shifted in time so that all first peaks coincide on the time axis at time zero. This data representation reveals a marginal change of the width of the first peak, which indicates a weak pulse broadening while propagating along the CPW. The waveguide structure with four photoconductive switches contains a number of interruptions, which favor the excitation of even modes. Beside the reflection peaks (b) and (c) in Fig. 2.13 the traces exhibit a more complex pattern. It probably originates from mixing of odd and even modes.

It was argued above, that the origin of feature (b) is a reflection at the open end of the side arm, which is used as a lead to bias the switch, This side arm acts as a parasitic waveguide. To confirm this the propagation trace is acquired using switch 2 and 3 in the same manner as the experiments discussed above. The traces are depicted in Fig. 2.14. The propagation velocity between the switches remains $0.32c$. The trace exhibits a complex structure, which is again attributed to mode mixing. The striking feature here is the presence of a reflection peak at ± 48 ps. Its position relative to the first peak is just the same as in Fig. 2.13. This agrees well with the explanation that the peak originates from the reflection at the open end of the side arm. Another reflection peak, which is labeled (c), is absent in this propagation trace. The assumption, that

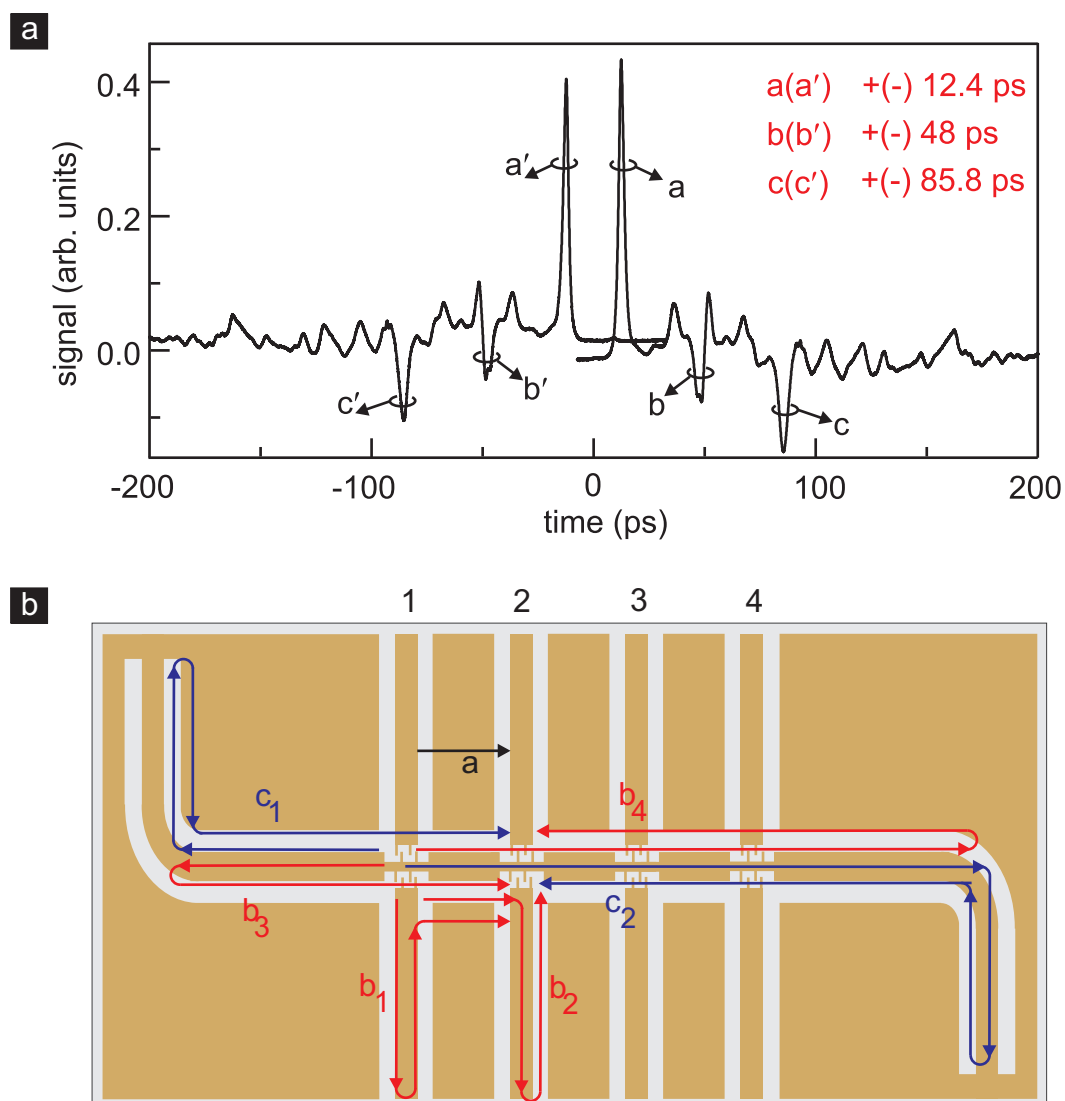


Figure 2.11: a) Propagation traces using switches 1 and 2 on the CPW with four switches. The trace for positive time is obtained when switch 1 assumes the role of the source and switch 2 is the detector. The data recorded when swapping the roles of the switches is plotted on the negative time axis. b) Pulse trajectories, which account for the peaks in panel a.

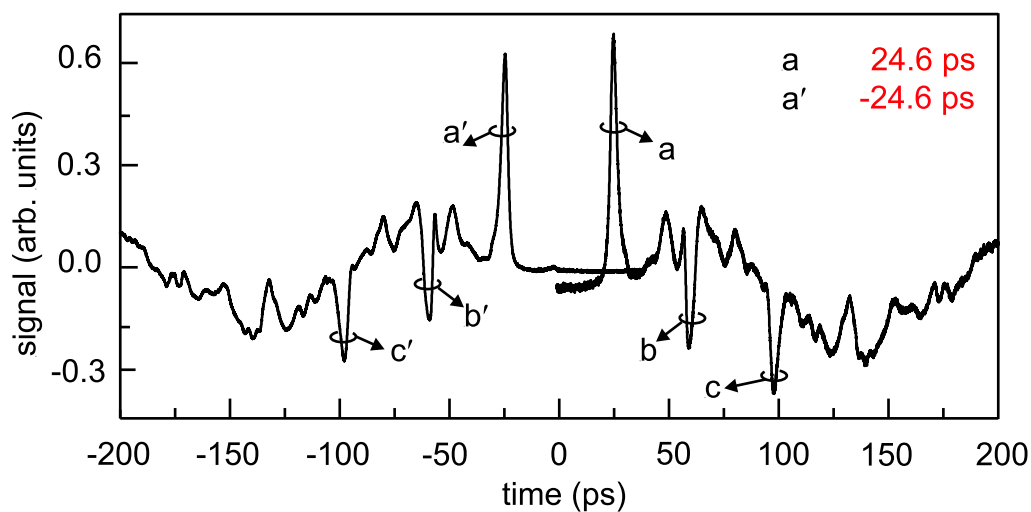


Figure 2.12: Pulse propagation traces recorded on the CPW with four switches using switch 1 and 3. The trace for positive time is obtained when switch 1 assumes the role of the source and switch 3 is the detector. The data recorded when swapping the roles of the switches is plotted on the negative time axis.

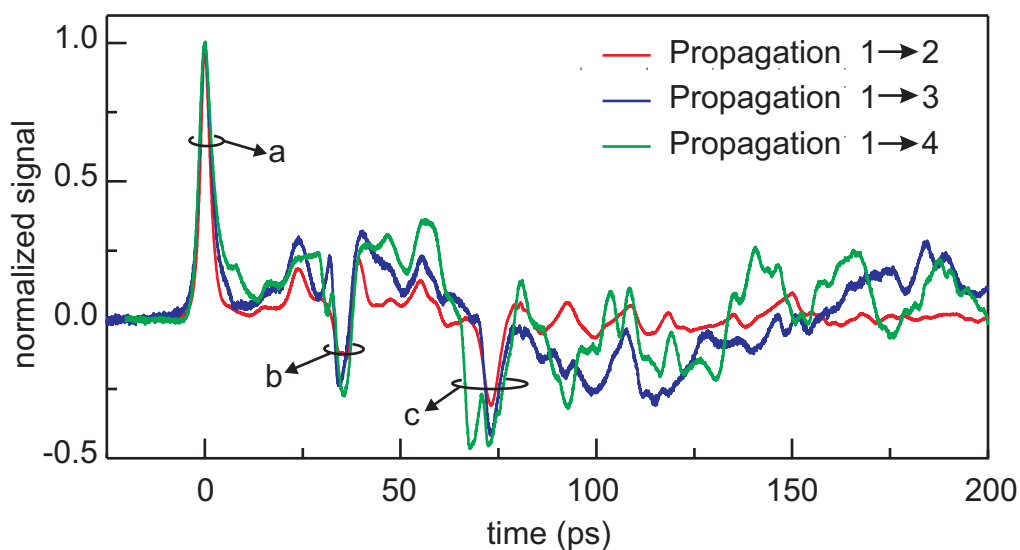


Figure 2.13: Pulse propagation traces on the CPW with four switches. Switch 1 acts as the source. The three traces show the signal at the detectors 2, 3, and 4 respectively. The traces are shifted in time so that all first peaks coincide at time zero. The amplitudes are normalized for the sake of comparison.

this peak could be attributed to a reflection at the short-circuited end of the parasitic waveguide, is indirectly confirmed in the result shown in Fig. 2.14. The travel distance to the short-circuited end of the waveguide is longer than, for instance, in the experiment with switches 1 and 2. Thus the signal is stronger attenuated and would appear at time beyond 100 ps. Also the waveguide discontinuities along the travel path favor the excitations of the even mode and lead to mode mixing. Therefore the attenuated peak might be hidden in the complex structure of the propagation trace.

The experimental results suggest to keep as less interruptions in the waveguide geometry as possible. Any interruption acts as an additional waveguide and results in spurious reflection peaks. The interruptions in the waveguide are, however, indispensable, as they are needed, for instance, to integrate the switches into the waveguide or to include the surface gates into the structure of the device under study.

There are several strategies to tackle the problem with the reflections.

1. The metal used to fabricate the parasitic waveguide is the same as what is used for the main waveguide between the source and detector switch. Instead, a material with higher resistivity can be used for parasitic waveguide to attenuate the spurious signal [24].
2. The ends of the waveguide are poorly terminated; they are either open or short-circuited. A better way to terminate the waveguide is to load it with an impedance that matches the wave impedance of the line. For the waveguide, which is considered in this work, the wave impedance amounts to 46Ω (Appendix A). Such an impedance can be realized with thin films of chromium or titanium [11]. The advantage of the thin films is that they can easily be integrated into the CPW geometry. Difficult however is to reproducibly obtain a specific resistance. The resistivity of these thin films is also temperature dependent and impedance matching is only possible for a limited temperature range.

Following the work of M. Griebel [11], the propagation velocity along a CPW can be calculated (see Appendix A). The propagation velocity along the waveguide patterned on ErAs:InGaAs amounts then to $0.39c$. For this a dielectric constant $\epsilon = 12.5$ for InP is assumed [25]. This assumption is legitimate, since the high frequency signal mainly travels within the InP substrate. Note, that the thickness of the ErAs:InGaAs superlattice is $2\mu\text{m}$, while that of InP is $500\mu\text{m}$. The experiments in this chapter yield, however, a propagation velocity of $0.32c$. Though this puzzle does not have any consequence for the experiments presented in this work, it should be addressed in the future work. This discrepancy becomes important when the end of the waveguide needs to be terminated with a load that matches the impedance of the waveguide. Based on the experimental value of the pulse propagation velocity, the effective quasi-static constant $\hat{\epsilon}_{\text{qs}}$ would be equal to 9.8 and thus the wave impedance amounts to 37Ω . In contrast, the wave impedance is 45Ω if one follows the calculation presented in Appendix A. Therefore a load with wrong impedance would result in a poor termination of the waveguide and reflections would not be avoided.

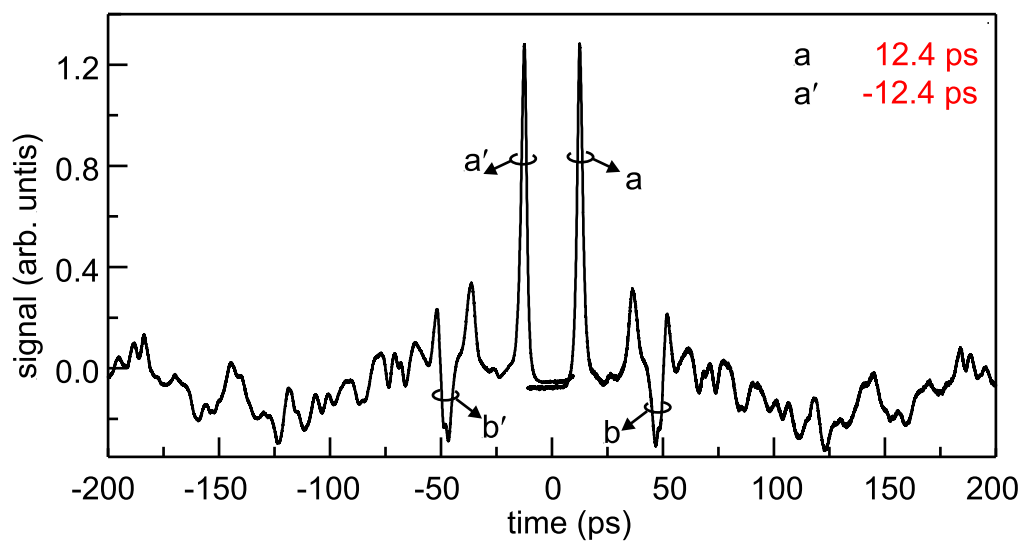


Figure 2.14: The propagation trace going along the positive direction of the time axis is measured for pulse propagation from switch 2 to switch 3. Sweeping the role of the switches one obtains the trace going along the negative direction of the time axis. The propagation velocity amounts to $0.32c$ and is the same as for other sections of the CPW.

Chapter 3

DC-Experiment

3.1 Introduction

The measurement set-up developed in the previous chapter facilitates the measurement of the time which it takes for electrons to propagate through a mesoscopic device fabricated from a high-mobility two-dimensional electron gas. For electrons at small magnetic fields the outcome of such a time-resolved experiment should be well-known. In the ballistic regime, the electrons propagate at the Fermi velocity which is determined solely by the density. The measured time delay would, however, be composed of several contributions: the time it takes for a pulse to run from the source switch to the device, the time it takes to travel through the device and finally the propagation time to reach the detector switch. Only the second contribution to the time delay is of interest. Since it is difficult to predict the other contributions with sufficient accuracy, it is essential to devise a scheme in which a relative time delay is measured and the other contributions automatically drop out. This can be accomplished by designing geometries in which electrons can travel along two or more trajectories of different lengths depending on a tunable parameter such as for instance the strength of the applied magnetic field. In this chapter, different types of ballistic devices are pursued and characterized in DC experiment. They are possible candidates for a time-resolved transport experiment and are either modified transverse magnetic focusing device or ballistic cavities with different shapes (triangle, square, hexagonal).

The experiments on the modified magnetic focusing devices are supported with numerical calculations, which were conducted by Jakob Metzger and Ragnar Fleischmann from the Max-Planck-Institute for Dynamics and Self-Organization.

3.2 Quantum Point Contact

A common element of the mesoscopic devices, which are considered in this chapter, is a quantum point contact [26,27]. It serves as a source or as a detector of ballistic electrons. It consists of a short and narrow constriction in the 2DES with a width on the order of the electron Fermi wavelength. Hence, the momentum in the transverse direction is quantized and takes on discrete values: $k_{\perp}^n = \frac{n\pi}{w}$, where w is the width of the constriction. When an electron from the wide 2DES reservoir at the Fermi surface with wavevector k_F enters to the n th mode of the quantum point

contact (QPC), its forward momentum changes to

$$k = \sqrt{k_F^2 - (k_\perp^n)^2}. \quad (3.1)$$

A small constriction in the 2DES can be realized with split gates on top of the heterostructure [28]. A negative voltage applied on gates locally depletes the 2DES region underneath leaving only a narrow undepleted channel. The width of the channel and thus the resistance of the QPC can be tuned by increasing the applied negative gate voltage. Alternatively a narrow channel can be formed by removing the 2DES everywhere except for a narrow area. In this case the channel width is fixed and cannot be tuned *in-situ*. The angular distribution of electrons injected through the QPC is proportional to a cosine function with an abrupt truncation at a certain angle $\pm\alpha$, which is determined by the shape of the QPC [29]. A gradual flaring of the confining potential of the constriction and the redirection of the electron flow as described by Eq. 3.1 above causes the collimation of the electron beam. Collimation has been demonstrated in transport experiments in a geometry with two opposing QPCs [29, 30]. In particular, the experiments demonstrated that the collimation is stronger for a narrower QPC opening. By varying the voltages applied to the gates, which form the QPC, the beam collimation can be tuned continuously. An in depth review about the properties of quantum point contacts can be found in Ref. [29, 31] and references therein.

3.3 Caustic

For the analysis of the DC transport characteristics of ballistic devices the concept of a caustic [32, 33] plays a central role. Consider two trajectories which start from the same point in space at angles α and $\alpha + \delta\alpha$ with $\delta\alpha \ll \alpha$ and bound a particle flux tube (gray area in Fig. 3.1a). These trajectories are mathematically described as $\vec{r}_\alpha(t)$ and $\vec{r}_{\alpha+\delta\alpha}(t)$. The point where these two trajectories cross is called a caustic:

$$\vec{r}_\alpha(t) = \vec{r}_{\alpha+\delta\alpha}(t + \delta t), \quad (3.2)$$

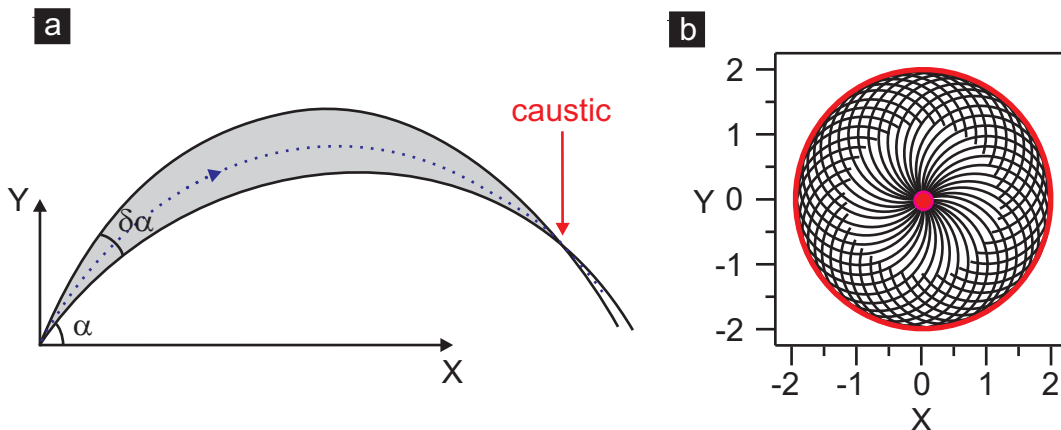


Figure 3.1: a) A caustic is formed at the point, where two trajectories, which bound a particle flux tube (gray area), cross. b) In a magnetic field the orbits with radius $R = 1$ build a caustic (red circle). It is located at $2R$ away from the source of the trajectories.

where t is a parameter that describes the trajectory. This definition of a caustic does not specify why the trajectories cross. In a magnetic field, for instance, the electrons move on circular orbits with radius R . A circular trajectory leaving the origin at angle α may be parameterized as follows:

$$\begin{cases} x = R(\cos(\alpha) - \sin(t)) \\ y = R(\sin(\alpha) + \cos(t)), \end{cases} \quad (3.3)$$

where α and t are parameters that describe the position of an electron on the orbit. Therefore, the condition for a caustic Eq. 3.2 can be rewritten as:

$$\begin{cases} x = R(\cos(\alpha) - \sin(t)) = R(\cos(\alpha + \delta\alpha) - \sin(t + \delta t)) \\ y = R(\sin(\alpha) + \cos(t)) = R(\sin(\alpha + \delta\alpha) + \cos(t + \delta t)). \end{cases} \quad (3.4)$$

Assuming $\delta\alpha \ll \alpha$ and $\delta t \ll t$ the equations have two solutions: the trivial solution $x = 0$ and $y = 0$ where all trajectories start. The second solution

$$\begin{cases} x = -2R \sin(\alpha) \\ y = 2R \cos(\alpha) \end{cases} \quad (3.5)$$

describes an envelope of the electron trajectories and is a caustic formed in the magnetic field by electron trajectories emitted from a point source. For each point on this envelope the density of electron trajectories diverges. This effect may be described as focusing of electron trajectories by a magnetic field. The electrons start from the same point in space and trajectories rejoin at another point in space. This sort of deterministic focusing takes place at a distance of one cyclotron orbit diameter away from the source (Fig. 3.1 b) as described by the second solution. The caustics of the electron trajectories can be detected in a transverse magnetic focusing (TMF) experiment.

3.4 Transverse magnetic focusing device

Transverse magnetic focusing experiment is a school example to demonstrate the ballistic propagation of electrons in a 2DES [34]. Here, two quantum point contacts are arranged along a line at a distance $2a$ apart. One of the QPCs serves as the electron injector, while the other collects the electrons. A schematic of a TMF device is shown in Fig. 3.2. A magnetic field B applied perpendicularly to the 2DES plane forces the electrons into circular orbits. For electrons at the Fermi surface, this orbit has a radius:

$$r = \frac{\hbar k_F}{eB} = \frac{\hbar\sqrt{2\pi n}}{eB}, \quad (3.6)$$

where n is the electron density of the 2DES. The first caustic appears at the second QPC when the radius of the cyclotron motion $R = a$ and hence at the magnetic field

$$B_0 = \frac{\hbar\sqrt{2\pi n}}{ea}. \quad (3.7)$$

At higher fields the electron trajectories bounce against the boundary between the two QPCs.

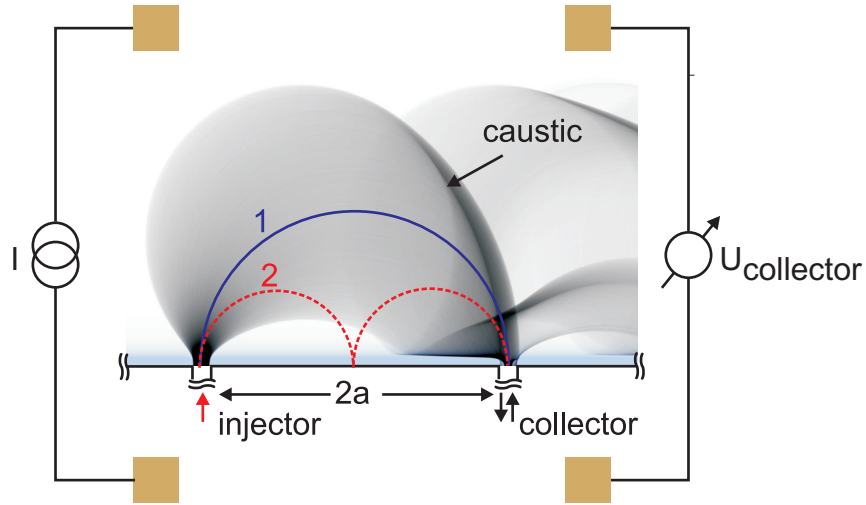


Figure 3.2: Schematic of a transverse magnetic focusing device. Electron trajectories are drawn for the magnetic field $B = B_0$. The injector emits a collimated electron beam with a certain distribution of electron trajectory centered around the electron trajectory denoted as 1. Shaded areas represents the spread of electron trajectories. The darkness of the gray shading is a measure of the local trajectory density. At field B_0 a caustic is formed at the collector. At this field also the central trajectory enters the collector. At $2B_0$ the electrons execute skipping orbits and their trajectories form a caustic at the collector. The central electron trajectory (depicted 2) reflects at the wall and enters the collector. (Picture provided by Jakob Metzger and Ragnar Fleischmann.)

The electrons execute skipping orbits. The trajectories form caustic at the collecting QPC when the cyclotron diameter or a multiple thereof equals the distance $2a$. In the experiment the voltage drop across the collector QPC exhibits periodic oscillations with maxima at the magnetic fields iB_0 , where i is an integer number. This number i is called the peak order. Note the central trajectory of the collimated electron beam (labeled 1 in Fig. 3.2) runs directly into the collector QPC at the magnetic field B_0 . Also at field $2B_0$ the central trajectory labeled 2 enters the collector QPC (Fig. 3.2). In general, each caustic peak in the TMF device occurs at the same values of the magnetic field for which also the central trajectory of the electron beam enters the collecting QPC.

A transverse magnetic focusing device is not suitable for time-differential measurements. The distance an electron travels before entering the collecting QPC is independent of the magnetic field, i.e. order i . trajectory length is independent of the magnetic fields. Indeed, the length of the electron trajectory emitted perpendicular from the QPC at the magnetic field iB_0 is given by

$$L = \frac{\hbar\sqrt{2\pi n}}{eB_0 i} \cdot \pi \cdot i = \frac{\hbar\sqrt{2\pi n}}{eB_0} \cdot \pi = a\pi. \quad (3.8)$$

A small modification of this geometry, however, allows to implement the idea of making time-differential measurements.

3.5 Corner Device

Instead of placing the quantum point contacts along a single line, they are arranged along two legs which form a corner. For the sake of simplicity we consider only a 90° -corner and the case where both point contacts are at equal distances from the corner. Such a device is shown in Fig. 3.3. Its operation can be understood intuitively as follows. The magnetic field applied perpendicularly to the plane of the device deflects the electron beam ejected from the QPC. At field B_0 the central trajectory of the electron beam arrives at the collecting QPC (Fig. 3.3a). Note, at this magnetic field the caustic has not been built yet. Hence, the signal at the detector appears only due to the collimating properties of the QPC. The caustic emerges, however, at field $\sqrt{2}B_0$, which follows from a simple geometrical consideration. It is formed by the trajectories that are emitted from the QPC under a slight angle. These trajectories are colored in red in Fig. 3.3b. Note that the central trajectory 1 does not arrive at the collecting QPC. As the magnetic field increases further the electrons are deflected into the corner of the device. At field $2B_0$ a caustic forms in the corner. After the reflection in the corner, trajectories refocus at the collecting QPC (Fig. 3.3c). The scenario of electron focusing in the corner and refocusing at the collecting QPC takes place at fields iB_0 with i an even number. At these fields the electrons behave effectively as in a conventional transverse magnetic focusing device provided the diameter of the electron orbits is much larger than the dimension of the corner. If the diameter of the electron orbit becomes comparable to the size of the corner, the caustic will no longer form in the corner. Other peaks are expected at fields iB_0 , where i is an odd number. They arise when the central trajectory from the emitting QPC enters the collector. Here, caustics form at the wall

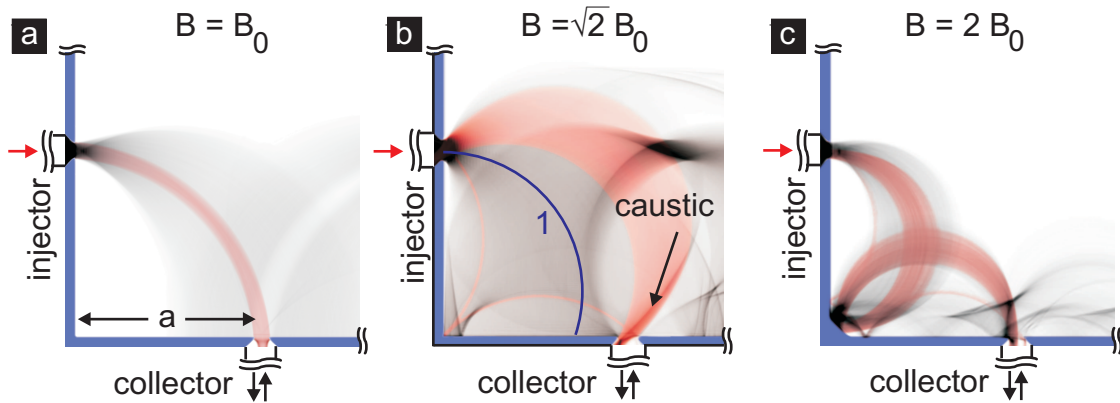


Figure 3.3: Electron trajectories in the corner device at different magnetic fields. The electron trajectories, which are emitted from the QPC, are colored black. A part of these trajectories (colored red) reach the collector QPC at the magnetic field indicated in each panel. a) A peak attributed to the QPC collimation is detected at the field B_0 . b) A caustic peak at field $\sqrt{2}B_0$ is formed by electron trajectories emitted from the QPC under slight angle. c) A formation of caustic takes place at field $2B_0$ and mimics the behavior in a conventional transverse magnetic focusing device. Here the simulation is done for a corner device with a chamfered corner. Qualitatively the focusing does not depend on the corner shape. (Pictures provided by Jakob Metzger and Ragnar Fleischmann.)

adjacent to the injector QPC. After hitting this wall, the electron trajectories defocus and do not build caustics later. These peaks are therefore collimation peaks. Thus the resistance peaks due to collimation and magnetic focusing are separated on the magnetic field axis and appear alternately. The decisive feature of the corner device is the different length of the electron trajectories which contribute to the odd and even order peaks. Indeed, the distance an electron travels along the central trajectory before entering the collecting QPC in the magnetic field iB_0 with i an odd number is

$$L_i = a\pi \frac{2i - 1}{2i}, \quad (3.9)$$

while for an even number i the electron trajectory length is

$$L_i = \pi a \quad (3.10)$$

and thus independent of the peak order. Hence, the corner device is a suitable geometry for time-differential measurements. It is instructive to estimate the travel times which are expected in the experiment. A typical electron density of $n = 2 \cdot 10^{11} \text{ cm}^{-2}$ corresponds to a Fermi velocity of $v_F = 0.2 \text{ } \mu\text{m/ps}$. The length of the corner arm a equals $3 \text{ } \mu\text{m}$. For the time-resolved experiment it is sufficient to consider only two peaks, e.g. at fields B_0 and $2B_0$. At field B_0 an electron runs a distance of $\pi a/2 = 4.7 \text{ } \mu\text{m}$ which takes 23.5 ps , while at $2B_0$ the electron trajectory length amounts to $\pi a = 9.4 \text{ } \mu\text{m}$ and the travel time is 47.0 ps . These travel times are very well accessible with the measurement technique presented in the previous chapter.

3.6 Experimental results

The devices are fabricated from a modulation doped GaAs/AlGaAs heterostructure in which the 2DES is located 150 nm underneath the crystal surface. The two quantum point contacts of the corner device are defined by three surface split gates. One split gate in the corner is shared by both quantum point contacts. A negative voltage applied on the gates depletes the 2DES beneath and defines the constriction in the 2DES. The sample fabrication is outlined in detail in Appendix C. The sample is placed in the center of a superconducting coil which allows to apply a magnetic field in the experiment. The sample space is cooled down to 1.4 K . A current of 5 nA is imposed through the sample and is modulated at a frequency of 13.33 Hz in order to use lock-in detection technique. As the magnetic field is swept at a rate of 15 mT/min , the voltage drop across both the injector and detector QPC is measured in a four-terminal configuration in order to avoid the contribution from contact resistances.

Two types of corner devices are characterized: corner devices with sharp (type I) and chamfered corner (type II). The electron density n in these devices equals to $2.5 \cdot 10^{11} \text{ cm}^{-2}$ and $2.2 \cdot 10^{11} \text{ cm}^{-2}$ respectively. Figures 3.4 and 3.5 summarize the experimental results for a device of type I and type II device. For the type I device (right inset in Fig. 3.4) the first resistance peak appears at $B_0^{exp} = 25 \text{ mT}$, while the theoretically expected position is at $B_0^{th} = 27.5 \text{ mT}$. This discrepancy can likely be attributed to the precision with which both the electron density and the device geometry are known. At B_0 , the central trajectory of the emitting QPC enters the detector (trajectory 1 in right inset). According to our previous theoretical consideration a caustic peak is expected at a magnetic field $\sqrt{2}B_0^{exp} = 35 \text{ mT}$. The left inset in Fig. 3.4 shows

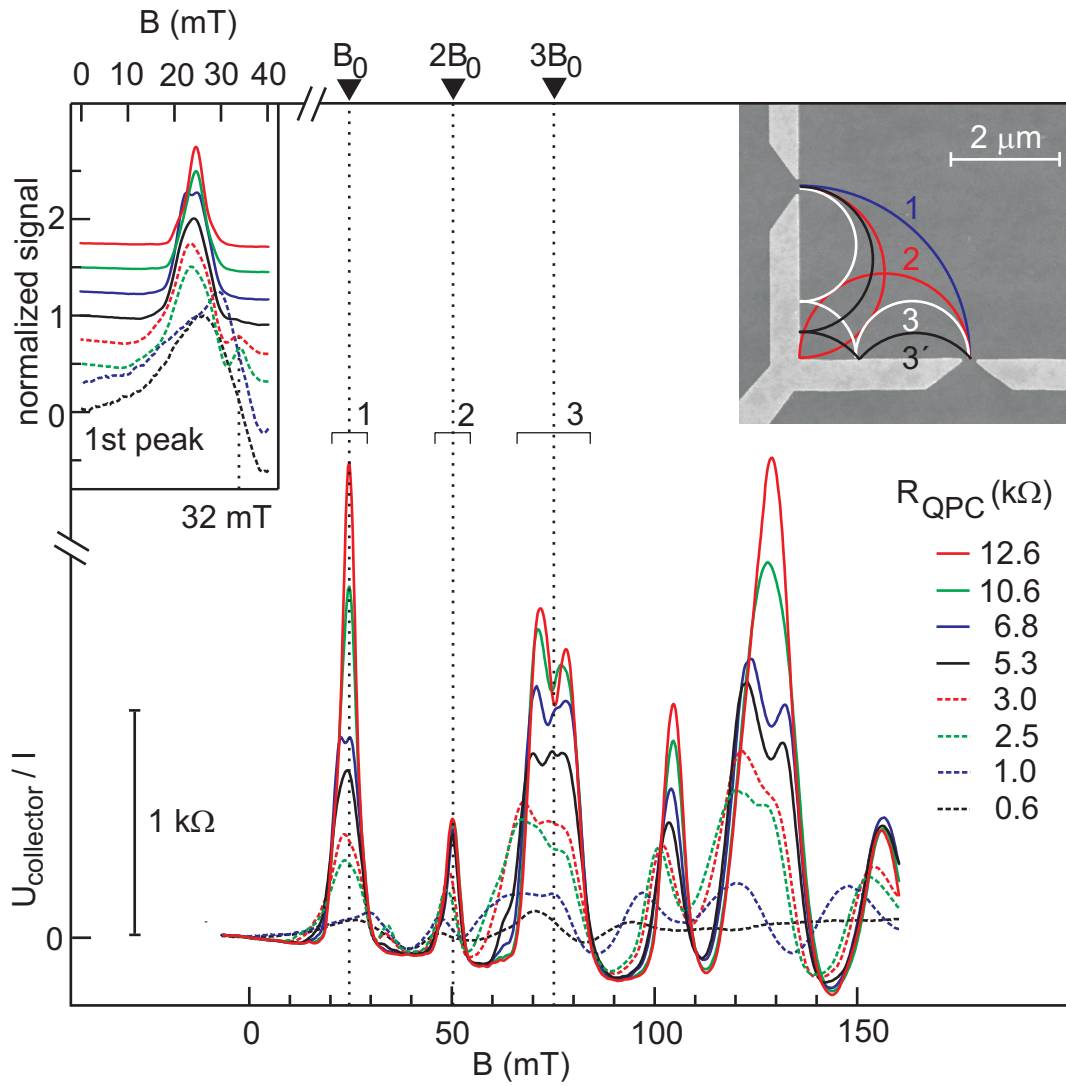


Figure 3.4: Magnetoresistance traces measured on a corner device with a sharp corner for a set of different gate voltages, i.e. QPC resistance values. The right inset depicts an SEM picture of the corner device. Central electron trajectories of the emitting QPC at fields B_0 , $2B_0$, $3B_0$ have been included. The left inset shows the first peak normalized in their amplitude. For clarity, these curves are offset by 0.25.

the first peak for different QPC resistance values. The amplitude of each peak is normalized to 1. Curves are offset for clarity by 0.25. A small additional peak emerges for a limited range of the QPC resistance values at 32 mT. It grows as the QPC resistance increases up to 2.5 k Ω , but then vanishes as the QPC width is reduced further. Numerical simulations, which will be discussed in section 3.7, show indeed that this behavior is expected for a caustic peak, which is formed by electron trajectories emitted from QPC at a slight angle. Here, we restrict ourselves to a straightforward simplified and intuitive description. An increase of the QPC resistance narrows the electron beam. As a result, the broad collimation feature and, therefore, the number of electron trajectories, which contribute to the caustic peak at $\sqrt{2}B_0$, reduces. This leads to a gradual and eventually to a total suppression of the caustic peak. This is a distinct feature of the

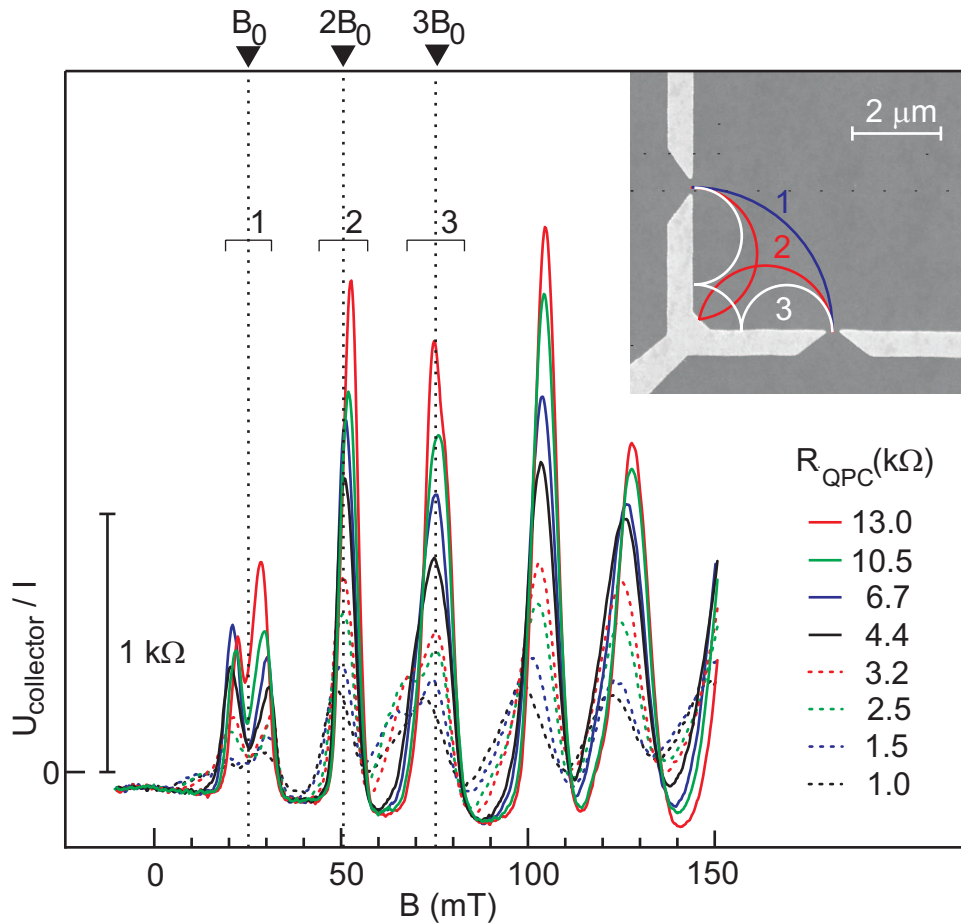


Figure 3.5: Magnetoconductance traces measured on a corner device with a chamfered corner for a set of gate voltages. The inset depicts an SEM picture of the corner device and the electron trajectories injected at the center of the upper QPC at fields B_0 , $2B_0$, $3B_0$.

corner device. For the device with a chamfered corner the first (collimation) peak is expected at $B_0^{\text{th}} = 25.8$ mT and the first caustic at $\sqrt{2}B_0^{\text{th}} = 36.4$ mT. Figure 3.5 shows data obtained on this device geometry. A double peak structure with maxima at 20 mT and 28 mT is observed instead. Even though it might be natural to assign the first peak of this double structure to collimation and the second at approximately $\sqrt{2}$ larger value of the magnetic field to the formation of a caustic at the collecting QPC, we assert that this assignment is incorrect. B_0^{exp} would deviate more than 20 % from the theoretical estimate. A proper assignment of these features requires numerical simulations. We will show that disorder induced branching of the electron flow can account for a splitting of the first collimation peak expected at 25.8 mT. Increasing the magnetic field further bends the electron trajectories toward the corner (trajectory 2 in both right insets) where they reflect and then enter the detector. These trajectories contribute to the peaks at 50 mT and 52 mT for type I and type II devices respectively. Their position coincides well with the expected position at $2B_0^{\text{th}}$. Due to the chamfered corner the second peak is enhanced in the type II device. The third peak is assigned to the trajectory 3, which hits every side wall once. It is interesting to note that the third peak exhibits a splitting with maxima at

71 mT and 78 mT for the largest QPC resistance in the type I device. The third peak at 75 mT is not split in the type II device. The higher order peaks appear at a multiple integer of B_0^{exp} for both device types. At higher magnetic fields the electron trajectories run closer to the edge defined by the split gate where the density is reduced. As a result deviations can occur from the predicted position on the magnetic field axis. This so-called "soft wall" effect has been reported previously in the literature [35].

The most interesting feature in magnetotransport traces presented here is the splitting of the first peak. We point out that the traces shown in Figures 3.4 and 3.5 are typical for experimental outcomes obtained in other 8 corner devices. The results of those experiments are not shown here, as they do not significantly contribute to the understanding of the peak splitting. We point out that there is no correlation between the shape of the corner and the shape of the first peak, as the trajectories associated with this peak do not traverse the vicinity of the corner. This is demonstrated on a device (Fig. 3.6a) with a corner gate that can be operated separately from the QPCs. The blue trace in Fig. 3.6b is recorded when the corner is present (2DES under the gate is depleted), while the red trace is taken when the corner is not defined. The length of the legs forming the corner is $3 \mu\text{m}$ and the electron density equals $2 \cdot 10^{11} \text{ cm}^{-2}$. The first peak attributed to collimation around the central trajectory emitted from the QPC appears at a magnetic field of $B_0^{exp} = 23.6 \text{ mT}$ and is independent of the presence of the corner. There is a difference of 1 mT between this number and the theoretically expected value. This small discrepancy can be accounted for the precision with which both the geometry of the device and the electron density are known. The second peak, which is a caustic peak at $2B_0$ has a very different amplitude for the two cases. As expected, it is much weaker when the corner is not defined. Despite the absence of the corner, the peak has however not entirely vanished. The electrons leaving the source quantum point contact have an angular distribution. Those particles injected under an angle in both tails of this distribution may still hit the wall and hence may be responsible for the

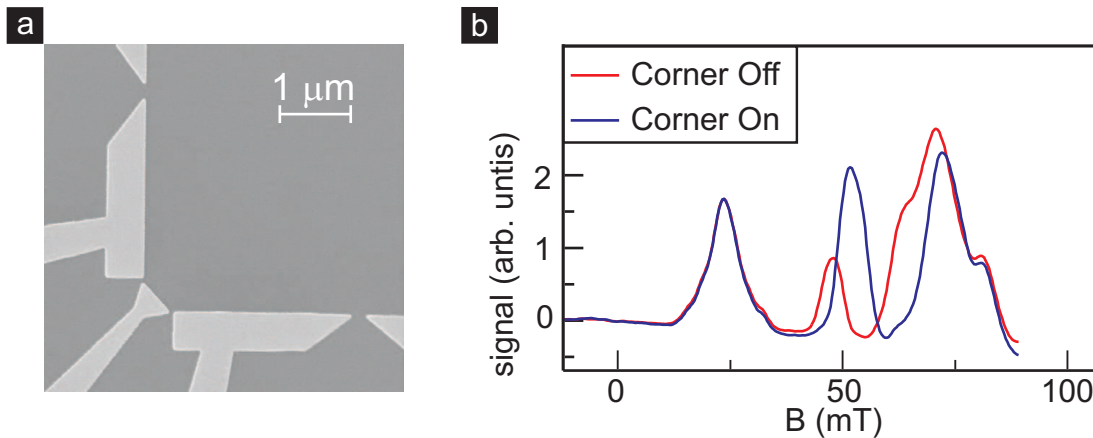


Figure 3.6: a) SEM picture of a corner device, whose corner is controlled independently from the quantum point contact. b) Magnetotransport traces obtained in the corner device. The red trace is the measurement with the corner turned off (the gate is grounded). The blue trace was taken with the corner turned on (2DES under the corner gate is depleted). The shape of the first peak is not influenced by the absence or presence of the corner.

appearance of a small peak. Electrons injected with angles in the central part of the distribution reach the corner and are absorbed in the large reservoir. They do not contribute to the focusing feature. The third peak around $3B_0^{exp}$ is expected to be present in both devices with a nearly identical amplitude, since the associated trajectory bounce of the middle of the walls away from the corner.

3.7 Numerical transport simulation in disorder-free landscape

The experiment is supported by numerical simulations of the electron transport in the corner device. First, we consider the transport in a flat potential landscape, i.e disorder-free landscape; it is an ideal cases. For simulation a QPC is tailored as a sum of the variable-depth hyperbolic tangents and the saddle potential profile within the QPC is shown in the inset of Fig. 3.7. Further, we assume a cosine-like electron distribution which is collimated by the saddle potential. Soft wall effects due to depletion are modeled by using a quadratic potential at the walls. The maximum height in the saddle potential is varied between $0.2E_F$ and $0.8E_F$, where E_F is the Fermi

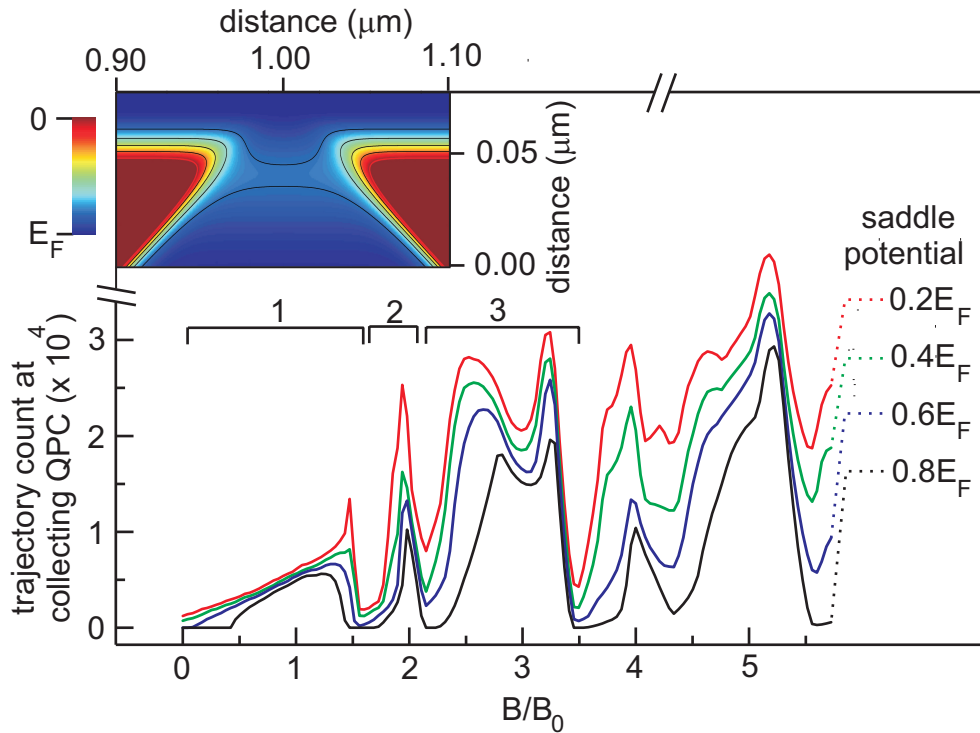


Figure 3.7: The number of electron trajectories which reach the collecting QPC as a function of B/B_0 in the geometry depicted in Fig. 3.5 without a disorder potential. The calculation is done for four different maximum heights of the saddle potential in the QPC and assumes a collimated cosine electron distribution. The caustic peak appears at the field $\sqrt{2}B_0$. Its amplitude drops for higher saddle potentials. The brackets indicate the assignment of the peak order. The inset shows the equipotential lines in the QPC for a saddle potential $0.2E_F$. (The calculation has been performed by Jakob Metzger and Ragnar Fleischmann.)

energy in non-depleted 2DES region. 10^5 trajectories are tracked in the magnetic field until they have reached the collector QPC. Figure 3.7 depicts the number of electron trajectories which reach the collecting QPC as a function of the magnetic field (B/B_0) for different heights of the saddle potential. For the weakest saddle potential, $0.2E_F$, we observe a peak at $\sqrt{2}B_0$ which is the expected caustic peak. As the barrier in the QPC continuously increases, the electron beam emitted from the QPC becomes narrower. A high saddle potential reduces the number of electron trajectories which contribute to the caustic formation and thus suppresses the caustic peak. This brings out the peak at B_0 attributed to the trajectory bundle which is represented by trajectory 1 in Fig. refSharpCorner. Such a behavior gives an account of the experimental observation (Fig. 3.4) and is a distinguished feature of the corner device. The simulation also reveals a splitting of the third peak (compare Fig. 3.4). There is one peak positioned between $2.4B_0$ and $2.8B_0$ depending on the saddle point height and another is fixed at $3.2B_0$. The former is caused by a trajectory (trajectory 3' in inset Fig. 3.4), which is emitted perpendicular to the QPC and hits the collecting QPC at a different angle. A higher saddle point potential suppresses these trajectories and favors those emitted at a slight angle which can then pass the collecting QPC more easily. This causes the peak to shift towards $3B_0$ for higher saddle points. The peak at $3.2B_0$ belongs to the trajectory bundle whose central trajectory is labeled as 3 in Fig. 3.4. It is shifted slightly towards higher magnetic fields because of the triangular shaped QPC.

The simulation results of electron transport in a disorder-free landscape explains only a small part of the experimental traces. It cannot explain the most interesting feature, the shape of the first peak. In what follows the numerical simulations are extended to the more realistic case where the electron transport proceeds in a disordered potential landscape.

3.8 Numerical transport simulation in disordered landscape

In a high-mobility modulation-doped two-dimensional electron gas two main mechanisms determine the electron scattering at low temperatures: remote ionized dopants in the modulation-doped layer and unintentional background charged impurities [36, 37, 38]. While the ionized dopants form a weak disorder landscape, which mostly contributes to small angle scattering of the electrons, the background impurities cause hard scattering of the electrons. The latter is the largest contribution to the electron mobility even in structures with high purity [38] and determines, therefore, the electron mean free path in the structure. However, on length scales much smaller than the electron mean free path, recent experiments [39, 40] and theoretical work [41] demonstrated that the weak disorder potential has a stronger impact on the electron flow. It alters the electron flow and leads to a pronounced branching of it. Only in low-mobility 2DES the scattering by the background impurities becomes more prevalent [40, 42]. Hence, we exclude this scattering mechanism, as the work is performed on structures with high mobility, and consider only the impact of ionized dopants. Their weak disorder potential acts on the electron flow analogous to an electrostatic lens [43], which randomly focuses the electron flow and thus forms caustics of electron trajectories (Eq. 3.2). This caustic is the origin of branch formation - a region with an enhanced density of electron trajectories compared to a disorder-free system [40, 44]. To account for the disorder in our system the disorder potential is modeled by a Gaussian correlated Gaussian random field with a standard deviation V_0 and a correlation

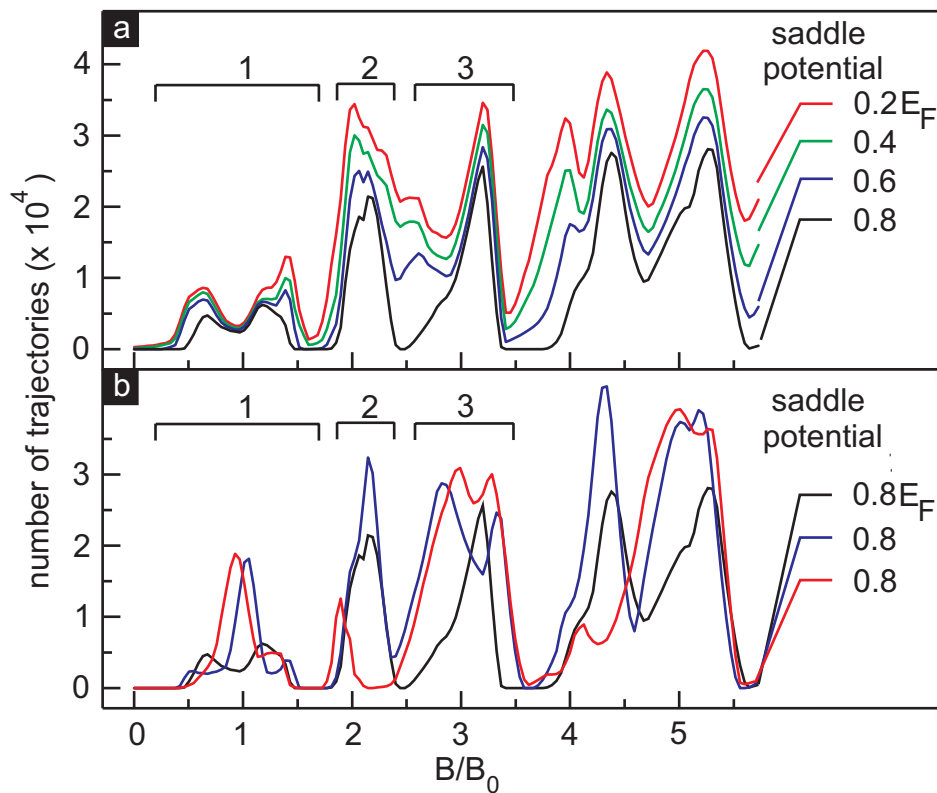


Figure 3.8: The number of trajectories which reach the collecting QPC as a function of B/B_0 in different realizations of the disorder potential. a) For one realization of the disorder potential, the curves are calculated for different heights of the saddle potential in the QPC. The caustic peaks at $\sqrt{2}B_0$ decreases as the height of the saddle potential increases (compare Fig. 3.7). b) The curves are obtained for a different realization of disorder potential. Note, the standard deviation V_0 and the correlation length l_0 of the disorder potential do not change, but the shape of the first peak changes. The red curve is obtained in a device of type I device, while the other two are obtained in a device of type II device. In both panels the brackets indicate the assignment of the peak order. (The calculation has been performed by Jakob Metzger and Ragnar Fleischmann.)

length ℓ_c :

$$\langle V(r)V(r') \rangle = V_0^2 e^{-|r-r'|^2/\ell_c^2}. \quad (3.11)$$

For the simulation, the following parameters of the disorder potential $V_0 = 0.02E_F$ and $\ell_c \approx 180$ nm are used.

The solid lines in Fig. 3.8a are the trajectory counts at collecting QPC in the type II device for various heights of the saddle potential. Unlike the traces in Fig. 3.7, the first peak (bracket 1) shows a splitting as we have observed in the experiment (Fig. 3.5). The right peak in the double structure appears at $\sqrt{2}B_0$ for a lower saddle potential and vanishes with an increasing saddle potential. The third peak is not split. This is opposite to the result obtained in the disorder-free potential landscape (Fig. 3.7). We stress that the peak structure does not change with small

variations of the parameters V_0 and ℓ_c . It depends, however, on the specific realization of the random potential, e. g. the form of the potential landscape, which corresponds to carrying out the experiment on different pieces of the same heterostructure¹. This is illustrated in Fig. 3.8b. For comparison a curve from panel a is displayed together with two other curves, which are obtained for two other realizations of the disorder potential. In these two realizations the first peak does not feature a splitting. But a small peak at about $\sqrt{2}B_0$ is seen in both cases. Note, the parameters of the disorder potential V_0 and ℓ_c are unchanged and the height of the saddle potential is fixed at $0.8E_F$. The red line is calculated, however, for a type I device. This shows that even a weak disorder potential, whose amplitude is only 2% of the Fermi energy, affects the shape of the collimation peaks and in particular of the first peak.

3.9 Comparison of experimental results with simulation

Panel a in Fig. 3.9 compares the experimental trace for $R_{QPC} = 3 \text{ k}\Omega$ in Fig. 3.4 with the simulation result (red line) from Fig. 3.8b calculated for the potential landscape shown in Fig. 3.9c. The disorder potential deflects the electrons (black and red flow) from the trajectories they would follow in disorder free case. For comparison, the inset shows the electron trajectories at B_0 in the absence of disorder. The disorder potential causes focusing (branching) of the flow. Two examples of branch formation are indicated by white arrows in Fig. 3.9c. Flow transmitted to the collector contributes to the peak at B_0 and is marked in red. Here, the disorder potential enhances the first collimation peak due to an additional focusing of the electron flow. The much smaller satellite peak close to $\sqrt{2}B_0$ is the caustic peak due to magnetic focusing. Another realization of the disorder potential is shown in panel d. In this case, the first peak splits. The curve obtained in this landscape is compared with the experimental trace for $R_{QPC} = 4.4 \text{ k}\Omega$ of Fig. 3.5. The caustic peak at $\sqrt{2}B_0$ is hidden in the double peak structure.

It is noticeable that while various shapes of the first peak are observed in the experiments and reproduced in the numerical simulations, the shape of the second peak barely changed. This observation is attributed to different stabilities of particle flow at fields B_0 and $2B_0$, at which the collimation and the caustic peaks are formed respectively. Panels c and d demonstrate this. At field B_0 (Fig. 3.9c) the collimated particle flow is focused by the disorder potential or, equivalently, the electrons are deflected from the trajectories they would follow in disorder free case (inset panel c). In opposite, Fig. 3.9s shows that the particle flow is preserved to large extend at $2B_0$. The trajectories, which contribute to the peak at $2B_0$, are drawn red and compared to the trajectories in the disorder free landscape (inset panel d). Although the flow is altered by the random potential, most of the trajectories, which would be transmitted in the clean system, still reach the collector. Thus the particle flow at field B_0 is more prone to be focused by the disorder potential than the particle flow at $2B_0$.

When accounted for the disorder potential, the numerical simulations explain well the peak shape and its variation in different realizations of the disorder potential. The discrepancy between the experimental and the simulated data can be attributed to several factors which are uncertain in the simulation. One of them is the lack of knowledge on the real form of the disorder potential. The simulation assumes only a structure of the disorder potential. But we cannot

¹We emphasize that the parameters V_0 and ℓ_c are the statistical parameters of the disorder potential. Therefore, different landscapes of the disorder potential can be realized for the same parameters V_0 and ℓ_c .

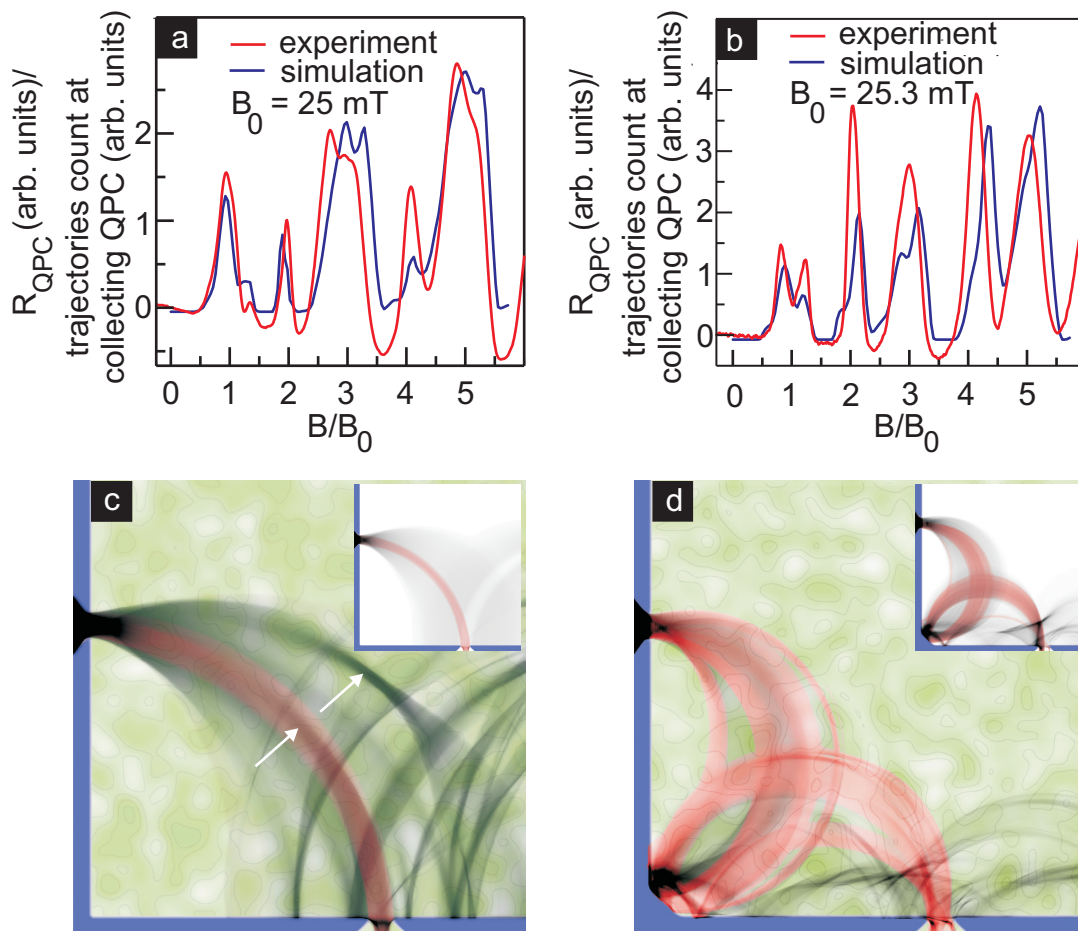


Figure 3.9: Comparison of experimental and simulated data. a) The magnetoresistance recorded in a type I corner device in comparison with a simulation of the number of trajectories entering the collecting QPC as a function of B/B_0 for the disorder potential landscape shown in panel c. b) Same as panel a for a corner device of type II. The disorder potential used in the simulation is shown in panel d and is distinct from the disorder potential used in a. c) Electron trajectories at the magnetic field B_0 in the presence of disorder. Disorder leads to the formation of branches indicated by white arrows. The inset shows the particle flow in a disorder-free landscape. d) Another realization of the disorder potential leads to a peak splitting (panel b). Though the particle flow is affected by the disorder at the field $2B_0$, a caustic still forms at the collecting QPC. The inset depicts the particle flow in the disorder-free potential. (The pictures are provided by Jakob Metzger and Ragnar Fleischmann.)

expect that the simulation reproduces completely the real shape of the disorder potential. It would be therefore enthralling to combine the technique of electron imaging ([39,45]) with the device characterization in DC-transport and numerical simulations in order to obtain more information about the disorder potential and correlate DC transport with imaging results. Also the outcome of a time-resolved transport experiment should indicate the structure of the disorder potential, as the electron travel time will depend on the path along which the electrons travel and thus on the shape of the disorder. Another uncertain factor is the height of the saddle potential

in the QPC. Our numerical simulation shows that the saddle potential affects the presence of the caustic peak at field $\sqrt{2}B_0$.

3.10 Ballistic cavities

A mesoscopic cavity is an alternative geometry that may be suitable for carrying out time-resolved experiments. The trajectories electrons run are defined by the strength of the magnetic field and the boundary conditions imposed by the cavity geometry. We seek a device which supports at least two electron trajectories of different length for which the electron returns to the injecting point contact. Time-resolved studies would no longer require a three chip configuration. A two chip configuration, where the mesoscopic device is on one chip and the photoconductive switch on the other, would be sufficient. This would represent an enormous simplification. One possible geometry is an equilateral triangle with a quantum point contact in the middle of one of its sides. The basic trajectories supported by this cavity are shown in Table 3.1. DC-transport experiments on such triangular cavities were performed only recently [46,47,48]. We have also considered square and hexagonal cavities. In both cases, a quantum point contact is placed in the middle of one of the cavity sides. In order to inject the electrons inside the cavity a small opening is fabricated in one of the corners, so that a bias can be applied. Table 3.1 lists the most prominent trajectories for the three cavity types that are investigated here. Also listed are their length and the time the electron travels before exiting the cavity.

We have experimentally investigated the DC-transport behavior of such cavities. The cavities are fabricated from the same modulation doped GaAs/AlGaAs heterostructure as the corner devices. The shape of the cavity is defined when a negative voltage is applied on two surface split gates. We first consider a triangular cavity (Fig. 3.10a) with a side length a of $3.5 \mu\text{m}$. The magnetotransport data, obtained for different gate voltages, are shown in Fig. 3.11. We can associate a number of the observed features with the prominent trajectories listed in Table 3.1. However, we also observe additional structures, which remain to be understood. The electron density in this experiment is $2.7 \cdot 10^{11} \text{ cm}^{-2}$. According to Table 3.1 we expect to see peaks at the following values of the magnetic field: $\pm 49 \text{ mT}$, $\pm 147 \text{ mT}$ and $\pm 245 \text{ mT}$. At high gate voltages we observe a peak at $\pm 42.5 \text{ mT}$. This peak can be attributed to the electron trajectory which

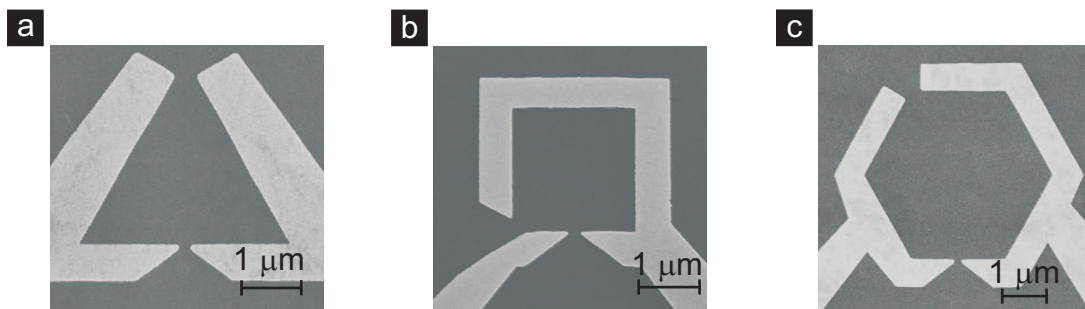


Figure 3.10: SEM pictures of ballistic cavities. a) equilateral triangular cavity with a side length of $3.5 \mu\text{m}$. b) square cavity with a side length of $2 \mu\text{m}$. c) hexagonal cavity with a side length of $2 \mu\text{m}$. The lithographic opening of the quantum point contact in all cavity types is 200 nm .










triagonal cavity	R	a = 3.5 μm		Number of reflections
		Length (μm)	Time (ps)	
	a/2	5.5	27.1	2
	a/6	12.8	63.2	8
	a/10	14.3	70.4	14
square cavity	R	a = 2 μm		Number of reflections
		Length (μm)	Time (ps)	
	∞	4.0	19.7	1
	a/2	6.3	30.9	3
	a/6	10.5	51.6	11
hexagonal cavity	R	a = 2 μm		Number of reflections
		Length (μm)	Time (ps)	
	∞	6.9	34.1	1
	3/2a	9.4	46.4	2
	a/2	18.8	92.9	5

Table 3.1: The most prominent electron trajectories in the different cavity types. Here R is the radius of the trajectory, a is the cavity side length. The third and fourth column show the length of the trajectory and the time an electron needs to traverse this trajectory. To calculate the traveled distance, Fermi velocity is assumed equal to $0.2 \mu\text{m}/\text{ps}$, a typical value for the experiments.

hits each cavity side in the middle. It shifts towards ± 45 mT as the gate voltage is lowered, while an additional peak emerges. At the largest negative gate voltage, a double peak structure is observed at ± 34 mT and ± 52 mT. Also at high voltages an additional peak has appeared near ± 97.5 mT. This peak may originate from trajectories with radius $R = a/4$, even though Linke et al. have predicted that this particular trajectory should not exist ([46]). At higher values of the magnetic field 146 mT, one can identify the trajectory with radius $R = a/6$ (see Table 3.1). However, we also observe a peak around ± 186 mT. This field comes close to the field value ± 196 mT, which would correspond to the trajectories with radius $a/8$. According to the stability diagram by Linke et al. this trajectory is also unstable ([46]). Here we can observe a strong and well-resolved peak. In short, some features can be identified unequivocally, while others have not been identified. Their appearance contradicts existing theory.

Another suitable cavity geometry is a square shape. The main trajectories, which can be supported by the cavity, are summarized in Table 3.1. Figure 3.12 shows the magnetotransport results on a square cavity with a side length of $2 \mu\text{m}$. A pronounced peak is present already

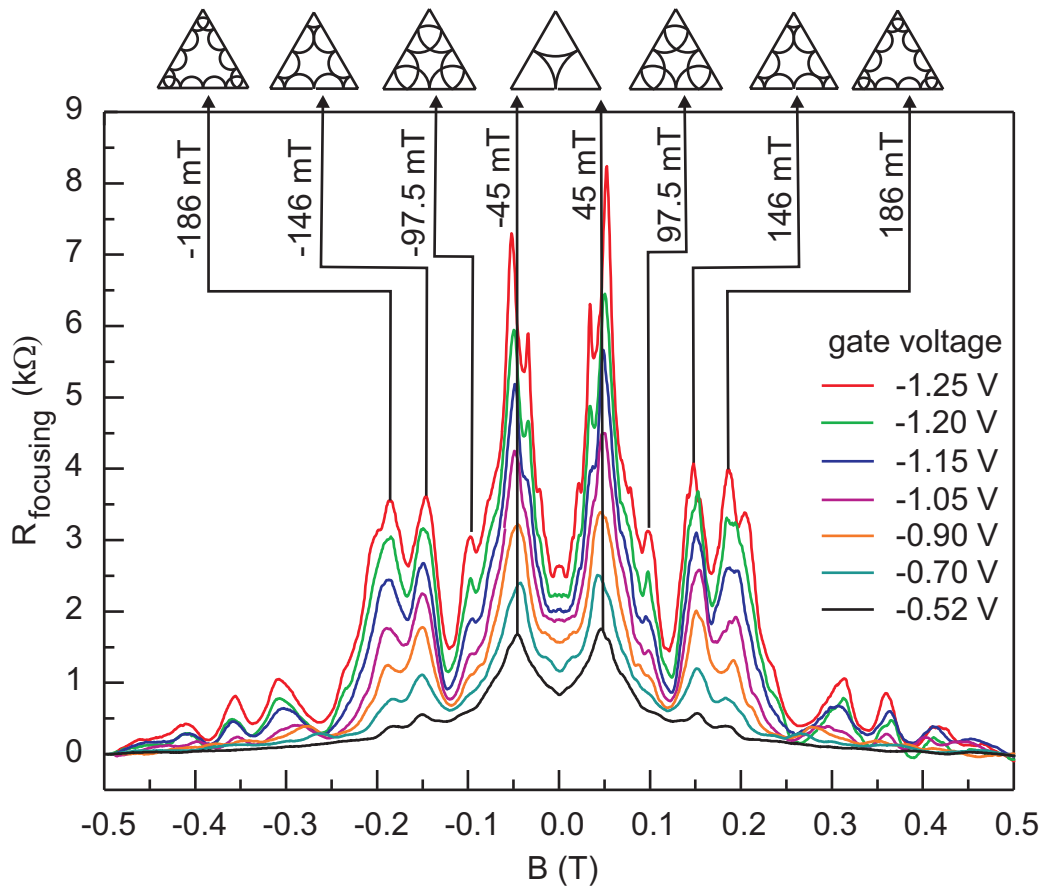


Figure 3.11: Magnetotransport data obtained for a set of gate voltages on a triangular cavity with a side length of $3.5 \mu\text{m}$. The top of the figure depicts the electron trajectories in the cavity which can be attributed to each peak.

at zero magnetic field. Ballistic electrons entering the cavity are reflected by the opposite wall back to the quantum point contact. As the magnetic field is turned on, the electron trajectory will bend and straight reflection back into the quantum point contact is suppressed. The next pronounced feature is associated with a trajectory where the electron hits each wall in the middle. This trajectory has a radius $a/2$, where a is the wall length. The position of this peak coincides very well with the predicted value from these classical considerations. The next peak is anticipated at $\pm 222 \text{ mT}$. The trajectory has been drawn at the top of Fig. 3.12. It is observed at significantly higher magnetic fields near 275 mT . Since this trajectory runs close to the walls, this discrepancy likely originates from soft-wall effects.

Finally we have investigated a hexagonal cavity with a side length of $2 \mu\text{m}$ (Fig. 3.10c). To the best of our knowledge, this geometry has not been studied previously. Magnetotransport data acquired for a set of different gate voltages are depicted in Fig. 3.13. The main trajectories are schematically drawn at the top of the graph. The electron density is $2.2 \cdot 10^{11} \text{ cm}^{-2}$. As argued in the discussion about the square cavity, there must also be a peak in the hexagonal cavity at zero magnetic field. A strong peak, as observed in the square cavity in Fig. 3.12, is however missing. The next peak is expected near 26 mT . A feature is indeed observed, albeit at a slightly higher value of the magnetic field (29.5 mT). This peak exhibits some fine structure and is

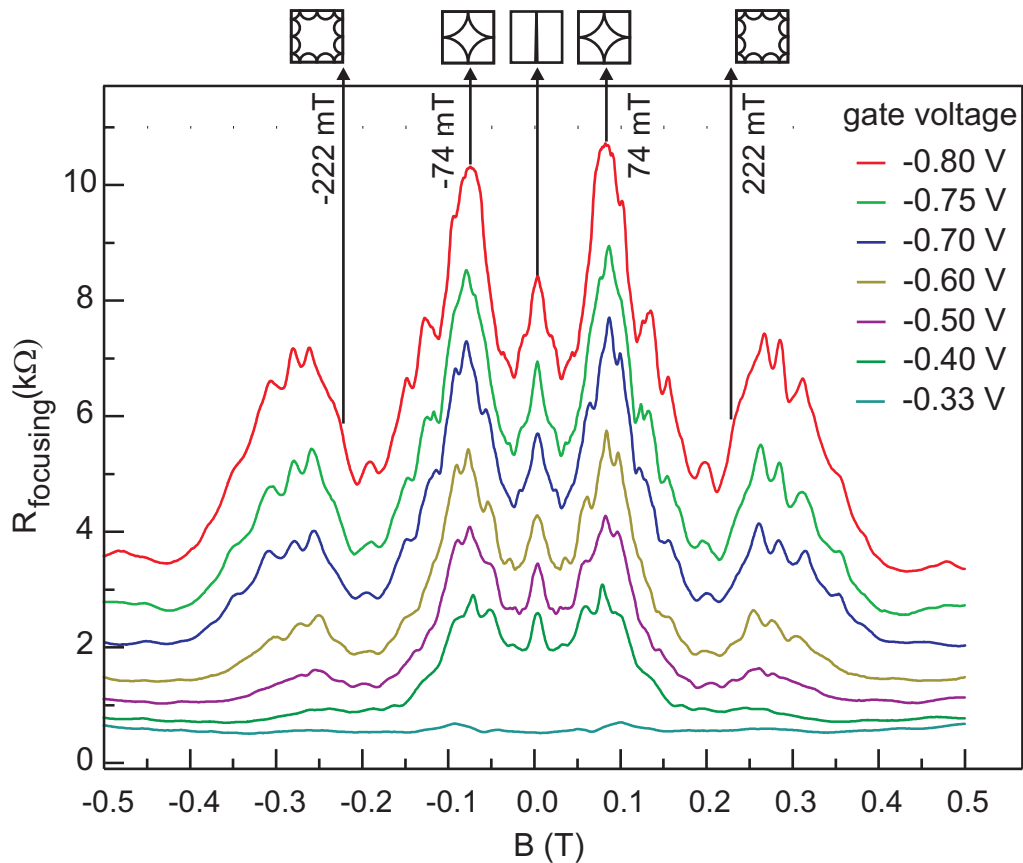


Figure 3.12: Magnetotransport data obtained for a set of gate voltages on a square cavity with a side length of $2 \mu\text{m}$. The position of the first and the second peak coincides well with the expected values of the magnetic field. The third peak, however, is shifted to higher fields. The electron trajectories, which are associated with each peak, are shown at the top of the figure.

rather weak. A more pronounced peak is seen at $\pm 75.7 \text{ mT}$. It coincides with the theoretically expected value for a trajectory where the electron hits each of the six walls in the middle. The higher order peaks are more difficult to account for. A dominant feature occurs at 132 mT when applying low gate voltages. As the gate voltage is lowered to more negative values, the peak shifts to higher values of the magnetic field. At the most negative gate voltage the peak occurs at 150 mT . The best candidate trajectory to account for this peak has a radius $R = a/4$. It would form at a magnetic field value of 155 mT . Since the trajectory gets close to the corner, the details of the corner may matter and may be responsible for the deviation in the experiment.

The mesoscopic cavities exhibit a wealth of magnetoresistance peaks with their substructures. The position of some peaks coincides with the intuitive picture of electron trajectories in the cavity. The others cannot be explained in a simple manner. A complete analysis of cavities should include a calculation for the stability of electron trajectories. Also the influence of the disorder potential may not be neglected, as was impressively shown in the experiments on corner devices.

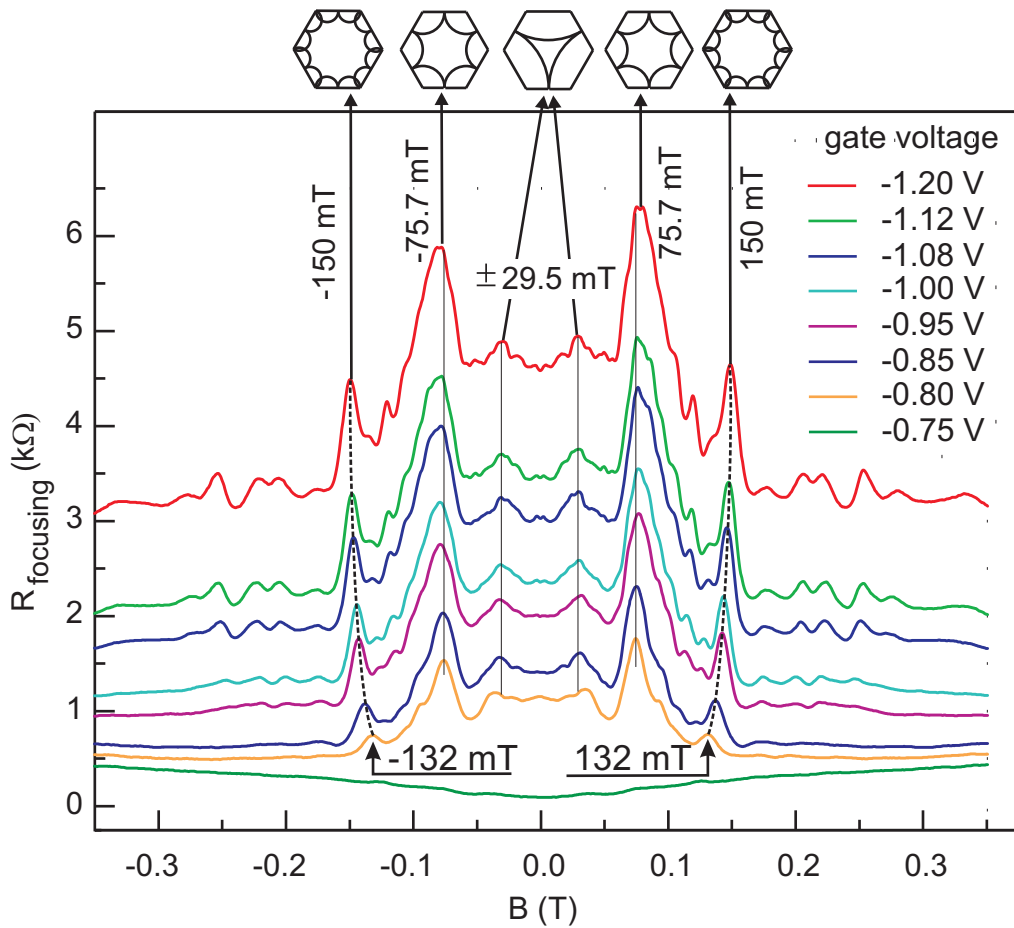


Figure 3.13: Magnetotransport data obtained for a set of gate voltages on a hexagonal cavity with a side length of $2 \mu\text{m}$. The dashed lines are guides to the eye and show how the peak moves from 132 mT to 150 mT as the QPC' resistance increases, i. e. the gate voltage is lowered.

Chapter 4

Time Resolved Experiments

In this chapter the experiments on time-dependent transport in a two-dimensional electron gas are described. We start discussing the experiments performed on a corner device, whose geometry is defined by applying negative voltages on top gates; we deplete the 2DES beneath the top gates. We perform then experiments on a corner device defined by wet chemical etching. The last geometry, which we consider here, is a stripe of a two-dimensional electron gas. In a magnetic field its excitations show various modes of bulk and edge magnetoplasmons. We also measure the propagation velocity of the excitations in the stripe.

4.1 Time-dependent measurement on a corner device

The chip assembly for the time-resolved transport experiment is shown in Fig. 4.1. The left and the right part of the assembly is made of the photoconductive material ErAs:InGaAs with 20 nm period [20]. The photoconductive switches are patterned on this material, as indicated in Fig. 4.1, and integrated into the coplanar waveguide as it was discussed in Chapter 1. Each switch acts either as a source of short electrical pulses or as a detector of an ultrafast signal. The central part of the assembly contains an active device fabricated from a GaAs/AlGaAs heterostructure. At the interface between the chips, the silver epoxy droplets (Fig. 4.1) provide an electrical contact between the different sections of the coplanar waveguide. The three-chip assembly is fixed in a chip carrier and the optical fibers are glued above the photoconductive switches with an optical adhesive. Figure 4.2 shows the final setup.

4.1.1 Gate defined corner device

A magnified image of the active device is shown in Fig. 4.3a. The corner device is patterned on top of the mesa by fabricating gates with e-beam lithography and metal evaporation. Figure 4.3b shows the electron microscope picture of the corner device. The central line of the waveguide, which goes from the photoconductive switches, terminates at the left and the right ohmic contact. The ground planes of the waveguide are interrupted by the leads which contact the e-beam structure and the ohmic contacts.

We first measure the magnetotransport in the DC regime. We drive the current between the contacts 1 and 2 and measure the voltage drop over the detector QPC between the contacts 2

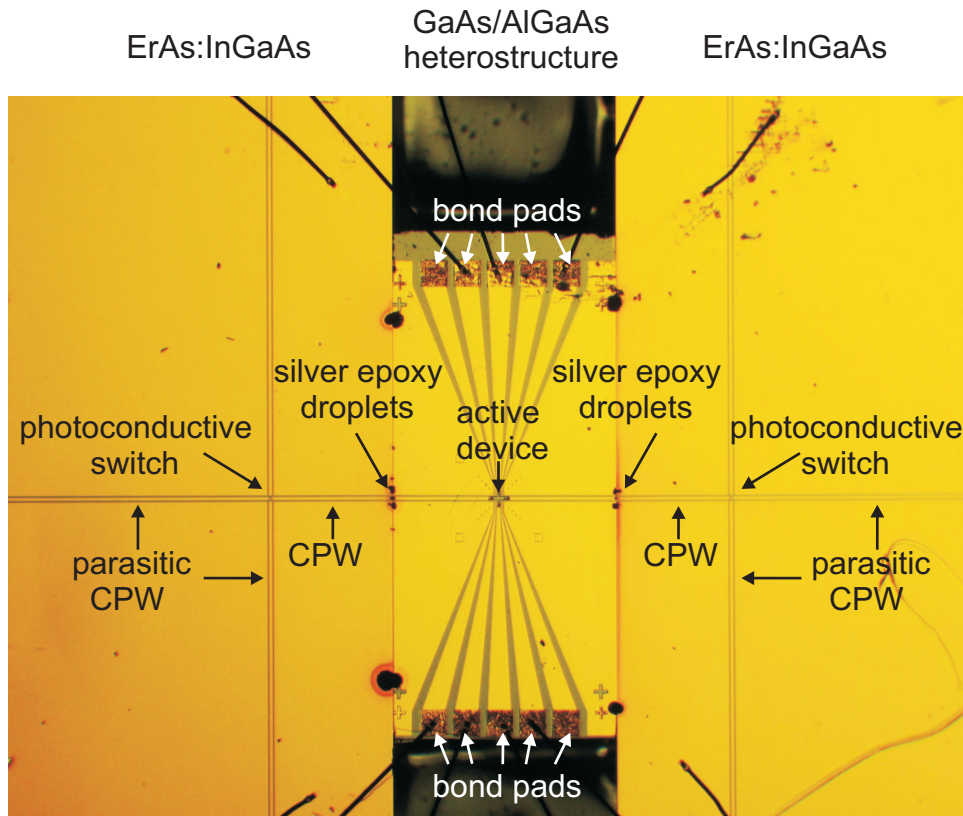


Figure 4.1: Three-chip assembly for the time-resolved transport experiment on a device made from a 2DES. The left and the right chips are fabricated from ErAs:InGaAs photoconductive material and contain the photoconductive switches. The central chip is fabricated from a GaAs/AlGaAs heterostructure and contains the 2DES. The distance between the switches is 2.9 mm; the length of the central chip is 1.5 mm, the distance from each switch to the interface is 0.7 mm.

and 3. The blue trace in Fig. 4.4 represents the experimental result when the laser light was on. The arrows indicate the position of the magnetoresistance features due to electron ballistic transport. The operation of the device changes, however, substantially when the laser light is turned on. The red curve depicts the measurement recorded shortly after the laser light was turned on. The curve became noisy even though we still can recognize the ballistic peaks. A further characterization of the device shows that the resistance of the quantum point contacts changes with time and is unstable when the light is incident on photoconductive switches. The repetition of the same magnetotransport measurement does not show even those two ballistic peaks.

4.1.2 Etched corner device

Instead of defining the corner device with top gates, we etched the structure of the corner device as shown in Fig. 4.5. Note, that the overall chip assembly has not been modified. Only the ground planes of the waveguide have been altered in the vicinity of the active device (Fig. 4.5a). The ground planes are no longer interrupted to accommodate leads that contact topgates. As a

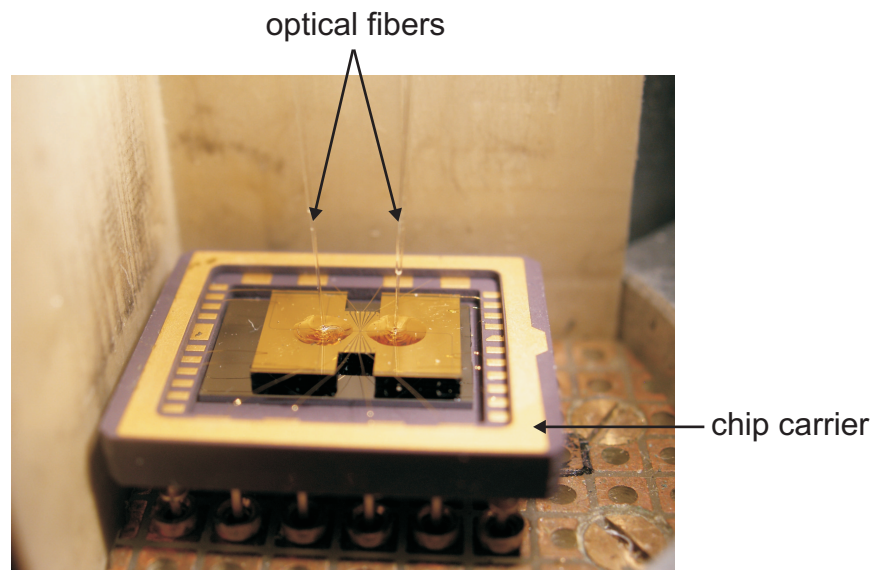


Figure 4.2: Chip carrier with a three-chip assembly. Optical fibers are fixed above the photoconductive switches with an optical adhesive.

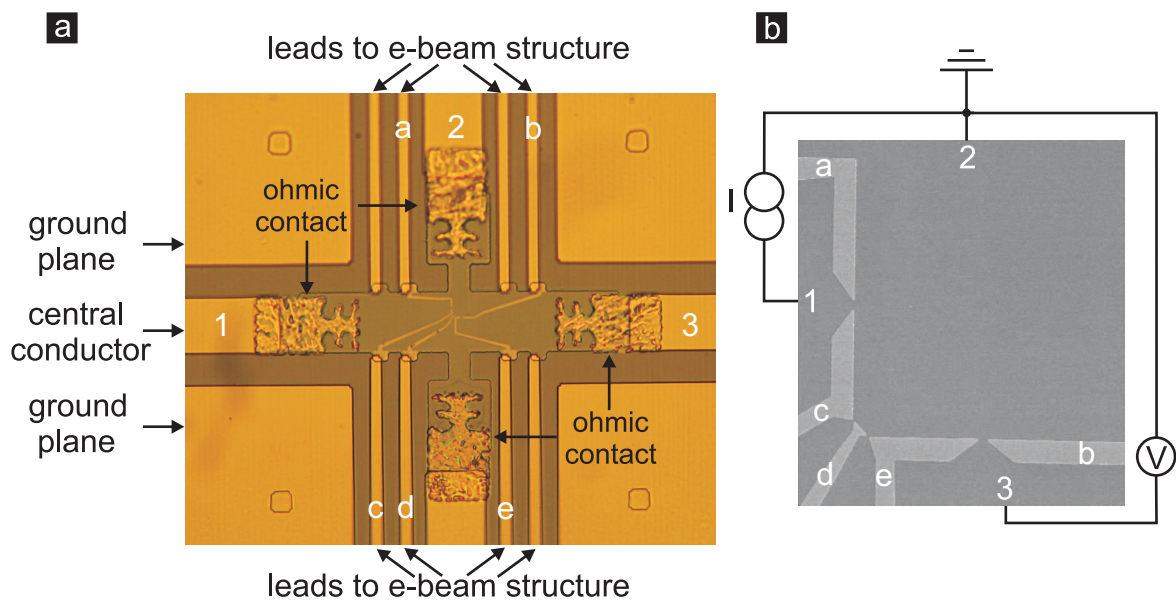


Figure 4.3: a) Magnified image of the active device. A corner device is patterned on top of the mesa. Several electrodes contact the corner device. A DC bias voltage applied to the electrodes depletes the 2DES and forms the corner device. Four ohmic contacts marked in the picture are alloyed to the 2DES. The central line of the coplanar waveguide terminates at the left and right ohmic contacts. b) Electron microscope picture of the corner device structured in the middle of the mesa. In DC transport experiments the current is driven between contacts 1 and 2, while the voltage is measured across contacts 2 and 3.

result we expect fewer reflections of the propagating wave (see Chapter 1). The ground planes

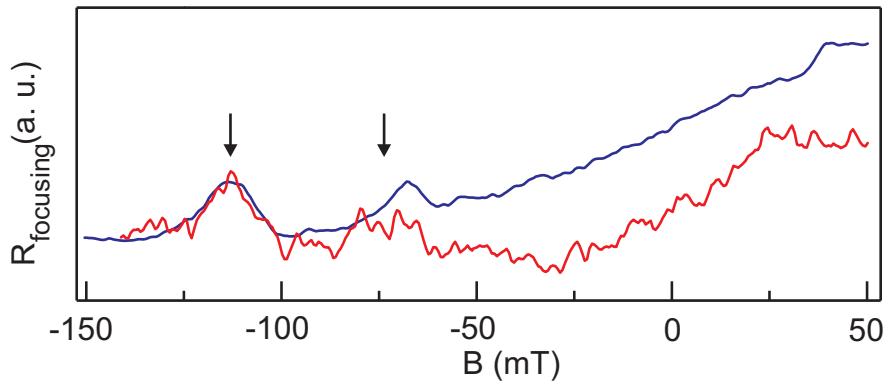


Figure 4.4: Magnetoresistance traces are measured on a corner device whose geometry is defined with surface gates. The blue curve is obtained for the case when the laser light was off. The red curve is obtained when the laser light was on. The arrows point the position of the magnetoresistance peaks due to ballistic electron transport in the corner device.

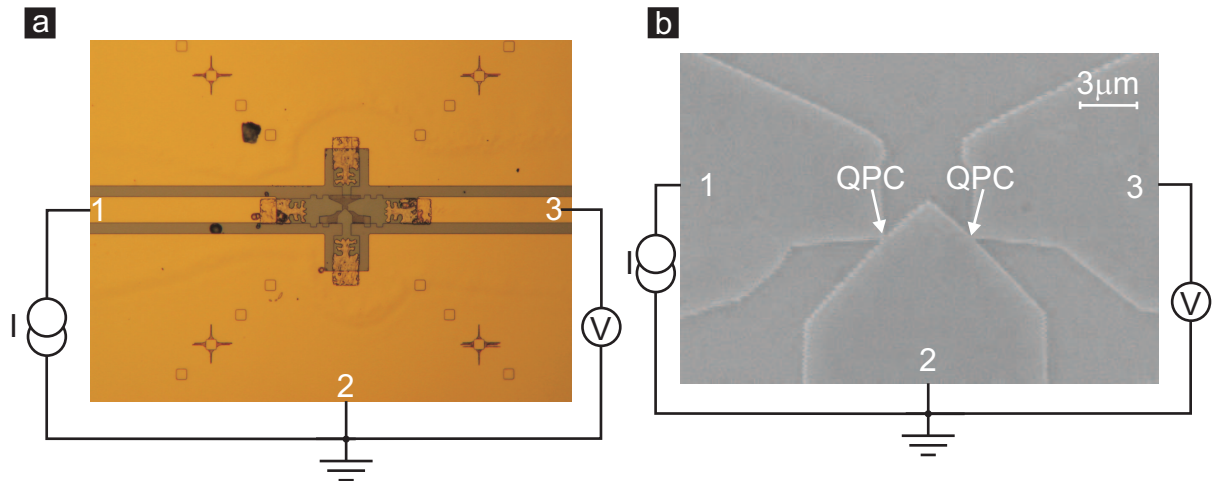


Figure 4.5: a) Corner device is fabricated by etching the mesa of the two-dimensional electron gas. b) Electron microscope picture of the etched corner device in the middle of the mesa.

are now used to contact the upper and lower ohmic contacts, while the central conductor of the waveguide still contacts the left and right ohmic contact. We characterize the corner device in DC transport. Here, we drive the current between the contacts 1 and 2 and measure the voltage drop between the contacts 2 and 3 as a function of the magnetic field applied perpendicular to the 2DES plane. Figure 4.6 compares the magnetotransport traces obtained in this three-terminal measurement when the laser light was on and off. Magnetoresistance peaks are superimposed on top of a rising background, with a slope corresponding to the hall resistance [34]. The measured signal also contains the contact resistance of contact 2 shared between the current drain and the voltage tap. The arrows in Fig. 4.6 point the position of the magnetoresistance peaks. Even though they are weak, the etched devices can be operated in a stable fashion even in the presence of stray light of the laser pulse. In the time-resolved experiment contact 2 is

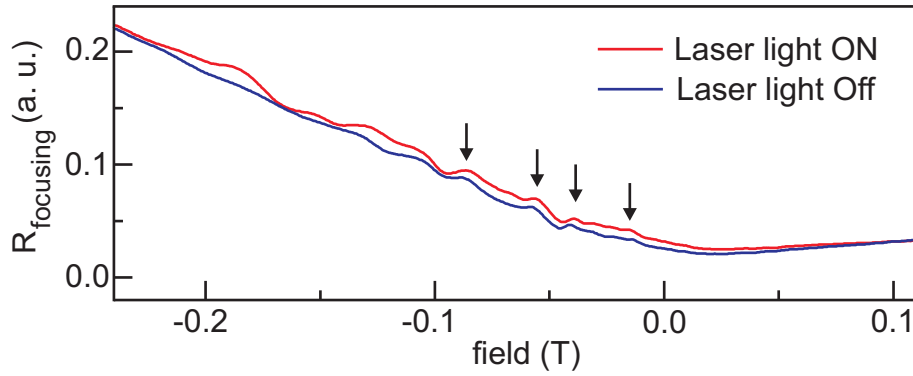


Figure 4.6: DC characterization of the corner device in a three-terminal configuration. The arrows indicate the position of the magnetoresistance peaks.

grounded, all others are floating. We apply a voltage on one of the photoconductive switches and sample the signal on the second photoconductive switch as we described in Chapter 1. The data acquisition for time-dependent transport in the magnetic field proceeds as follows. For a given position of the stepper motor, i.e. delay τ between the pump and probe beam, the signal is recorded from the oscilloscope screen for discrete values of the magnetic field. Thereafter the stepper motor is moved to the next position and the signal is recorded for the same discrete values of the magnetic field. The measurement result is represented by concatenating the traces along the time axis for the same magnetic field values. The raw experimental data are displayed in color rendition in Fig. 4.7a. Unfortunately, no magnetic field dependent features are observed. Rather it shows a pattern of magnetic field independent lines. In the hope, to identify magnetic field dependent signal, the magnetic field independent features were subtracted. They are associated with the waveguide structure as will be shown in the course of this chapter. We first Fourier transform the data along the field axis for every point on the time axis. The Fourier component at zero frequency contains the magnetic field independent signal. Hence, we set this component to zero and perform the inverse Fourier transform. The result of this data analysis is depicted in Fig. 4.7b. It does not show magnetic field dependence, which could be attributed to the ballistic electron transport in the corner device. Analog to the DC transport measurement, we anticipate to observe the features of the electron ballistic transport, when we integrate the signal along the time axis in Fig. 4.7 for every value of the magnetic field. The result of the integration is shown in Fig. 4.8. The ballistic peaks are not distinguishable in the noisy signal.

The experimental configuration can be improved in several ways. The geometry of the corner device should be optimized so that the four-terminal measurement of DC transport is possible. It avoids the increasing background with the magnetic field (see Fig. 4.6) and therefore eases the identification of the ballistic peaks. Further, in order to increase the signal the impedance of the quantum point contacts should be increased, which implies that the geometrical opening should be made smaller.

In order to understand the effect of the short electrical pulse on a two-dimensional electron gas, we simplify the geometry of the integrated active device even more.

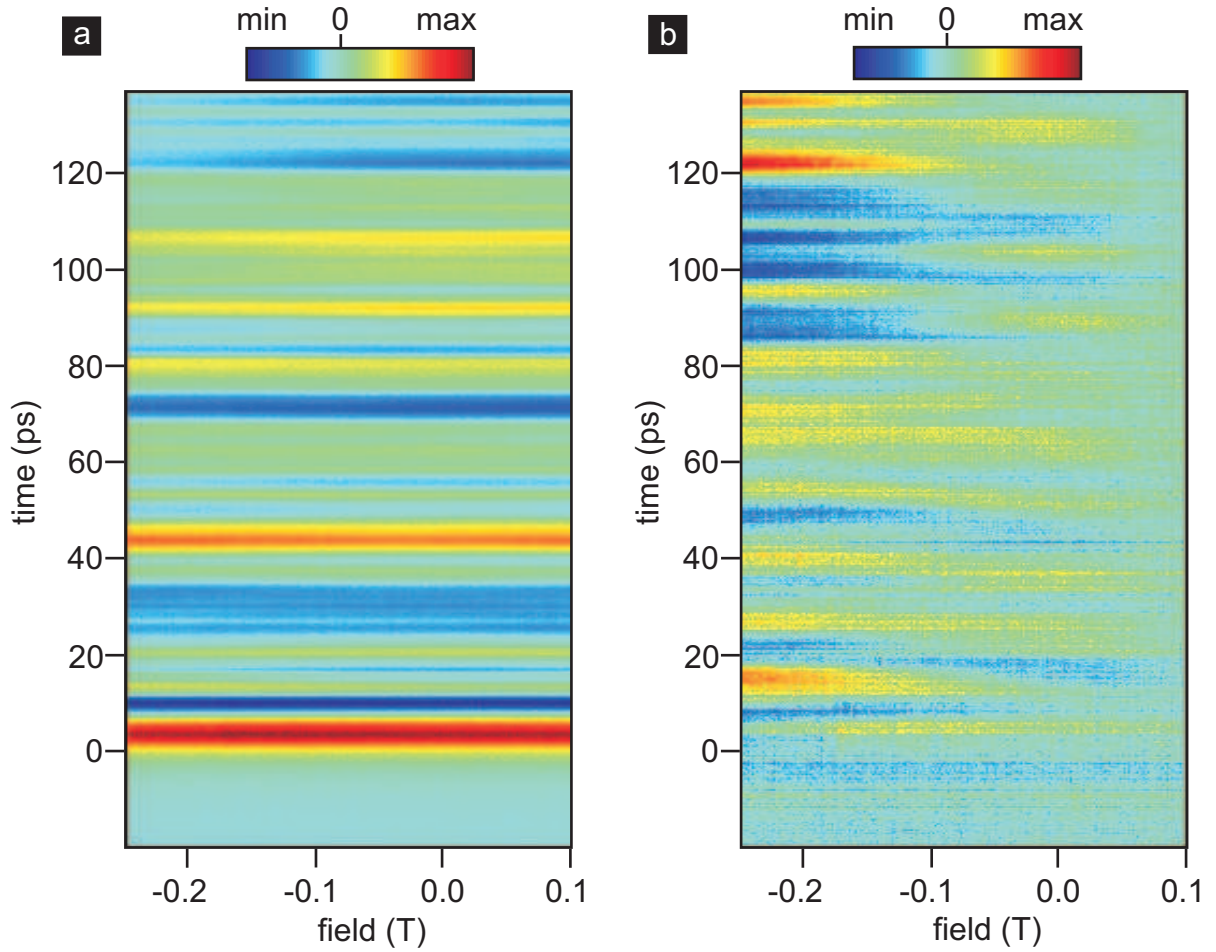


Figure 4.7: Time-dependent response of the etched corner device. a) raw experimental results are obtained by reading out the signal at the detector switch traces from the oscilloscope screen for every value of the magnetic field and by subsequent concatenating the corresponding traces. Magnetic field independent signal is superimposed on a magnetic field dependent signal. b) Magnetic field dependent signal is obtained by filtering out the DC component along the magnetic field axis for every point on the time axis.

4.2 Time-dependent transport on a stripe of the 2DES

Here, we remove both the upper and the lower ohmic contacts in Fig. 4.3, so that only two ohmic contacts (left and right) are left. No additional features are etched or written with e-beam lithography. The central line of the coplanar waveguide terminates at each contact. This device, called stripe, is depicted in Fig. 4.9. Note, that the corner device is not structured on mesa. The distance between the ohmic contacts is $60 \mu\text{m}$ and the width of the stripe is $20 \mu\text{m}$. The sample is cooled down to 1.4 K and the electron density of $n = 0.6 \cdot 10^{11} \text{ cm}^{-2}$ is measured in a two-terminal transport configuration in a perpendicular magnetic field.

After this initial sample characterization, we determine the zero time point, which is when the two optical pulse trains arrive simultaneously at the photoconductive switches. This proce-

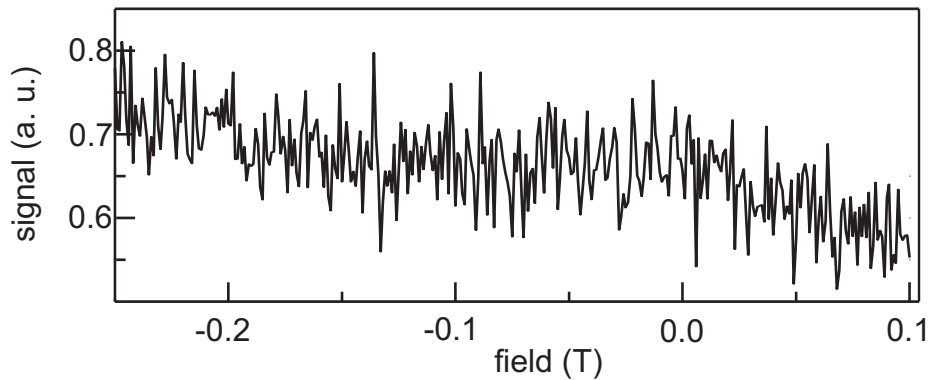


Figure 4.8: The signal from Fig. 4.7a is summed along the time axis for every value of the magnetic field. This data analysis does not show the signal of the electron ballistic transport in the corner device.

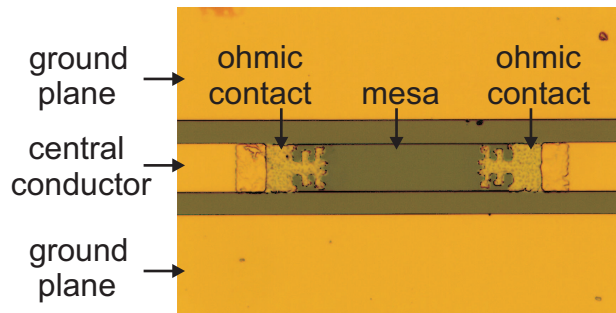


Figure 4.9: The device under study is a $60 \mu\text{m}$ long stripe of a 2DES. Two ohmic contacts are alloyed to the 2DES. The central line of the coplanar waveguide terminates at either of the ohmic contacts.

procedure was already applied in the experiments described in Chapter 1. Therefore we implement the photoconductive sampling technique and exploit the symmetry of the chip assembly. A bias voltage is applied at one of the switches, which assumes the role of the source switch. The photocurrent, which flows through the other (detector) switch, is measured as a function of the delay time between the optical pulse trains. It is sufficient to determine the zero time point at zero magnetic field. In Fig. 4.10 the trace along the positive direction of the time axis is acquired for the case when the switch on the left side of the 2DES stripe acts as the source and the switch on the right side of the 2DES stripe acts as the detector. The second trace is depicted along the negative time axis and is acquired for the case when the roles of the switches are interchanged. Both traces are symmetric with respect to the desired zero time point, which is indicated by an arrow in Fig. 4.10. Since the propagation velocity of the electrical pulse along the waveguide is $0.32c$ and the total distance between the switches is 2.9 mm , we conclude that the peaks at 0 ps and -53 ps correspond to the direct pulse propagation from the source switch to the detector switch, as if the stripe of the 2DES acts as an extension of the central line of the coplanar waveguide.

Figure 4.11a shows the time-dependent response in a magnetic field of the $60 \mu\text{m}$ long stripe to the excitation with a single electrical pulse. The signal is recorded for 351 discrete values

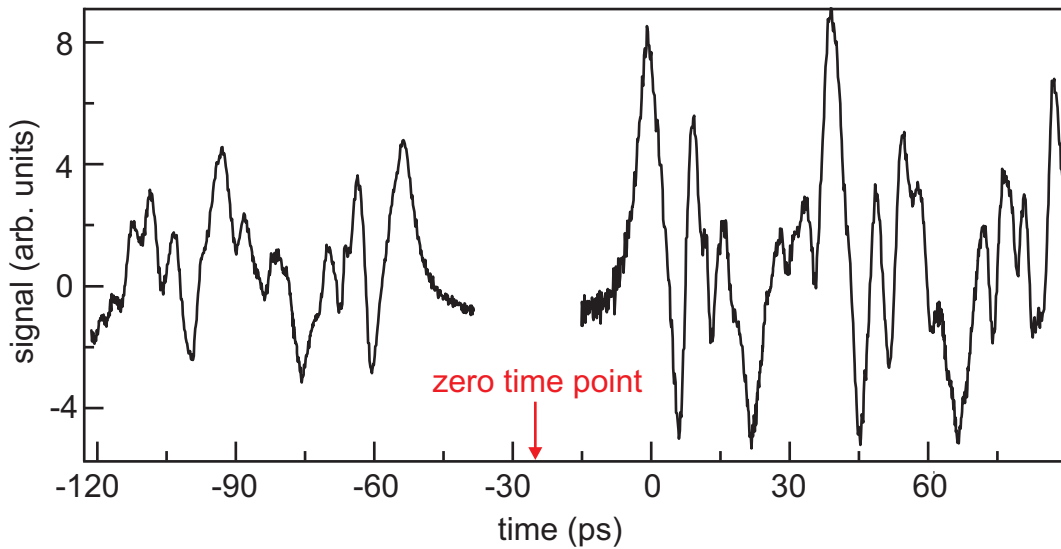


Figure 4.10: Traces of the pulse propagation between the source and the detector switch allow for the zero time point determination. The trace along the positive direction of the time axis is measured when the left switch is the source and the right switch is the detector. The first peak appears at the delay time of 0 ps. The trace along the negative direction of the time axis is obtained when the role of the switches is interchanged. The first peak appears at the delay time of -53 ps. The time point, when the two optical pulse trains arrive simultaneously at the photoconductive switches, is in the middle between the two traces and is indicated by the red arrow.

of the magnetic field between -1 T and 1 T in equidistant steps. The figure depicts magnetic field independent signal and indicates magnetic field dependent signal. Note, that the time axis is the same as in Fig. 4.10. The line at the delay time of 0 ps corresponds to the direct pulse propagation between the source and the detector switch and is independent of the magnetic field. This assures us that this electrical pulse is bound to the waveguide structure and not to 2DES. To bring out magnetic field dependent features it is convenient to subtract the magnetic field independent component along the magnetic field axis for every point on the time axis. Alternatively, we can perform a Fourier transform along the magnetic field axis for every value of the delay time and set the zero frequency Fourier component to zero. By performing the inverse Fourier transform we filter out magnetic field independent features in the time domain. Figure 4.11b shows the result of the initial data analysis. While the signal at zero delay time vanishes completely, a peak shows up at 16 ps. This peak is interpreted as an excitation of the 2DES that propagates from one end of the stripe to the other. Apart from a rich set of extremes at zero magnetic field, Fig. 4.11b shows the lines which move up as well as down in time as the magnetic field increases. We will show below that the Fourier transform of these time dependent signals yields a reach spectrum of excitations associated with the plasmon modes of the 2DES.

4.2.1 Plasmon modes in 2DES

The theory of plasmons [49] has been sufficiently covered in the literature [50, 51, 52, 53, 54]. We only point out that plasmons are collective excitations of charge carriers in metals or semi-

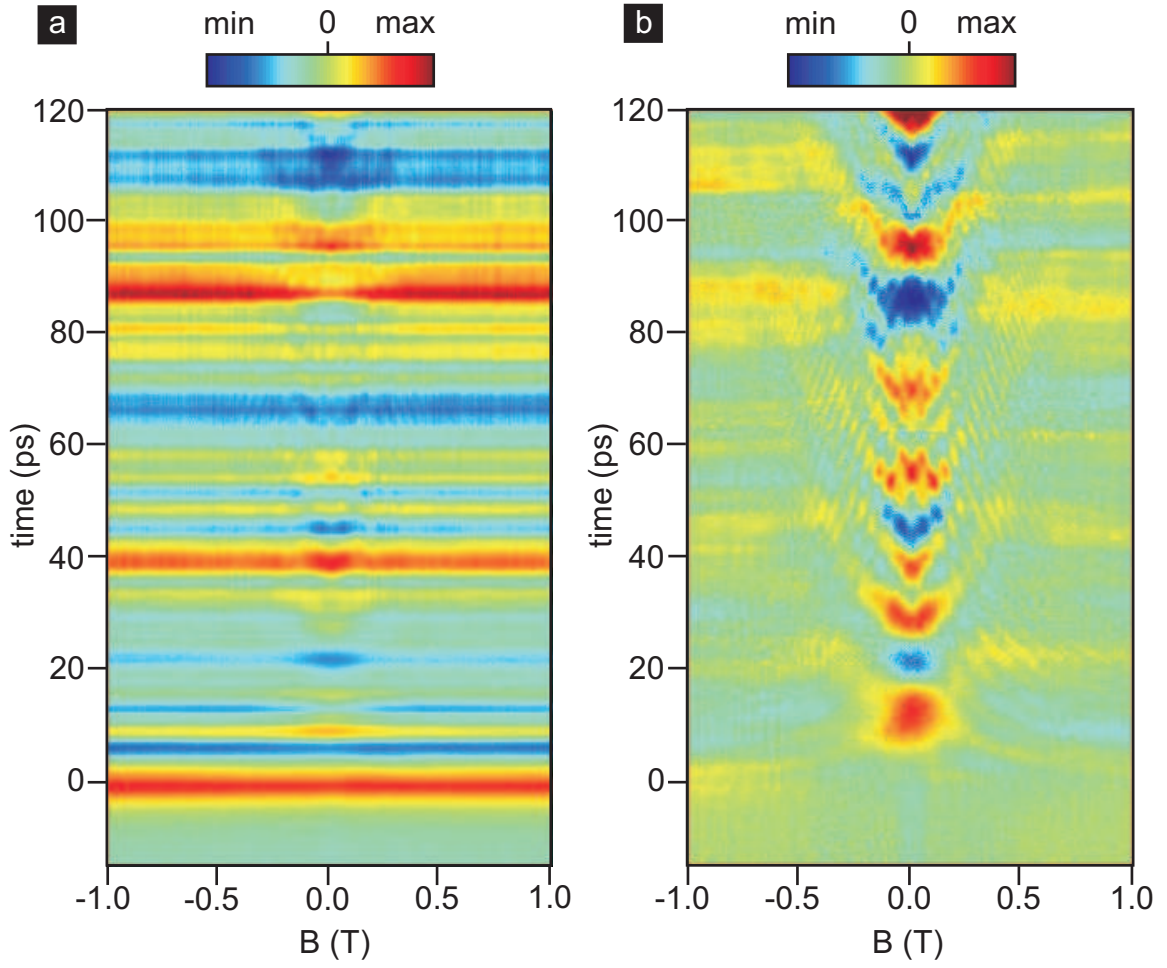


Figure 4.11: Time-dependent response of the stripe with a length of $60 \mu\text{m}$ and a width of $20 \mu\text{m}$. The electron density is $n = 0.6 \cdot 10^{11} \text{ cm}^{-2}$ is achieved after the sample is cooled down to 1.4 K . a) raw experimental data. A magnetic field independent signal dominates, but is superimposed on a magnetic field dependent signal. b) Magnetic field dependent signal is obtained by subtracting the magnetic field independent component along the magnetic field axis for every point on the time axis.

conductors. In the two-dimensional case the plasmon dispersion at zero magnetic field is

$$\omega_p^2 = \frac{ne^2}{2m^*\epsilon\epsilon_0}k + \frac{3}{4}v_F^2k^2, \quad (4.1)$$

where n is the electron density, e is the electron charge, m^* is the effective electron mass, ϵ is the dielectric constant of the medium and k is the wave vector of the excitation. The second term includes electrodynamic effects, such as retardation effect, and should be accounted for when the phase velocity of the plasmons approaches the light velocity c [55,56]. In the approximation of small wave vector k ($v_F < \omega/k$), the second term can be neglected and one obtains:

$$\omega_p^2 = \frac{ne^2}{2m^*\epsilon\epsilon_0}k. \quad (4.2)$$

In a magnetic field applied perpendicular to the 2DES plane the plasmon excitation couples to the electron cyclotron motion. This coupling leads to a hybridization of the plasmon and cyclotron resonance mode [57]. The hybrid mode has a resonance frequency at:

$$\omega_{bmp}^2 = \omega_c^2 + \omega_p^2, \quad (4.3)$$

where $\omega_c = eB/m^*$ is the electron cyclotron resonance frequency in magnetic field B . This mode is associated with charge oscillations across the entire system. They are therefore referred to as bulk modes. Note, the bulk magnetoplasmon frequency increases with the magnetic field and approaches the electron cyclotron resonance frequency at high magnetic field ($\omega_c \gg \omega_p$).

The other type of excitation is bound to the edge of the sample and is called edge magnetoplasmon [58, 59, 60]. Here an edge is a fully or partially depleted region of the bulk 2DES. The depletion can be achieved either by applying a voltage to the top-gates or by etching of the 2DES material. The depletion at the edge causes the charge density, and thus the potential, to vary with the distance perpendicular to the edge. If then a charge is moved against the edge, the restoring force due to the potential shape at the boundary leads to various resonance conditions. The frequency of edge magnetoplasmon is given by:

$$\omega_{emp} \approx \frac{ne^2}{2\pi\epsilon\epsilon_0 B} k \ln\left(\frac{1}{|k|a}\right), \quad (4.4)$$

where a is a characteristic length of the boundary strip to which the charge oscillations are confined, n is the electron density far away from the boundary and k is the wave vector of the plasmon. Note, the edge magnetoplasmon frequency decreases with the magnetic field. This dispersion relation in Eq. 4.4 had been obtained for an abrupt drop of the electron density near the boundary. For a realistic edge potential profile the electron density changes smoothly at the vicinity of the edge. In this case, additional edge modes coexist. These acoustic modes [57] have a linear dispersion given by

$$\omega_j = \frac{ne^2}{2\pi\epsilon\epsilon_0 B} k/j, \quad j = 1, 2, \dots \quad (4.5)$$

4.2.2 Fourier spectrum

We now return to the experimental data in Fig. 4.11. At every value of the magnetic field, the data in Fig. 4.11b is numerically Fourier transformed along the time axis. The result of the Fourier transform comprises the real part and the imaginary part, from which the phase of the Fourier transform can be obtained by evaluating the arctangent of the ratio of the imaginary and the real parts for every data point. Panels a and b in Fig. 4.12 show color renditions of the real part and the phase of the Fourier transform respectively¹. The phase jumps form contours that either increase in frequency with increasing magnetic field or the frequency drops to zero in the large field limit. Apparently these phase jumps are closely connected to the bulk and edge magnetoplasmons of the 2DES. We attempt to identify these modes. We first focus on the

¹We point out that the excitation spectrum can also be obtained when the raw signal in Fig. 4.11a is Fourier transformed first along the time axis and the magnetic field independent features are filtered out afterwards. The spectra extracted with both methods do not differ significantly. In this chapter we use the first approach, i.e. the magnetic field independent features are removed before the excitation spectrum is extracted.

bulk magnetoplasmon modes whose frequency increases with the magnetic field. We determine their frequency at zero magnetic field and thereafter assign a wave vector to each of the observed resonances. The attempts to fit the observed branches using Eq. 4.3 did not deliver satisfactory results; the bulk magnetoplasmon frequency does not approach the electron cyclotron frequency at high magnetic field ($\omega_c \gg \omega_p$). Therefore we use the following function to fit each bulk magnetoplasmon branch:

$$f_{bmp} = \sqrt{f_p^2 + (C \cdot f_c)^2}, \quad (4.6)$$

where $f_p = \frac{1}{2\pi}\omega_p$ is the fit parameter for the plasmon frequency at zero magnetic field. f_c is calculated for an effective electron mass $m_e=0.068m_0$. C is another fit parameter that corrects

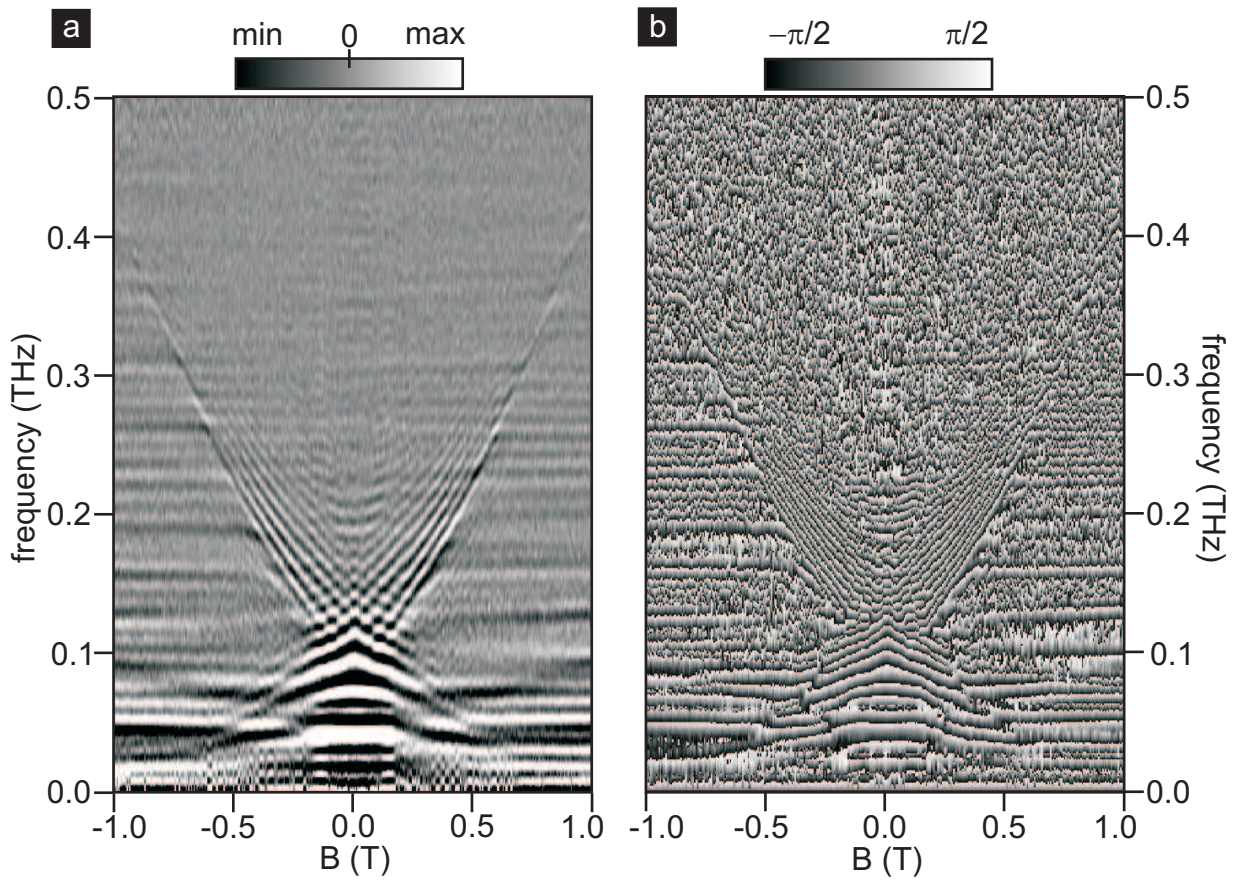


Figure 4.12: Fourier spectrum of the time domain data shown in Fig. 4.11b. a) The real part of the Fourier transform of the time-dependent data shown in Fig. 4.11. Two types of excitation are seen: bulk magnetoplasmons and edge magnetoplasmons. The frequency of the bulk magnetoplasmons increases in the magnetic field, while that of the edge magnetoplasmons decreases in the magnetic field. The spectrum shows several modes of each excitation type. b) Phase of the Fourier transform of time-dependent signal shown in Fig. 4.11. The phase shows also spectral components whose frequency increases/decreases in the magnetic field. The phase change between $\pi/2$ and $-\pi/2$ indicates the resonance condition.

for the cyclotron resonance frequency $f_c = \frac{1}{2\pi}\omega_c$. C would for instance account for deviation of the effective mass from this value. The dashed red lines in Fig. 4.13a are the best fits of the first eight branches. The fit parameters are summarized in Fig. 4.13b. The last row shows that the cyclotron resonance frequency has to be corrected by about 10% to 15%. For clarity, we assign a mode number to every branch; this number is given in the first row of the table. For comparison, Fig. 4.14 shows the same fits plotted on the real part of the excitation spectrum. It shows that the branches run along the border between black and white regions.

The edges and ohmic contacts of the 2DES impose boundary conditions for the plasmon

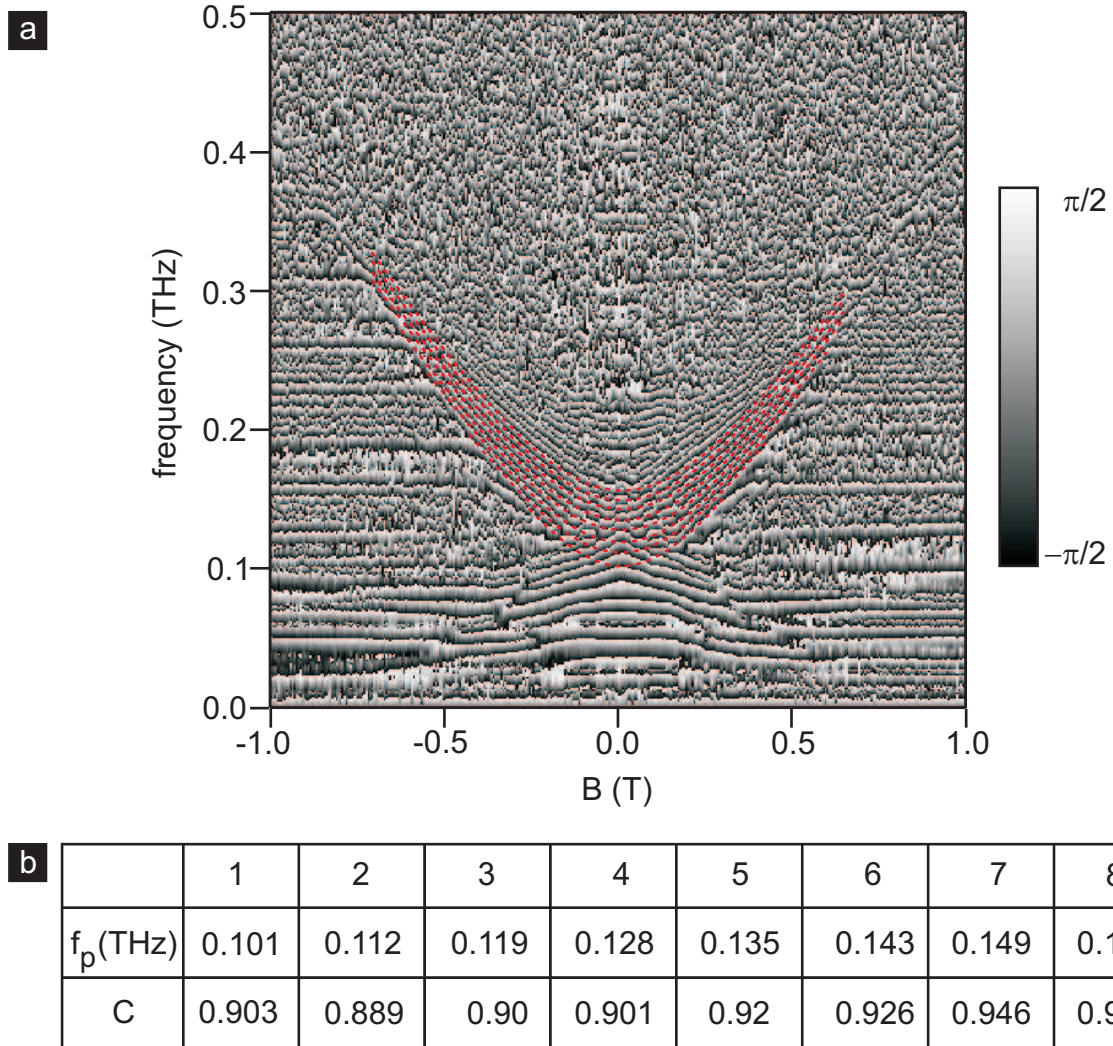


Figure 4.13: a) The phase component of the Fourier transform with a best fit of the first eight branches of the bulk magnetoplasmon modes of a 2DES stripe with a length of $60 \mu\text{m}$ and an electron density $0.6 \cdot 10^{11} \text{ cm}^{-2}$. The abrupt change of the phase from $\pi/2$ to $-\pi/2$ is taken as a signature of a resonance. b) Parameters f_p and C which yield the best fit for the bulk magnetoplasmon modes. The parameter f_p is the plasmon frequency in zero magnetic field and C is a correction factor of the cyclotron resonance frequency.

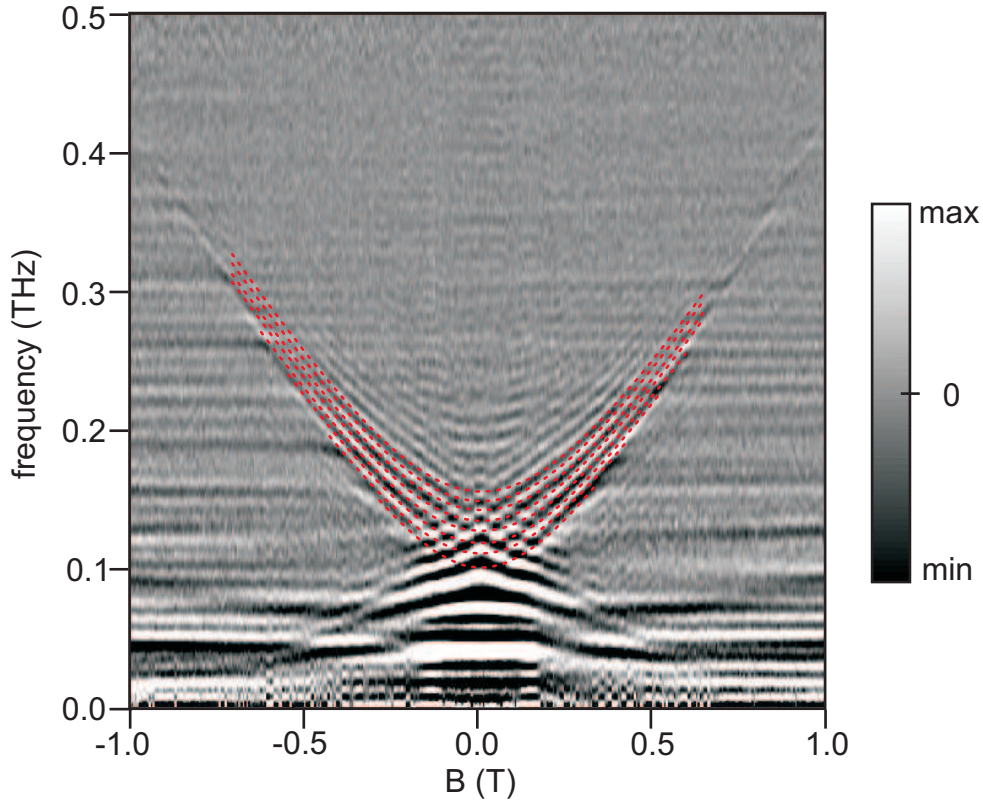


Figure 4.14: The real part of Fourier transform with several modes of bulk excitation of time-dependent signal shown in Fig. 4.11. Two types of excitation are visible: bulk magnetoplasmons and edge magnetoplasmons. The frequency of the bulk magnetoplasmons increases in the magnetic field, while that of the edge magnetoplasmons decreases in the magnetic field. Several branches of each excitation type indicate the excitation of different modes. Red dashed lines represent a best fit to the data using the bulk magnetoplasmon formula of Eq. 4.6. These best fits run along the boundary between the white and dark region.

excitations that can be excited in the 2DES. We anticipate that the characteristic dimensions of the 2DES accessible (its width and length) determine and quantize the wave vector of the plasmon modes. It is plausible to assume that the observed branches correspond to magnetoplasmon modes at the fundamental wave vectors and higher orders thereof. For a 2DES with a length L and width w , we expect the following wave vectors to be relevant:

$$k(j, i) = \left(j \frac{\pi}{L}, i \frac{\pi}{w} \right), \quad (4.7)$$

where $i, j = 0, 1, 2, \dots$

In the remainder of this section we attempt to confirm this hypothesis and identify the observable excitation modes. The wave vector can be determined from the frequency of each plasmon mode using Eq. 4.2.

Figure 4.15 depicts the frequency of the bulk magnetoplasmon mode at zero magnetic field for $k(j, i = 0)$, $k(j, i = 1)$, $k(j, i = 2)$ and $k(j, i = 3)$ as a function of j . These frequencies are compared with frequency at which a phase shift of π is observed in the experimental data. These

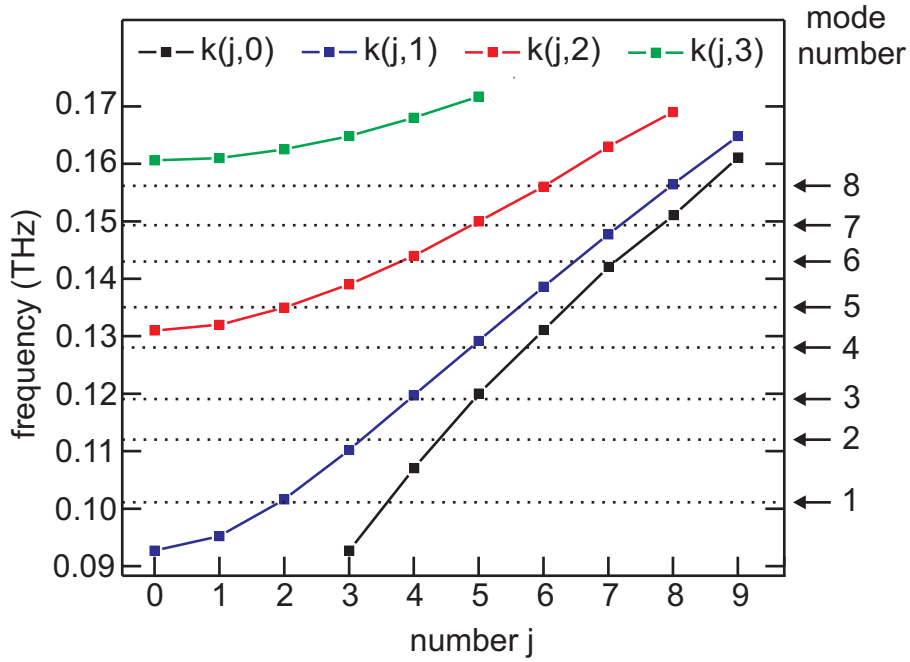


Figure 4.15: The electron plasmon frequency as a function of the j , which describes the quantization of the wave vector $k(j, i)$ in length direction of the stripe. The number i describes the wave vector quantization across the width of the stripe and assumes here the values 0, 1, 2 and 3. The plasmon frequency is evaluated for the stripe with the length $60 \mu\text{m}$ and the width $20 \mu\text{m}$. The electron density is $0.6 \cdot 10^{11} \text{ cm}^{-2}$. Horizontal dotted lines indicate the position of the fitted frequency from the table in Fig. 4.13 and the mode number is assigned to each fitted frequency.

frequencies were determined in Fig. 4.13b as best fits to the data and are marked in Fig. 4.15 with dotted lines. By correlating these frequencies with those calculated we identify the first four bulk magnetoplasmon branches as modes with the wave vectors $k(2, 1)$, $k(3, 1)$, $k(4, 1)$ and $k(5, 1)$. Above the frequency of the fourth branch the plasmon modes with $i = 2$ can be excited (red line in Fig. 4.15). Hence, the 5th branch may be assigned to the mode with wave vector $k(2, 2)$ or alternatively as $k(6, 1)$. If we assume that the driving force of the excitation, i.e. the electrical pulse, acts uniformly across the width of the 2DES stripe, then according to the dipole approximation modes with even order i cannot be excited [61, 62]. Even though the symmetry of our experimental arrangement favors the dipole approximation, we cannot entirely exclude the excitation of the modes with an even order i . The 6th branch might be attributed to a mode with wave vector $k(4, 2)$. The 7th and the 8th branches can be attributed either to wave vectors $k(5, 2)$ and $k(6, 2)$ or to wave vectors $k(7, 1)$ and $k(8, 1)$ respectively. The modes with $i = 3$ (green line in Fig. 4.15) can only be excited above 160 GHz. And therefore this mode is not relevant for the analysis of the first eight observed modes. One should point out, that the values of the bulk magnetoplasmon frequency at zero magnetic field are obtained with the fit function Eq. 4.6 that allows for the correction of the electron cyclotron frequency. Since the cyclotron frequency deviates by about 10% from its expected value (see Table in Fig. 4.13), it is not clear whether also the bulk magnetoplasmon frequency deviates at zero magnetic field.

We note that the frequency of bulk magnetoplasmons is proportional to \sqrt{n} and that the

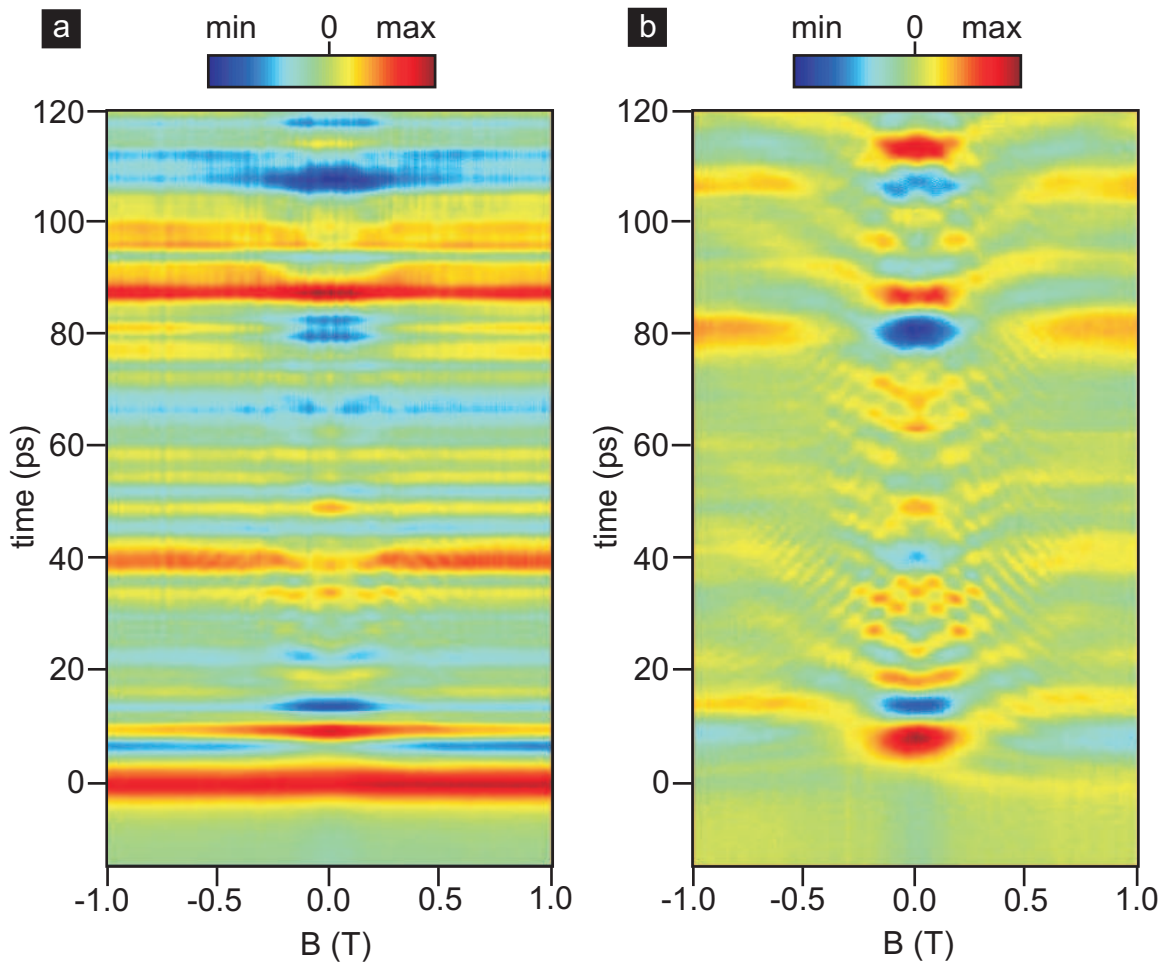


Figure 4.16: Time-dependent response of a stripe of the 2DES with a length of $60 \mu\text{m}$ and a width of $20 \mu\text{m}$. The electron density is $n = 1.0 \cdot 10^{11} \text{ cm}^{-2}$. a) Raw experimental data. A magnetic field independent signal dominates, but is superimposed on a magnetic field dependent signal. b) This magnetic field dependent signal is brought out by subtracting the magnetic field independent component along the magnetic field axis for every point on the time axis.

edge magnetoplasmon frequency scales linearly with density n . The density is therefore an interesting parameter to explore and to verify the interpretation of the data put forward here. The electron density in the stripe can be increased to $1 \cdot 10^{11} \text{ cm}^{-2}$ by illuminating the 2DES with a light emitting diode, which is positioned above the sample between the optical fibers. The raw result of time-resolved transport experiment is presented in color rendition in Fig. 4.16a. Note, that the pattern of magnetic field independent features has not changed in comparison with the data in Fig. 4.11. This confirms that these field independent features are only determined by the waveguide geometry and not the property of the 2DES. To emphasize the magnetic field dependence, magnetic field independent features are removed in the same fashion as in the previous experiment. The result is shown in Fig. 4.16b. The first peak has moved to an earlier time and appears now at 8 ps. The Fourier transform of the time domain data is depicted in Fig. 4.17. Panel a shows the color rendition of the real part and the panel b shows the color

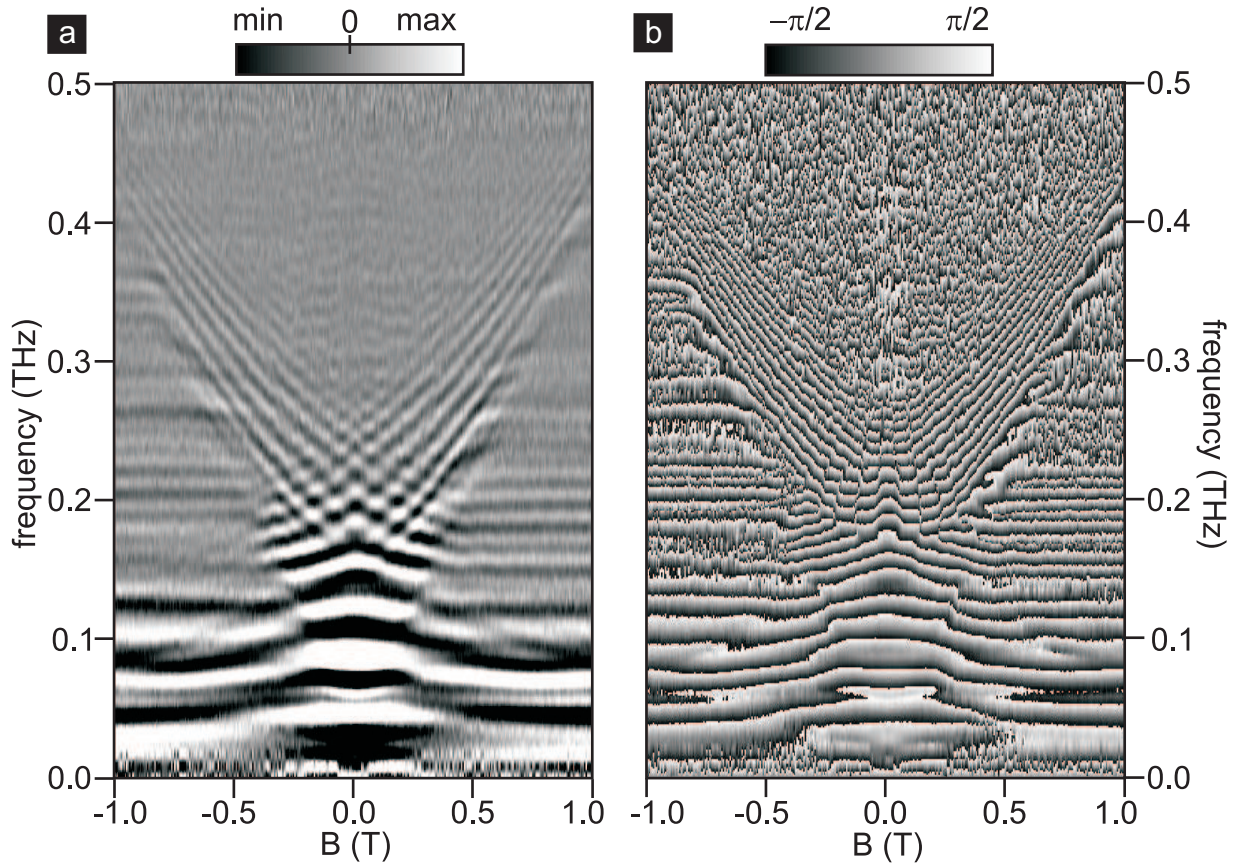


Figure 4.17: The real part and the phase of the Fourier transform of the time domain data plotted in Fig. 4.16 for the $60 \mu\text{m}$ long 2DES stripe at $n = 1.0 \cdot 10^{11} \text{ cm}^{-2}$. a) Real part of the Fourier transform. b) Phase of the Fourier transform.

rendition of the phase. Both panels show clearly that the separation between adjacent bulk magnetoplasmon modes has increased as a result of the increased electron density. The zero-field frequency of the first eight bulk magnetoplasmon modes are again identified from the fitting Eq. 4.6 to the lines corresponding to a phase shift of π in panel b of Fig. 4.17. Figure 4.18 shows the color rendition of the phase together with the best fits. Panel b lists the fit parameters. The value of the cyclotron resonance frequency deviates by about 15% from its expected value.

To assign wave vectors to each of these modes we proceed in the same fashion as before. A correlation is established between the zero-field plasmon frequency and the fit frequency f_p . Figure 4.20a plots the zero-field plasmon frequency calculated according to Eq. 4.2 as a function of j ; i serves again as a parameter and assumes the values 0, 1, 2 and 3. The horizontal dotted lines indicate the values of f_p . According to the figure, the first branch can be attributed to the excitation mode with a wave vector $k(5, 1)$ and the second branch can be attributed to the mode with a wave vector $k(6, 1)$. The mapping is carried out by successively increasing the number j by 1 for other branches. Therefore, the last branch is associated with a mode with a wave vector $k(12, 1)$. Graphically the introduced mapping is shown in Fig. 4.20b, where the fitted frequency from table in Fig. 4.18a is plotted versus the theoretically evaluated frequency. The best linear fit (orange line) shows a correspondence of almost one to one between the two frequency sets.

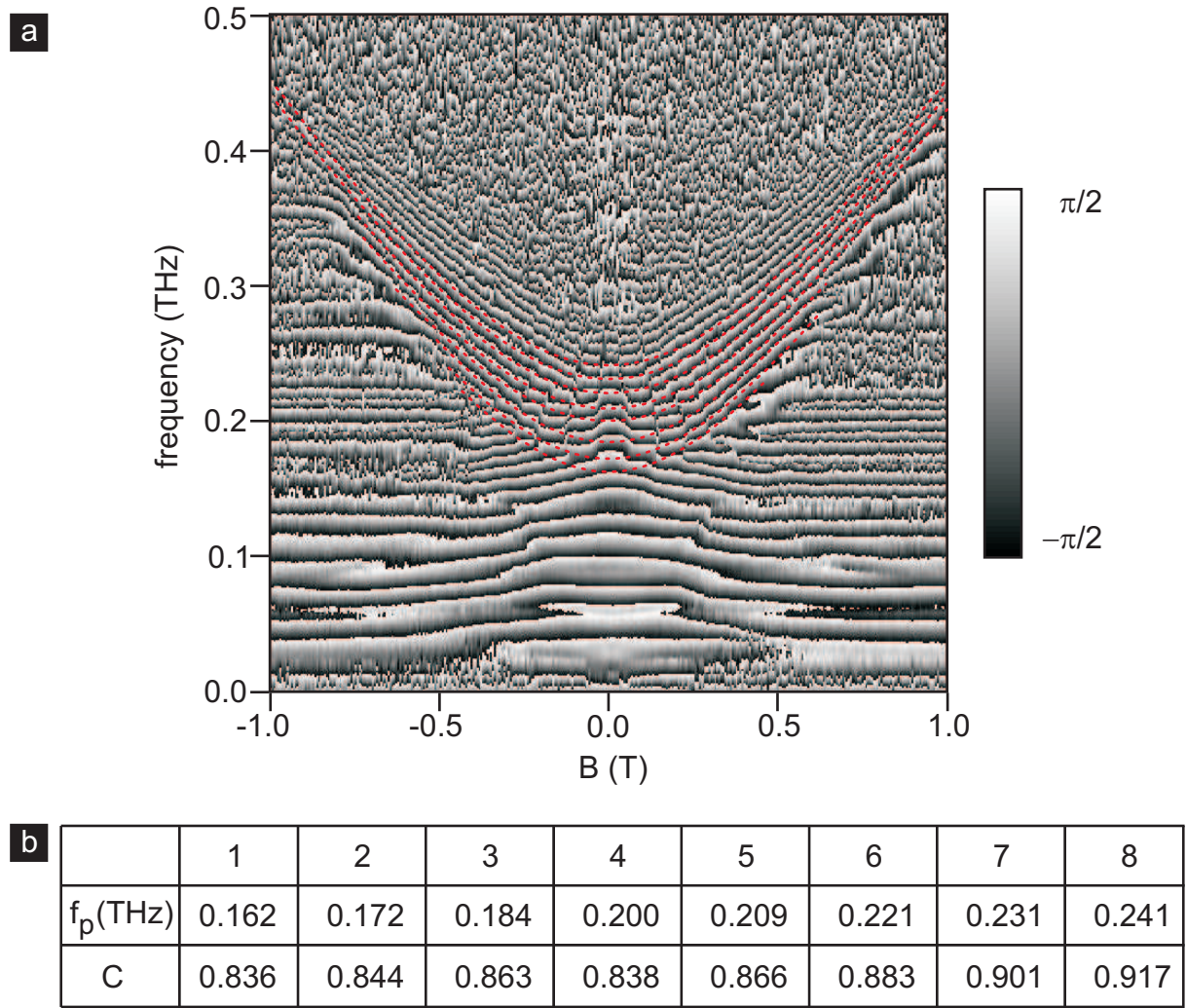


Figure 4.18: a) Phase of the Fourier transform of the time dependent data shown in Fig. 4.16. The phase change between $\pi/2$ and $-\pi/2$ is interpreted as a resonance. The red dashed lines are best fits to the data for the first eight branches of the bulk magnetoplasmons using the functional dependence described by Eq. 4.2. The parameters to obtain best fits to the data are listed in the table b. b) Table lists the best fit parameters of bulk magnetoplasmon modes. They are the plasmon frequency in zero magnetic field f_p and the correction factor C of the cyclotron resonance frequency f_c .

Figure 4.20a shows that above the frequency of the first branch the modes with $i = 2$ can be excited and that $i = 3$ modes can be relevant above the frequency of the 5th experimentally observed mode. As argued above the excitation of modes with even number i is unlikely. The excitation of modes with $i = 3$ is however not prohibited with the symmetry arguments. Even though we have assigned all eight branches to the excitations with $i = 1$, the mapping in Fig. 4.20a allows also for an assignment of the 5th branch to the excitation of a mode with a wave vector $k(1, 3)$ or $k(2, 3)$. Note, that both modes have almost the same frequency as the mode $k(9, 1)$. The strength of the excitation of $k(2, 3)$ mode will depend on the coupling of the driving force to this mode. Following the same arguments, the 6th branch can be attributed to

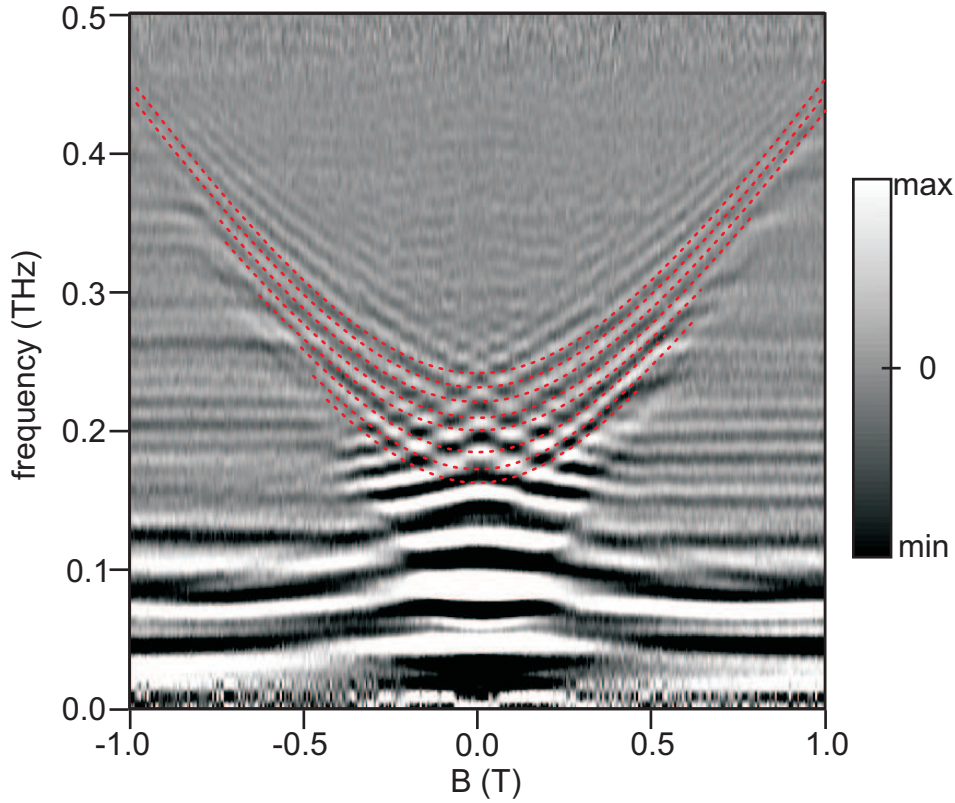


Figure 4.19: Real part of the Fourier transform. The red lines are the best fits of bulk magnetoplasmon modes from Fig. 4.18.

the excitation of a mode with a wave vector $k(5, 3)$. The assignment of other branches to an excitation with $i = 3$ is straightforward with the help of Fig. 4.20a.

4.2.3 140 μm long stripe

We discuss now the results of identical experiments performed on a stripe with a length of 140 μm instead of 60 μm at the same electron density $n = 1 \cdot 10^{11} \text{ cm}^{-2}$. Figure 4.21a shows the raw data of time-resolved experiments. The magnetic field dependent features are presented in panel b. Note, that the first pulse appears at a delay time of 18.5 ps and thus later than for the 60 μm long stripe where this feature appeared at 8 ps. To analyze the excitation spectrum we proceed in two steps. First, we analyze the edge magnetoplasmons, which are well seen when the signal of the first 60 ps in Fig. 4.21b is Fourier transformed. Thereafter, we proceed with the analysis of the bulk magnetoplasmons, which show up if we Fourier transform 100 ps of the signal.

Figure 4.22 depicts the phase and the real part of the Fourier transform of 60 ps; it shows clearly the spectral components whose frequency decreases as the magnetic field increases. According to Eqs. 4.4 and 4.5 the frequency of edge plasmons decreases in the magnetic field and thus resembles our experimental observation. The drawback of those equations is that they are derived for a semi-infinite plane and do not consider the finite size of the system. Aleiner et al. [60] described theoretically the excitation of low dimensional plasmons in a stripe and

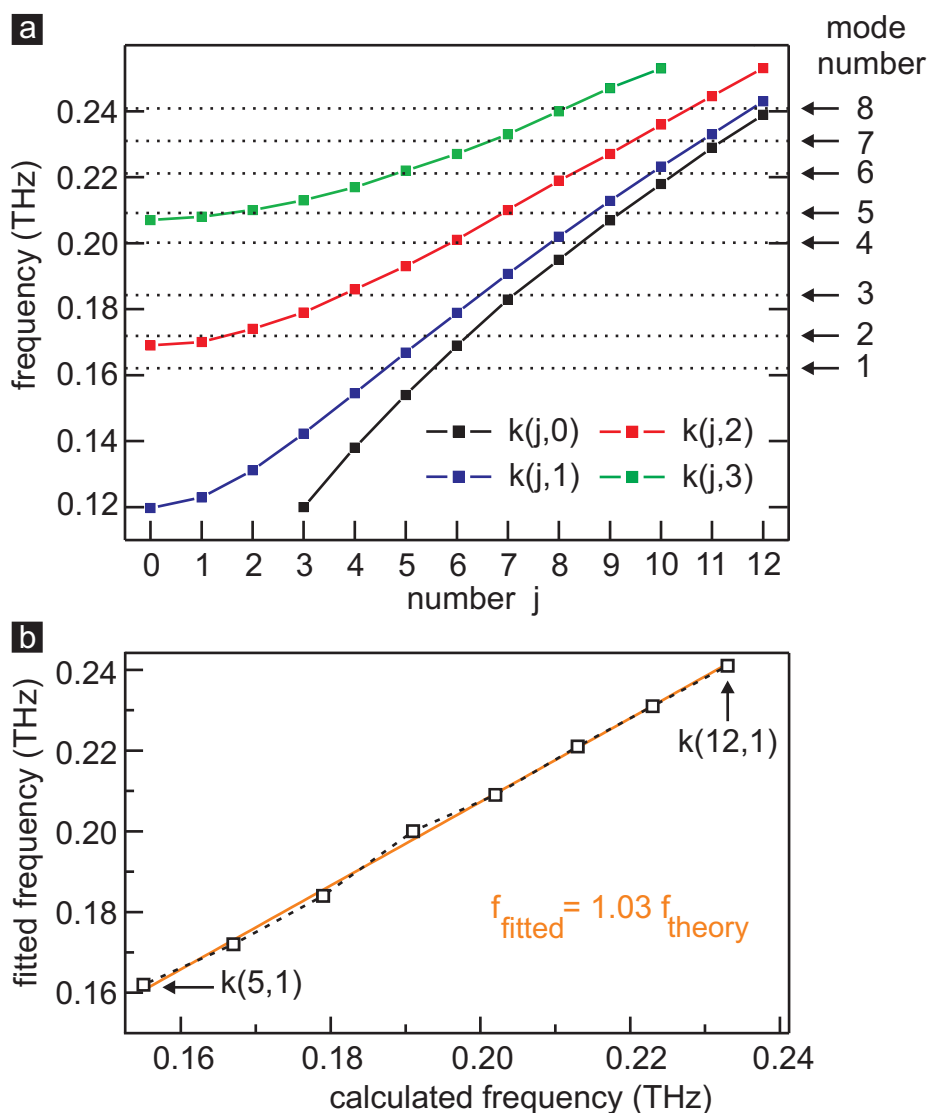


Figure 4.20: Mapping between the fitted and calculated values of plasmon frequency for a $60 \mu\text{m}$ long stripe with an electron density $1.0 \cdot 10^{11} \text{ cm}^{-2}$. a) Comparison between the theoretically calculated values of the zero-field bulk magnetoplasmon modes $k(j, i = 0)$, $k(j, i = 1)$, $k(j, i = 2)$, $k(j, i = 3)$ as a function of j and the experimentally extracted zero-field magnetoplasmon frequencies. The experimentally extracted values from a fit to the data (Fig. 4.18) are included as horizontal dotted lines. b) Correlation diagram between fitted and theoretically calculated zero-field magnetoplasmon frequencies if all observed modes are assigned to $k(j, i = 1)$ wave vectors. The best fit (red line) shows an almost 1 to 1 correspondence between two frequency sets.

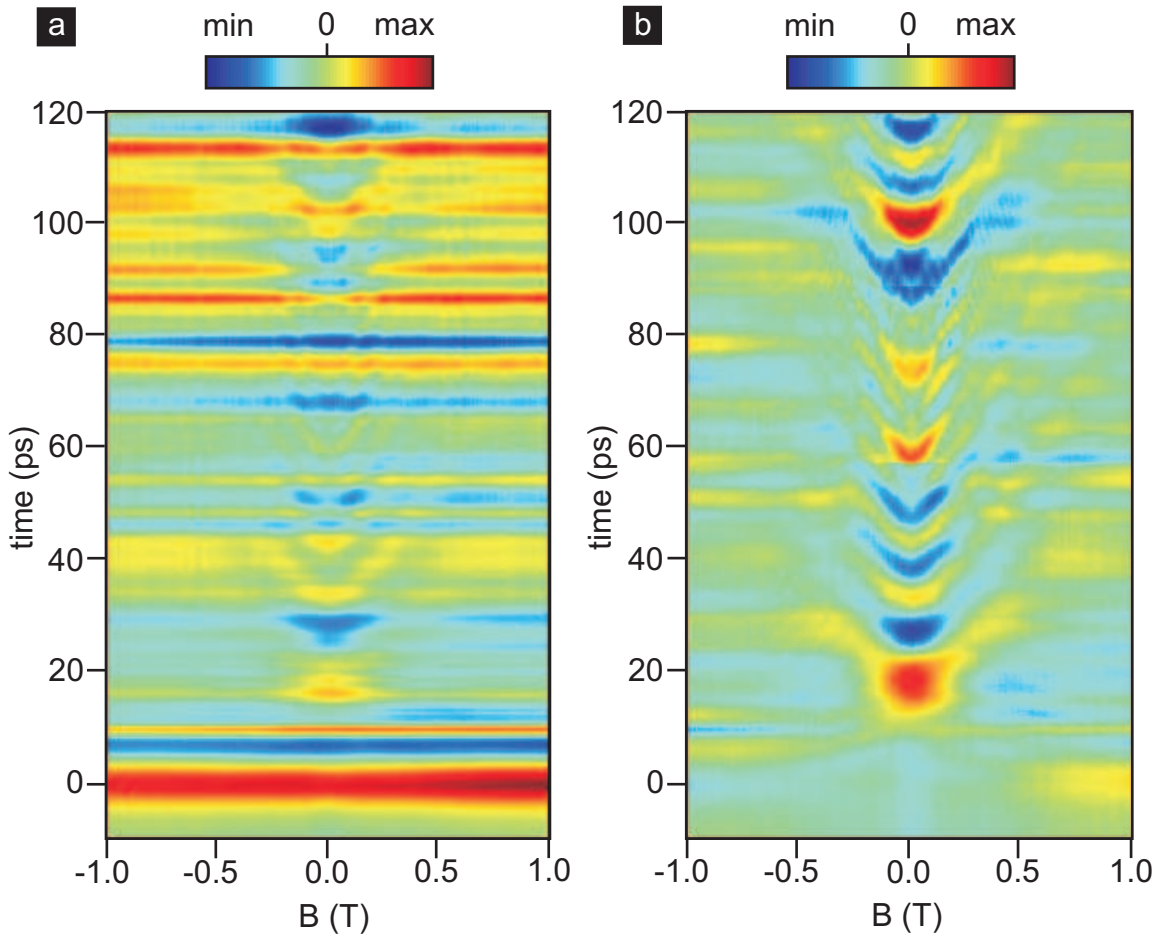


Figure 4.21: Time-dependent response of a stripe of the 2DES with a length of $140 \mu\text{m}$ and a width of $20 \mu\text{m}$. The electron density is $n = 1.0 \cdot 10^{11} \text{ cm}^{-2}$. a) raw experimental data. A magnetic field dependent signal is superimposed in a dominating magnetic field independent signal. b) A magnetic field dependent signal is brought out by removing the magnetic field independent features for each data set at a fixed time.

Kukushkin et al. confirmed it experimentally [61]. The excitation frequency is given by

$$\omega = \frac{\omega_{LO}}{\sqrt{1 + (\omega_c/\omega_{TO})^2}}, \quad (4.8)$$

where ω_{TO} is the plasmon frequency give by Eq. 4.2 with a wave vector given by the width of the stripe and

$$\omega_{LO}^2 = \frac{nwe^2}{2\pi\epsilon\epsilon_0 m^*} K^2 \left[\ln\left(\frac{8}{Kw}\right) - 0.577 \right], \quad (4.9)$$

where w is the width of the stripe and the wave vector $K = \pi/L$ is given by the stripe length L . Thus, at zero magnetic field the frequency of plasmon excitation is given by ω_{LO} and is proportion to $1/L$.

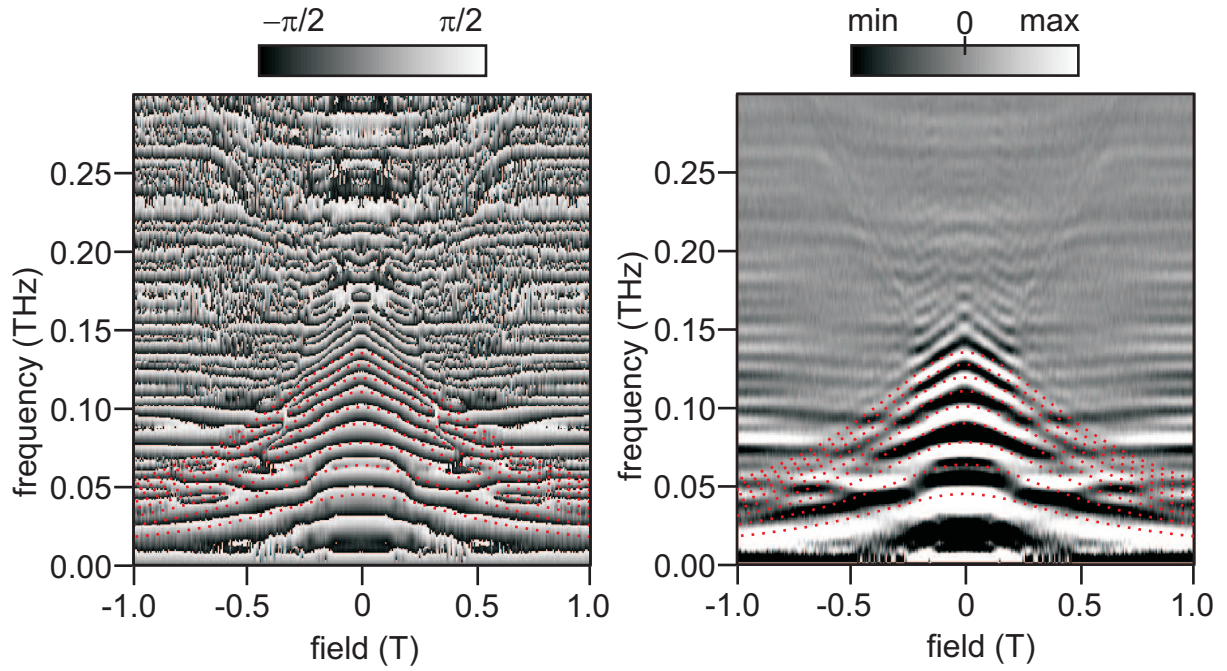


Figure 4.22: The phase and the real part of the Fourier transform of the time-domain data obtained on a 140 μm long stripe. The spectrum shows the excitation of edge magnetoplasmons. Red dashed lines show the best fit for edge magnetoplasmons. The bulk plasmons are not well seen in the spectrum.

However, we find that the spectral components in Fig. 4.22 follow the dependence

$$f = \frac{0.95 \cdot f_p(k(j, 0))}{\sqrt{1 + \left(0.98 \cdot \frac{f_c}{f_p(k(0, 2))}\right)^2}}, \quad (4.10)$$

which is plotted with dotted red lines in Fig. 4.22. The number j describes here the mode number, f_p is the plasmon frequency at zero magnetic field given by Eq. 4.2 and f_c is the electron cyclotron resonance frequency. The correcting factors 0.95 and 0.98 of the zero-field plasmon frequency can be explained with the precision with which the electron density, the dielectric constant and the effective electron mass are known. Equation 4.10 shows that the frequency at zero magnetic field becomes $0.95 f_p(k(j, 0))$ and is proportional to $\sqrt{1/L}$ (L is the length of the stripe). Note, that with Eq. 4.10 we have approximated the experimental data assuming that the drop in the edge magnetoplasmon frequency is identical for all modes and determined by $f_p(k(0, 2))$. Though Eq. 4.10 reflects the same dependence on the magnetic field as given by Eq. 4.8, it remains unclear why the frequency at zero magnetic field deviates from that in Eq. 4.8 and thus has a different dependence on the stripe length.

While the edge magnetoplasmons are well seen in Fig. 4.22, the bulk magnetoplasmons are only weakly pronounced. This indicates, that bulk magnetoplasmons are not excited yet. Remember, we Fourier transformed only the first 60 ps of the signal. However, the bulk magnetoplasmons become visible in the Fourier transform including data in Fig. 4.21b up to 100 ps. The real part of the Fourier transform is shown in Fig. 4.23 a. While the modes of the edge

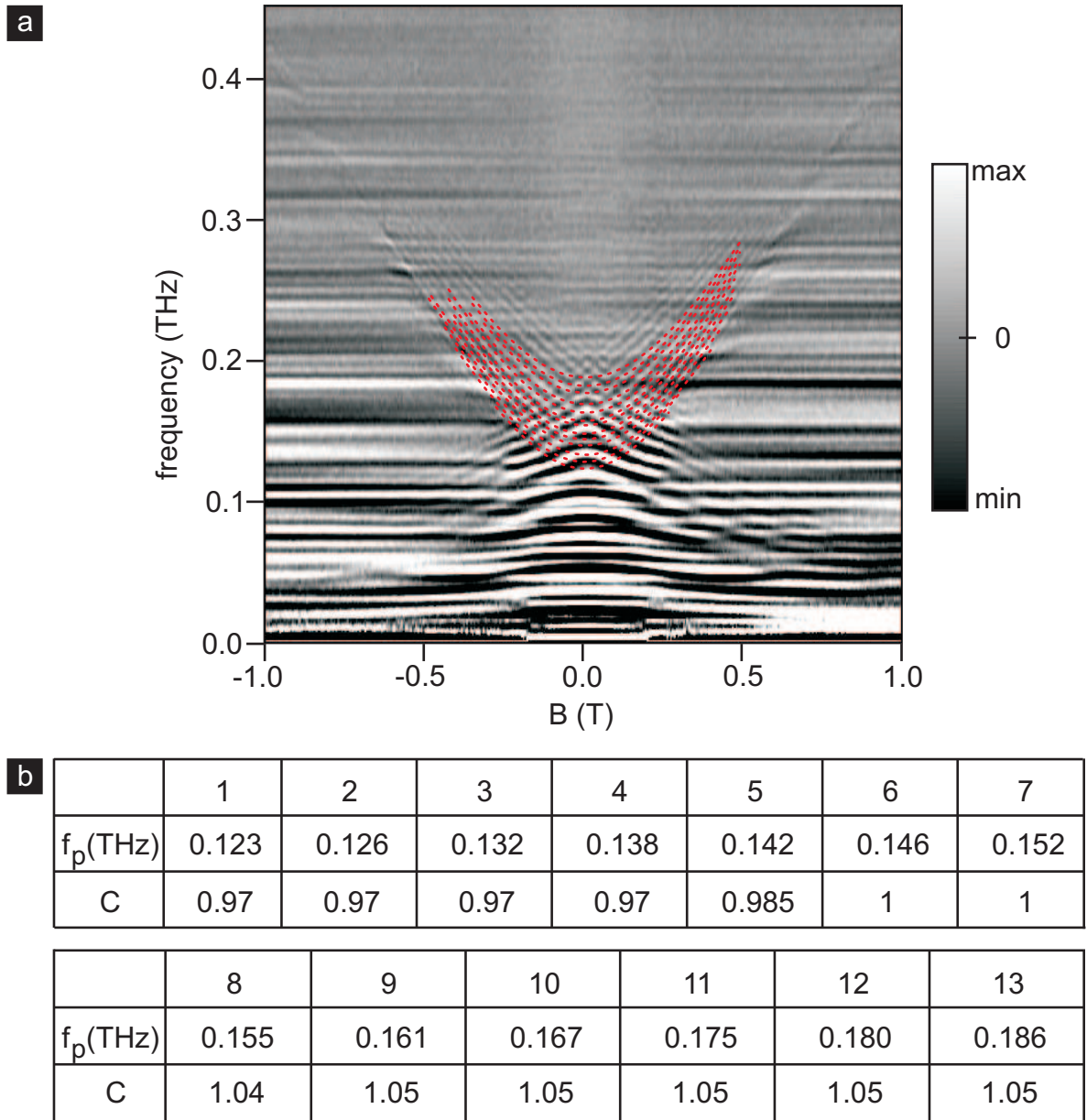


Figure 4.23: a) Real part of the Fourier transform of the time dependent data shown in Fig. 4.21. Red lines are best fits to the bulk magnetoplasmon modes. b) The table summarizes the parameters used for these fits for the first 13 bulk magnetoplasmon modes. f_p is the plasmon frequency at zero magnetic field and C is a correcting factor for the cyclotron resonance frequency.

magnetoplasmons are blurred by other spectral features at low frequencies, which most probably originate from the fact that the magnetic field independent signal in Fig. 4.21b cannot be completely removed. The modes of bulk magnetoplasmon modes are clearly visible. The modes of the bulk plasmons are positioned denser on the frequency axis than in the spectrum obtained for 60 μm long stripe for the same electron density. This affirms that the wave vector is given by the length of the stripe. We identify the first 13 modes in the excitation spectrum and fit them

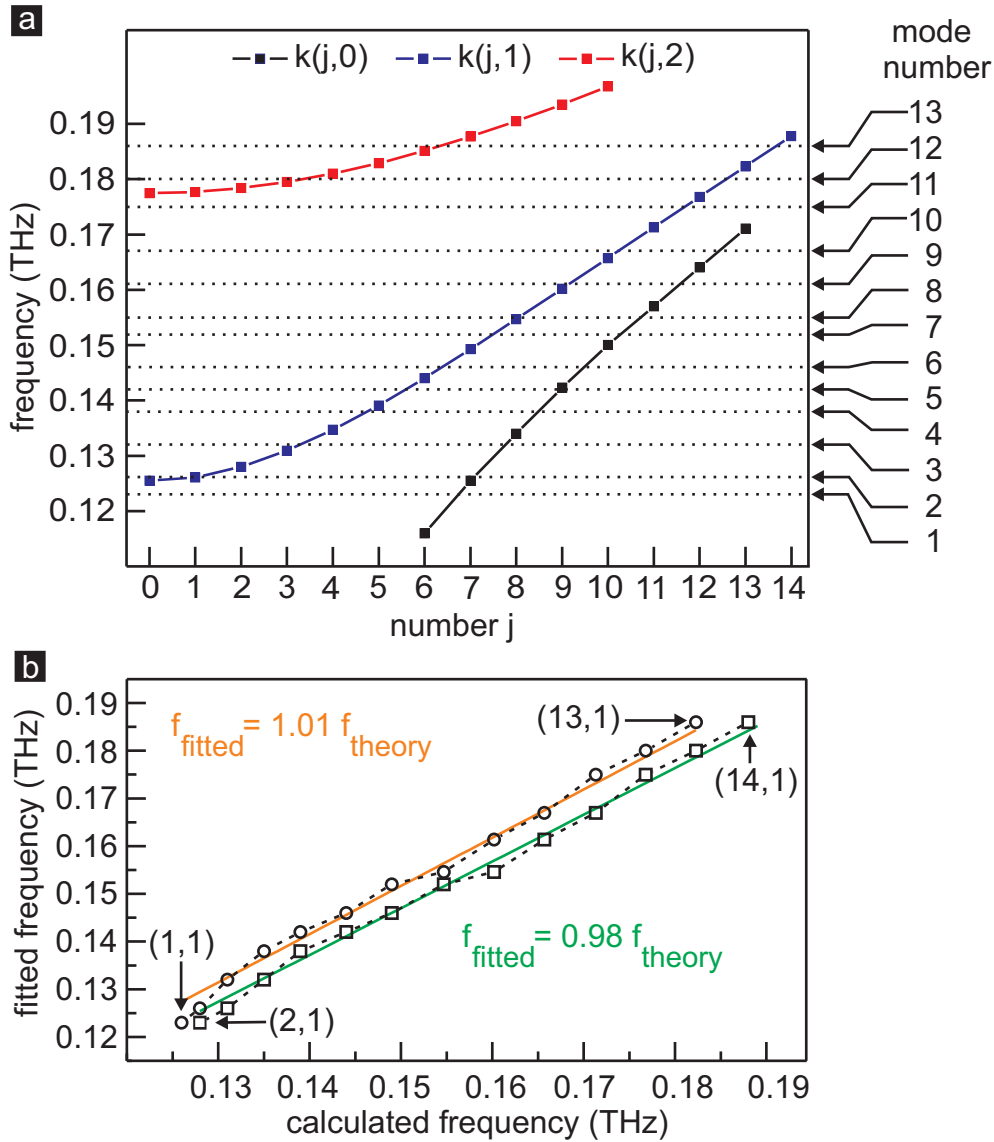


Figure 4.24: Mapping between the fitted and calculated values of plasmon frequency for a $140 \mu\text{m}$ long stripe with an electron density $1.0 \cdot 10^{11} \text{ cm}^{-2}$. a) Comparison between the theoretically calculated values of the zero-field bulk magnetoplasmon modes $k(j, i = 0)$, $k(j, i = 1)$, $k(j, i = 2)$, $k(j, i = 3)$ as a function of j and the experimentally extracted zero-field magnetoplasmon frequencies. Horizontal dotted lines indicate the position of the fitted frequency from the table in Fig. 4.23 b) Plasmon frequency from table in Fig. 4.23a vs. evaluated frequency. Two sets of mapping between the fitted and the evaluated frequencies are represented with circle and square symbols. The orange and the green lines are the best linear fits of each mapping.

using Eq. 4.6. The parameters of the best fits are listed in the table in Fig. 4.23b. The cyclotron resonance frequency deviates only by a few percent from the expected value, while a correction of up to 15% is needed for the $60 \mu\text{m}$ long stripe.

We assign now the mode numbers i and j to each excitation mode as we have done pre-

viously for the 60 μm long stripe. Figure 4.24a plots the dispersion of the zero-field magnetoplasmon frequency as a function of j for three values of i . The dotted lines indicate again the position of the zero-field magnetoplasmon extracted from the experimental data (see table in Fig. 4.23b). According to this plot modes with $i = 1$ are excited. Due to the fact that the separation between two adjacent resonances is small, an unequivocal assignment of mode numbers is difficult. Two different assignments seem possible and are graphically presented in Fig. 4.24. In the first mapping, the first magnetoplasmon mode is assigned to a mode with a wave vector $k(1, 1)$. We obtain the wave vectors for other branches by successively increasing the j in increments of 1. Hence, the last mode has $j = 13$. Circles in Fig. 4.24b represent this assignment. The best linear fit (orange line) confirms an almost 1 to 1 correspondence between the two frequency sets. In the other mapping the first mode is assigned to a mode with a wave vector $k(2, 1)$. Also here it is sufficient to successively increase the j in increments of 1 in order to obtain the wave vector for all other modes. This mapping is shown with squares in Fig. 4.24b. When plotting the experimentally extracted frequencies as a function of the theoretically calculated frequencies, here too data points fall on a line with a slope close to 1 (green line).

4.3 Pulse propagation velocity in a stripe

Since the frequency of the bulk magnetoplasmons increases with magnetic field, their phase velocity $v_{\text{phase}} = \omega_p/k$ increases with magnetic field as well. Therefore the lines that move to earlier times with increasing magnetic field in the time dependent data plotted in figures 4.11b, 4.16b, 4.21b are assigned to the bulk magnetoplasmons. In contrast, the phase velocity of the edge magnetoplasmons decreases with increasing magnetic field. Therefore the lines that move to later times with an increasing magnetic field in figures 4.11b, 4.16b, 4.21b are attributed to these edge magnetoplasmons.

Another interesting feature can be picked from the figures 4.16b and 4.21b. If the lines of the bulk magnetoplasmons are continued to their imaginary point of origin at zero magnetic field, one obtains that this point is blurred around 40 ps for 60 μm long stripe and around 90 ps for 140 μm long stripe. This fact is directly linked with the selection of the wave vector and can be comprised in the following model of bulk plasmon excitations. The spectral components of electrical pulse, which arrives at the 2DES, covers a terahertz frequency range. Each of these spectral components couples to the excitation of the 2DES with the corresponding frequency. The composition of these excitations constitutes a pulse that propagates in the stripe. We stress that the selection of the excitation modes cannot happen at the begin of the pulse formation, since the spatial boundary conditions are not given for the pulse yet. The pulse propagates then in the stripe and can probe the boundaries. The boundary conditions in the transverse direction are imposed on the pulse during its first run from the begin to the end of the stripe. And therefore, only the second quantum number of the wave vector in Eq. 4.7 can be selected. Indeed, Figure 4.22 depicts the Fourier transform of the first 60 ps and shows only weakly pronounced bulk plasmon mode with a wave vector given by the width of the stripe. When the pulse arrives at the end of the stripe, a part of it is reflected back. Thus the pulse can run back and forth in the stripe several times and probe the boundary conditions in the longitudinal direction. After at least three runs in the stripe the first quantum number of the wave vector in Eq. 4.7 can be selected as well. The continuation of the bulk magnetoplasmon lines to their

imaginary origin indicates the time point, when the wave vector is selected. Thus this time point appears earlier for the shorter stripe than for the longer one, which is consistent with the points of origin at 40 ps for 60 μm long stripe and 90 ps for 140 μm long stripe.

It is natural now to determine the propagation velocity of the pulse across the stripe. It was discussed above that the first peak in figure 4.11b, 4.16b as well as 4.21b is interpreted as the propagation of the pulse due to collective excitations in the stripe. Since both the length of the stripe as well as the time, at which the peak appears, are known, we can determine the propagation velocity. Figure 4.25a shows the time at which the peaks appears as a function of stripe length: 30 μm , 60 μm , 90 μm and 140 μm . The electron density here is $0.6 \cdot 10^{11} \text{ cm}^{-2}$. The figure shows that the signal arrives at the detector later for a longer stripe. The time of the

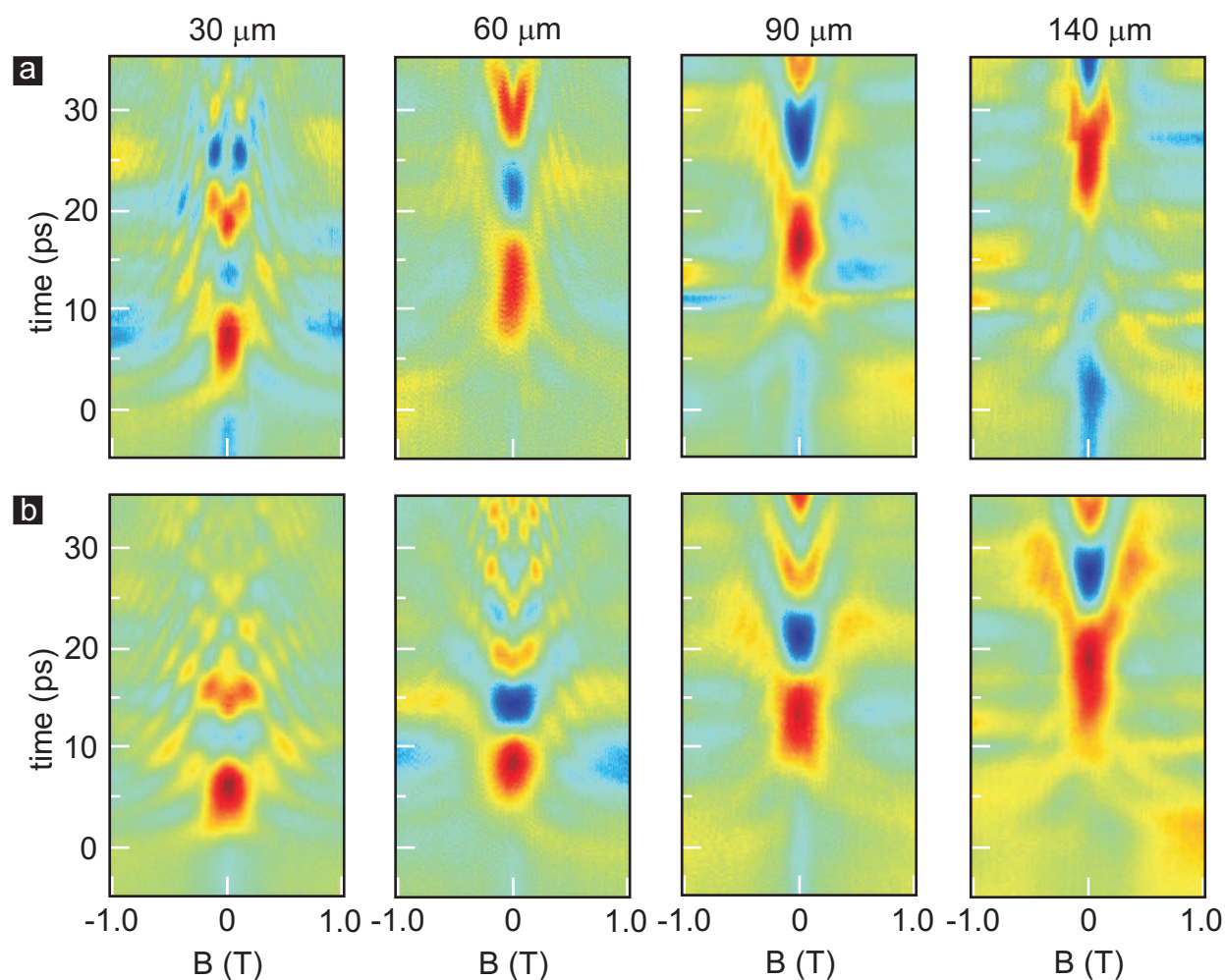


Figure 4.25: Dependence of the time resolved data on the length of the 2DES stripe. The stripe length varies from 30 μm to 140 μm . The stripe width is 20 μm . Figure captures the time-dependent response up to the first 35 ps after the excitation with an electrical pulse. a) The color rendition for an electron density $n = 0.6 \cdot 10^{11} \text{ cm}^{-2}$. b) The color rendition for an electron density $n = 1 \cdot 10^{11} \text{ cm}^{-2}$. Both panels show that the response of the stripe to the pulse excitation appears at later times for longer stripes. For a given stripe length a response appears earlier for a higher electron density.

signal maximum is plotted versus the stripe length in Fig. 4.26 with blue squares. The linear fit passing through time 0 for a stripe yields a propagation velocity of $4.9 \cdot 10^6$ m/s. The results for stripes of the same length but with a different electron density of $1.0 \cdot 10^{11} \text{ cm}^{-2}$ are summarized in Fig. 4.25b. The functional dependence on the stripe length shows the same trend; the 2DES response arrives later at the detector for a longer stripe. A comparison of data sets for the same stripe length but different density illustrates shows that the pulse arrives earlier at the detector for a stripe with a higher electron density. With red squares in Fig. 4.26 we plot the time at which the peak appears versus the stripe length. The electron density here is $1 \cdot 10^{11} \text{ cm}^{-2}$. The best linear fit passing through time 0 for a stripe length of 0 yields a propagation velocity of $7.4 \cdot 10^6$ m/s.

4.4 Temperature dependence

The last topic in this chapter illustrates how the outcome of the time-dependent transport measurement changes with temperature. It is demonstrated on a $90 \mu\text{m}$ long stripe. The experiments are performed at four temperatures 1.4 K, 10 K, 70 K, and 120 K. The temperature is measured with a cernox sensor. The experiment at each temperature is done after the system has thermalized at the given temperature for several hours. Figure 4.27 summarizes the experimental results. The upper row shows the raw data of the time-resolved transport experiment, while the

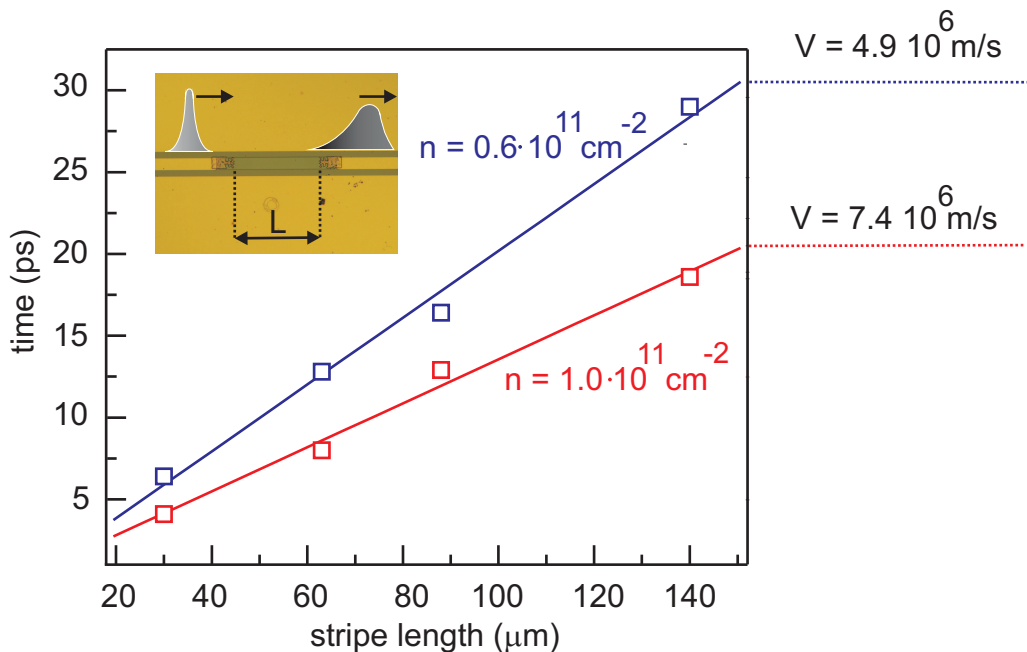


Figure 4.26: The time when the first peak around $B = 0$ appears as a function of the stripe length. These data points are extracted from Fig. 4.25. The blue and red squares are for an electron density of $0.6 \cdot 10^{11} \text{ cm}^{-2}$ and $1.0 \cdot 10^{11} \text{ cm}^{-2}$ respectively. The red and blue lines are best linear fits to each data set. We enforce an interception at time 0 for a stripe of length 0. The propagation velocity is given in the plot for each electron density.

lower part of the figure depicts the experimental results after their filtering. Note, that the magnetic field independent features do not change with temperature. We therefore attribute them purely to the waveguide structure. This is the main conclusion of this section.

Since we have developed an intuitive understanding of some magnetic field dependent features, we can read from the bottom panel of Fig. 4.27 that the bulk magnetoplasmons are present at temperatures of 1.4 K and 10 K, but are absent at higher temperatures. Only the features from the edge magnetoplasmons remain visible at 70 K, even though they are strongly damped. At even higher temperatures (120 K) all plasma excitations have vanished. For completeness, we mention here that the electron density changes with the temperature, which leads to a slight shift of the first peak along the time axis. The electron density was determined from the slope of the two-terminal transport resistance in a magnetic field: for $n = 1.2 \cdot 10^{11} \text{ cm}^{-2}$ at 10K, $n = 1.6 \cdot 10^{11} \text{ cm}^{-2}$ at 70K and $n = 1.9 \cdot 10^{11} \text{ cm}^{-2}$ at 120K.

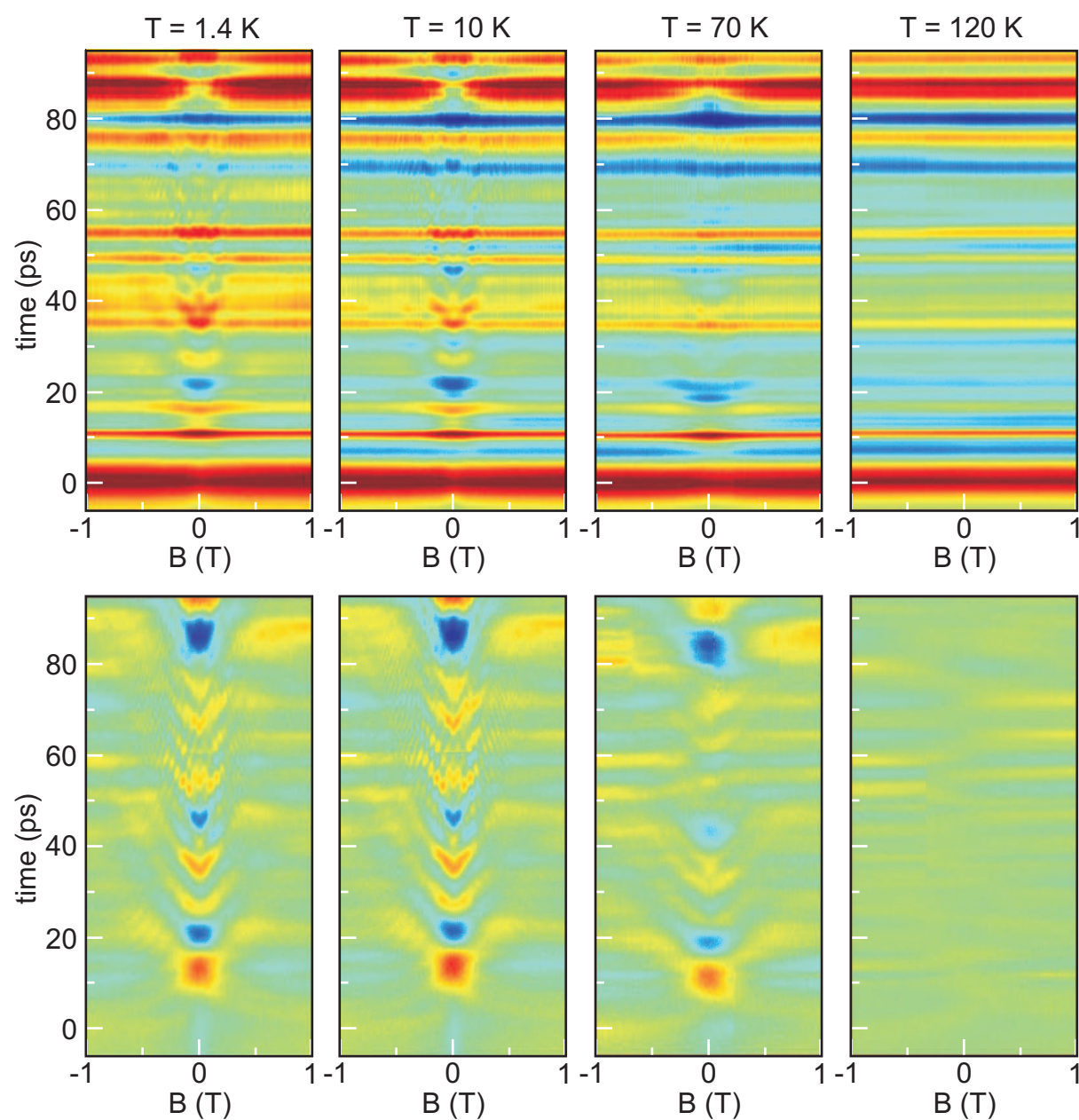


Figure 4.27: Temperature dependence of the time resolved data in a stripe of $90 \mu\text{m}$ length. The measurements are done at 1.4 K, 10 K, 70 K and 120 K. The upper panels summarize raw data, while the bottom panels depict data after removing magnetic field independent features. The plasmon modes vanish gradually as the temperature increases. The bulk magnetoplasmons have disappeared at 70 K, while the signature of the edge magnetoplasmons survives up to 120 K.

Chapter 5

Correlation of electrical pulses on a 2DES

This chapter introduces an alternative measurement concept to the photoconductive sampling technique. The suggested measurement method adopts the idea of photocurrent autocorrelation, which is used to characterize the electron lifetime in photoconductive switches [11, 12, 14, 19, 20], and can be utilized for time-resolved transport measurements in low-dimensional systems. It is therefore referred as electrical pulse correlation. The experiment introduced in this chapter is the first attempt to implement the new measurement approach. The experimental results are preliminary and therefore raise a number of questions. Nonetheless we can devise an experiment, that facilitates the measurement of time-resolved electron transport in mesoscopic device.

5.1 Idea behind the electrical pulse correlation technique

In order to explain the idea of the electrical pulse correlation in a 2DES, it is instructive to outline first the idea of the photocurrent autocorrelation method in photoconductive switches. This method utilizes the fact that the photocurrent I , which is created in the photoconductive switch, is commonly non-linearly proportional to the irradiated optical power P , i.e. $I \sim P^\alpha$, where $\alpha < 1$ is the power that describes the non-linearity. It is assumed that the laser spot size on the switch is fixed. Figure 5.1 a shows the photoconductive switch, which is integrated into the CPW geometry, and the experimental arrangement to measure the photocurrent. The photoconductive switch is irradiated by two short optical pulses, which are delayed in time relative to each other [11], and the total average photocurrent is measured as a function of the delay time between the optical pulses. Figure 5.1 b displays the photocurrent as a function of the delay time $\Delta\tau$ between the pulses. The reduction of the photocurrent at zero delay time is due to the sub-linear response and can be understood as follows. At a delay time, which is larger than charge carrier lifetime in the switch, the total photocurrent is the sum of photocurrents created by each optical pulse separately, i.e. $P^\alpha + P^\alpha$, since the measured current is integrated over several laser cycles. However, at zero delay time the total photocurrent amounts to $(P + P)^\alpha$ and is less than the sum of the currents created by every pulse individually.

In this autocorrelation arrangement the switch is excited by two optical pulses, each of which, in its turn, creates a transient current pulse. The delay time between the electrical pulses is therefore given by the delay time between the optical pulses. In the following experiment,

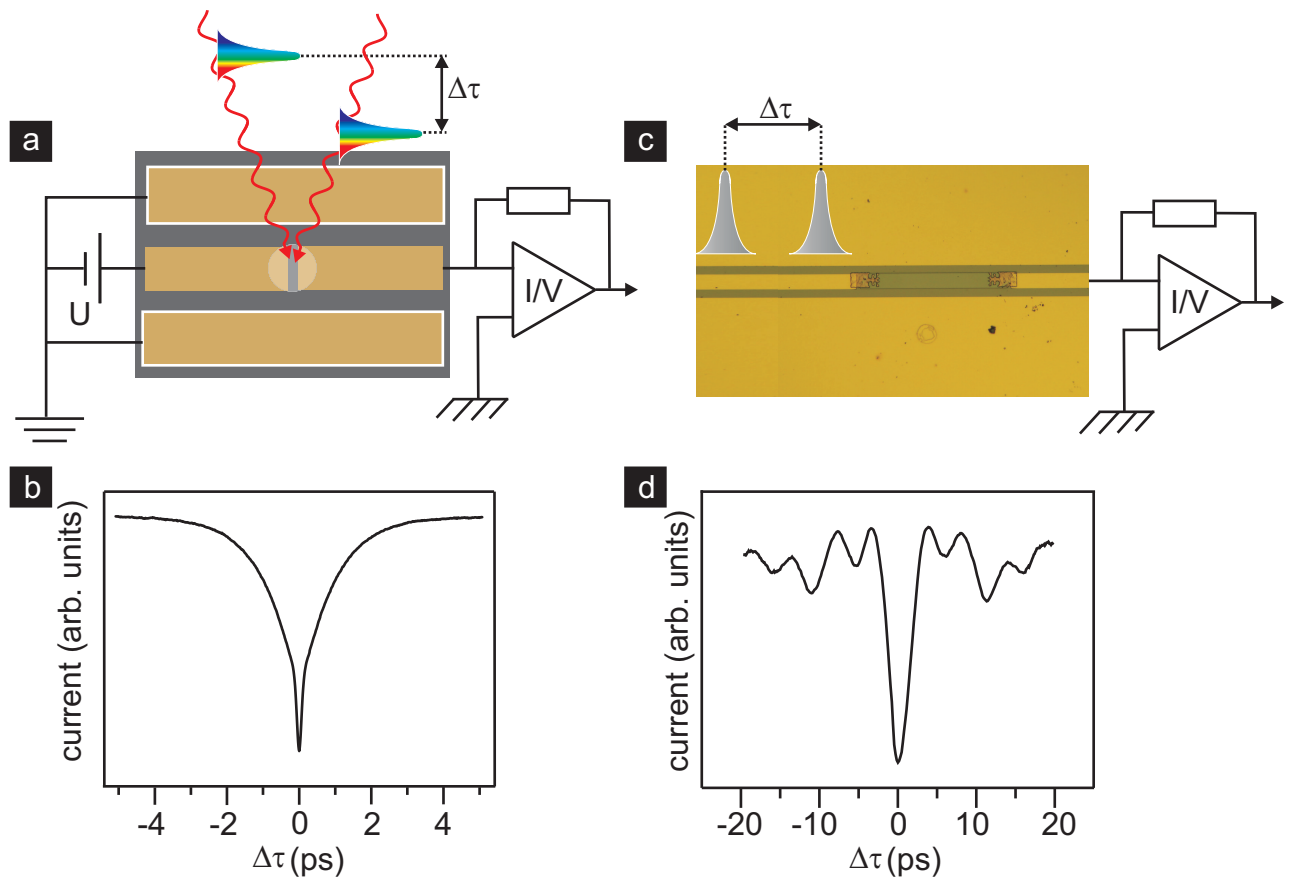


Figure 5.1: Analogy between the photocurrent autocorrelation on a photoconductive switch and the electrical pulse correlation on a 2DES. a) A setup for photocurrent autocorrelation measurement on a photoconductive switch, which is integrated into a CPW. The photoconductive switch is operated by two short optical pulses, which induce time-dependent photocurrents in it. The average photocurrent in the switch is measured as a function of the delay time between two optical pulses. b) Autocorrelation curve measured on the switch. The total average current, which flows in the switch, is plotted as a function of the delay time between two optical pulses. c) A setup for electrical pulse correlation measurement on a 2DES. The stripe of a 2DES is excited by two electrical pulses and the average current is measured as a function of the delay time between the two electrical pulses. The delay time between the electrical pulses is given by the delay time between the optical pulses which operate the switch. d) Correlation curve measured on the 2DES. The average current is measured as a function of delay time between the two electrical pulses excited with the photoconductive switch.

those electrical pulses excite the 2DES and the current is measured as a function of delay time between the pulses. Note, in order to consider two electrical pulses to be well separated in time, the time interval between them should be larger than the electron lifetime in the photoconductive material. The electron life time in the photoconductive material used in the current experiment is on the order of 1 ps. Figure 5.1 c shows the schematic of the experimental arrangement for the electrical pulse correlation measurement on a 2DES. It indicates that two electrical pulses

are created on the left side from the 2DES. The experiment is performed on a 2DES stripe with a length of $140 \mu\text{m}$ and a width of $20 \mu\text{m}$. The electron density at 1.4 K equals to $0.6 \cdot 10^{11} \text{ cm}^{-2}$. Figure 5.1 d shows the outcome of the experiment in zero magnetic field. The reduction of the current at zero delay time reflects the measurement of the photocurrent autocorrelation curve on the photoconductive switch, which is used in the experiment (compare with Fig. 5.1 b). At non-zero delay the curve exhibits oscillations which are absent in the photocurrent autocorrelation curve. Hence, we conclude that those oscillations originate from the 2DES, since its presence in the experiment is the only difference between the experimental setups in panel a and c.

In the following, it will be shown that these current oscillations are strongly affected by an externally applied magnetic field. Since the behavior of the photoconductive switch is magnetic field independent in the field range under consideration, the signal variations can be attributed solely to the 2DES.

5.2 Correlation in magnetic field

The bottom panel of Fig. 5.2 depicts a color rendition of the average correlation current as a function of both the magnetic field and the delay time $\Delta\tau$. The observed dependence of the signal on the magnetic field is surprising and confirms that the 2DES is responsible for this signal. The starting point for understanding the experimental result may be as follows. In

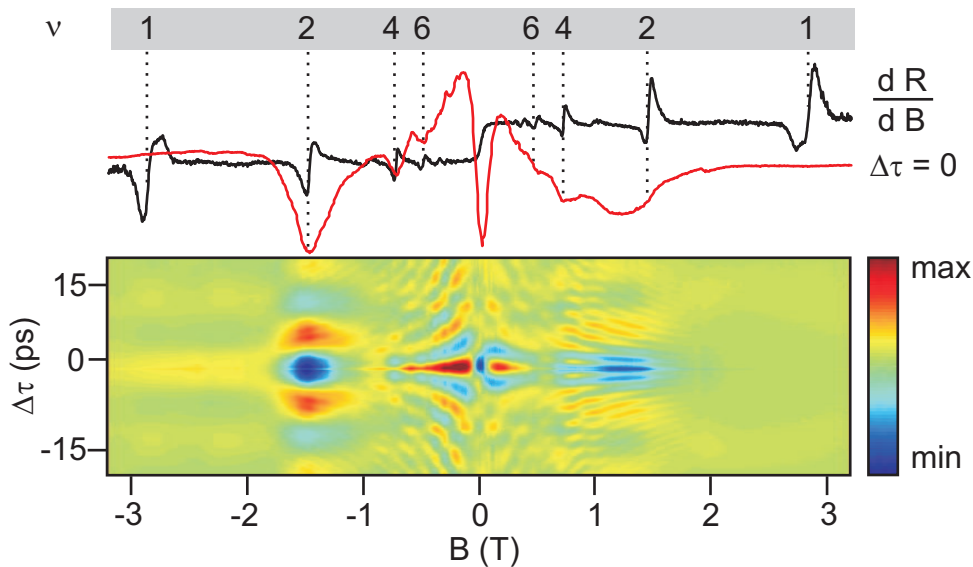


Figure 5.2: Electrical pulse correlation measurement in the magnetic field. The bottom panel shows a color rendition of the average current as a function of both the magnetic field and the time delay $\Delta\tau$. The red line in the top panel represents a trace extracted from the color plot at zero time delay $\Delta\tau$ along the magnetic field axis. The black line depicts the derivative of the two-point resistance with respect to the magnetic field. The dotted lines mark the integer filling factors. Some features are correlated between the two curves. For negative magnetic fields, the correlation curve exhibits a dip, whenever 2DES condenses in an even integer filling factor quantum Hall state.

the previous chapter it has been shown that an electrical pulse excites plasmons in the 2DES stripe. Prior to the pulse excitation the 2DES is in an equilibrium state. After the first electrical excitation, the dynamics of plasmon excitations is observed on the time scale of 100 ps (see Chapter 3). Hence, when the second electrical pulse, which is delayed in time, arrives at the 2DES, the system is in a non-equilibrium state. The second electrical pulse excites additionally the 2DES stripe. In other words, the second electrical pulse probes the state of the 2DES after its excitation by the first pulse. It is not clear yet, how the second excitation of the system leads to a measurable signal. From the analogy between the photocurrent autocorrelation in the switch and the electrical pulse correlation on a 2DES, we conclude that non-linear effects should play an important role for the observation of the signal. Hence, this non-linearity originates from the 2DES. If so, then this non-linearity must be linked to the plasmon excitations in the 2DES. But is it essential to have a non-linearity for signal observation? The open questions must be addressed in further experiments and in theoretical models, which support the experiments.

Here, we highlight several important features in the measurement plotted in Fig. 5.2:

- Magnetic field independent signal is absent. This is contrary to the experimental results presented in the previous chapter. The recorded data do not require a pre-filtering, which was necessary for the experimental results presented in the previous chapter in order to remove magnetic field independent signal. This measurement method apparently offers the advantage of being sensitive only to the properties of the 2DES for $|\Delta\tau| > \tau_{lifetime}$.
- Signal asymmetry with respect to the direction of the magnetic field. This behavior is unclear yet. An asymmetry with respect to the direction of the magnetic field may indicate that the edges of the stripe are not identical. The asymmetry could also be related to the misalignment of the ohmic contacts on the stripe. However, further experiments are needed to clarify the origin of the asymmetry.
- Signal variation at zero delay time. It was suggested above that the signal around zero delay time reflects the autocorrelation measurement on the switch. It was also stated that the magnetic field does not affect the operation of the switch. However, the signal at zero delay time varies with the magnetic field. Hence, we have to revise the above statement: the measured signal is a convolution of the switch autocorrelation signal and the non-linear 2DES response.
- The dependence of the signal on the Landau level filling factor [63]. The red line in the top panel of the Fig. 5.2 depicts a trace from the color plot at zero delay time along the field axis. Integer filling factors are marked. The black line shows the derivative of the two-point resistance with respect to the magnetic field. These two traces exhibit a strong correlation with each other; the photocurrent curve (red line) exhibits a dip, whenever the 2DES condenses in an integer quantum Hall state. This correlation is well pronounced for the integer filling factors 2, 4 and 6 for negative values of the magnetic field. Even though it is less clear for positive values of the magnetic field, it is also there.

The electrical pulse correlation signal persists also at later times. Figure 5.3 a depicts the correlation signal up to 100 ps. Filling factors $\nu = 1$ and $\nu = 2$ have been marked for negative magnetic field. The asymmetry with respect to the direction of magnetic field is apparent here.

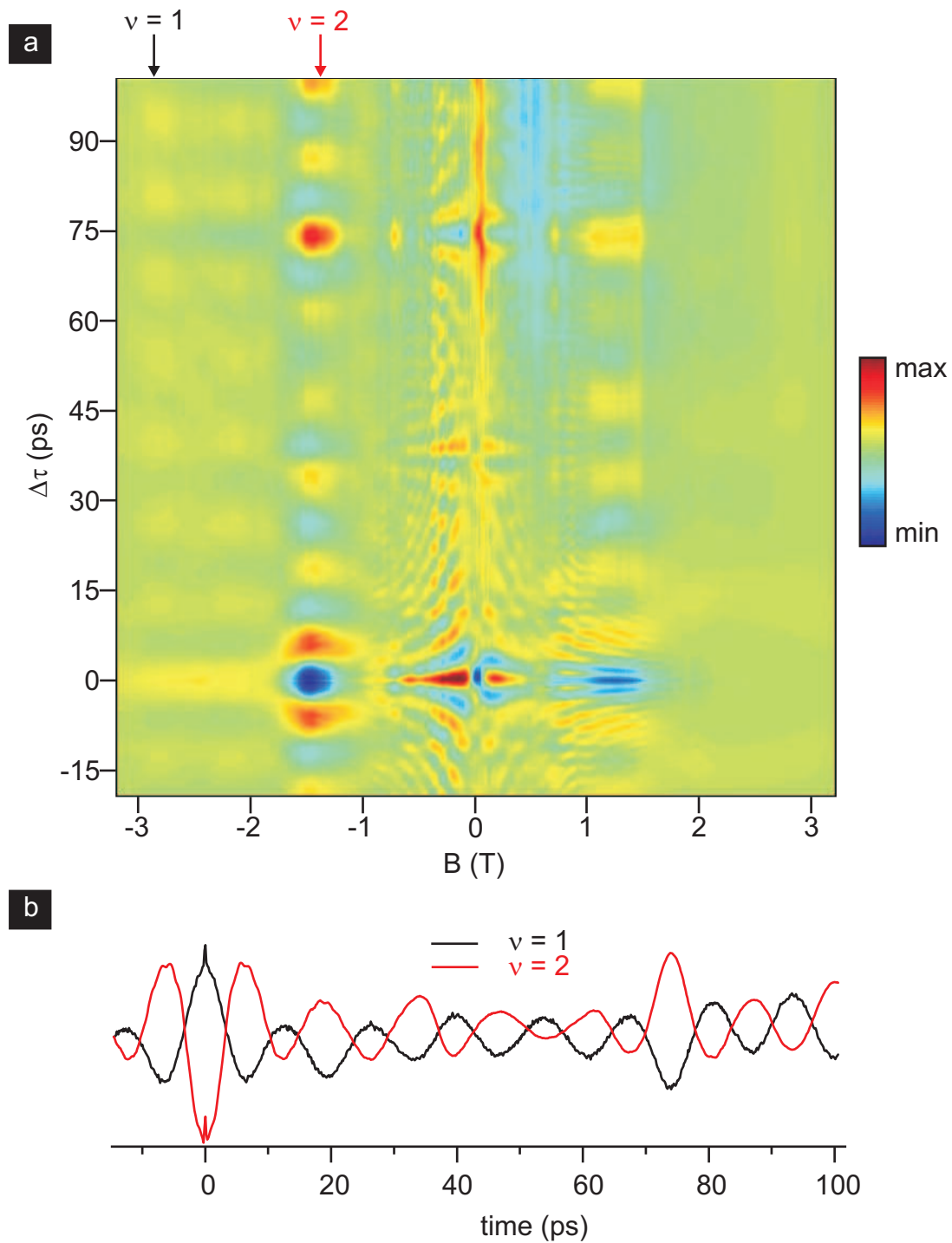


Figure 5.3: a) Color rendition of electrical pulse correlation measurement in the magnetic field. The stripe length is $140 \mu\text{m}$ and the electron density equals $0.6 \cdot 10^{11} \text{ cm}^{-2}$. The filling factors $\nu = 1$ and $\nu = 2$ are indicated. b) Traces from color plot along the time axis for the filling factors $\nu = 1$ and $\nu = 2$. The amplitude of traces is adjusted so, that both traces appear with the same amplitude.

Another interesting fact is brought out when the traces along the time axis at these filling factors are plotted together. Figure 5.3 b shows these traces, whose amplitude is scaled so that both traces appear with the same amplitude at zero delay time. This representation makes clear that the traces have the same periodicity, but are phase shifted: a local minimum of one trace corresponds to a local maximum of the other trace. The phase change happens at a field around -2 T as seen in Fig. 5.3 a.

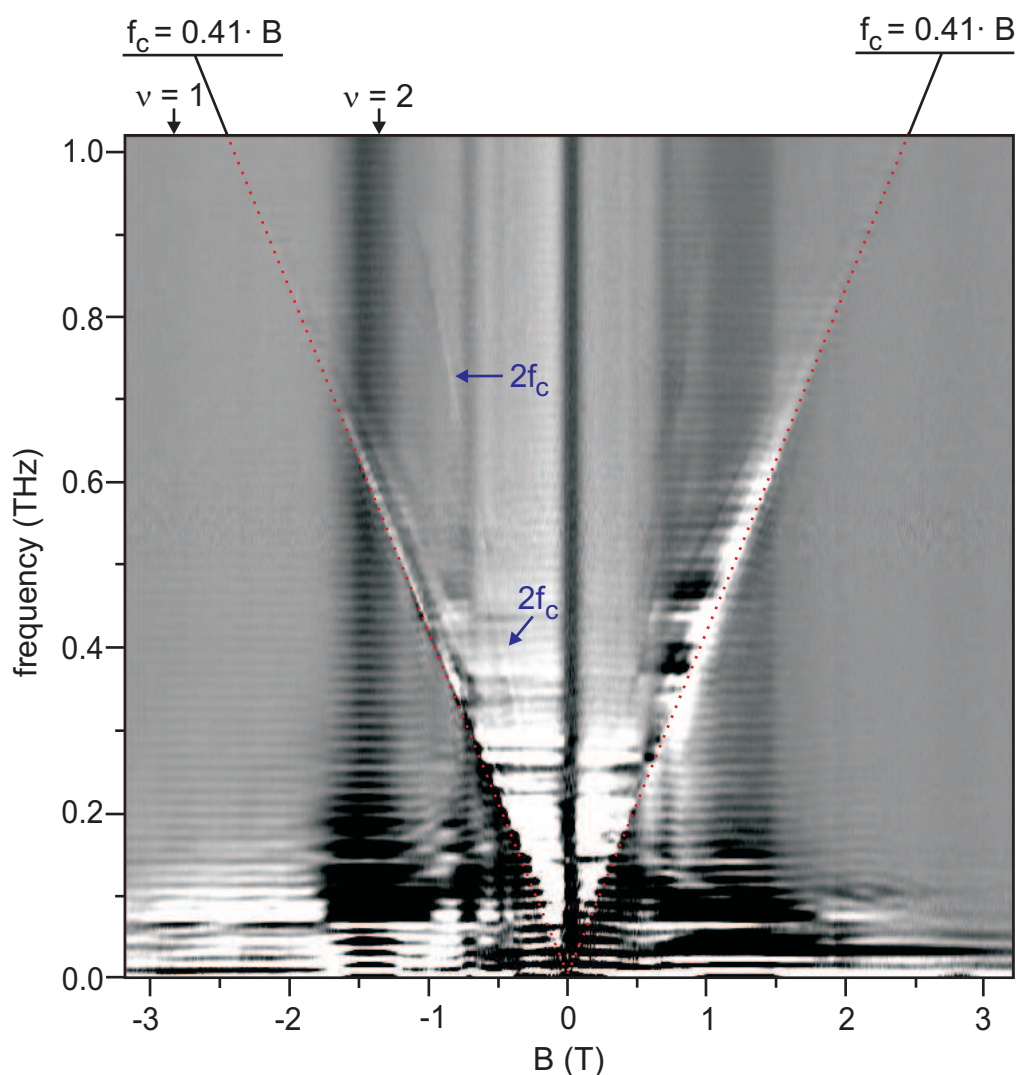


Figure 5.4: Real part of Fourier transformation of correlation signal shown in Fig. 5.3. The red dashed lines indicate the cyclotron resonance line of electrons. In GaAs the electron cyclotron resonance frequency f_c in a magnetic field B is $f_c = 0.41B$ (THz/T). The arrows point to the position of the features at the double cyclotron resonance frequency $2f_c$.

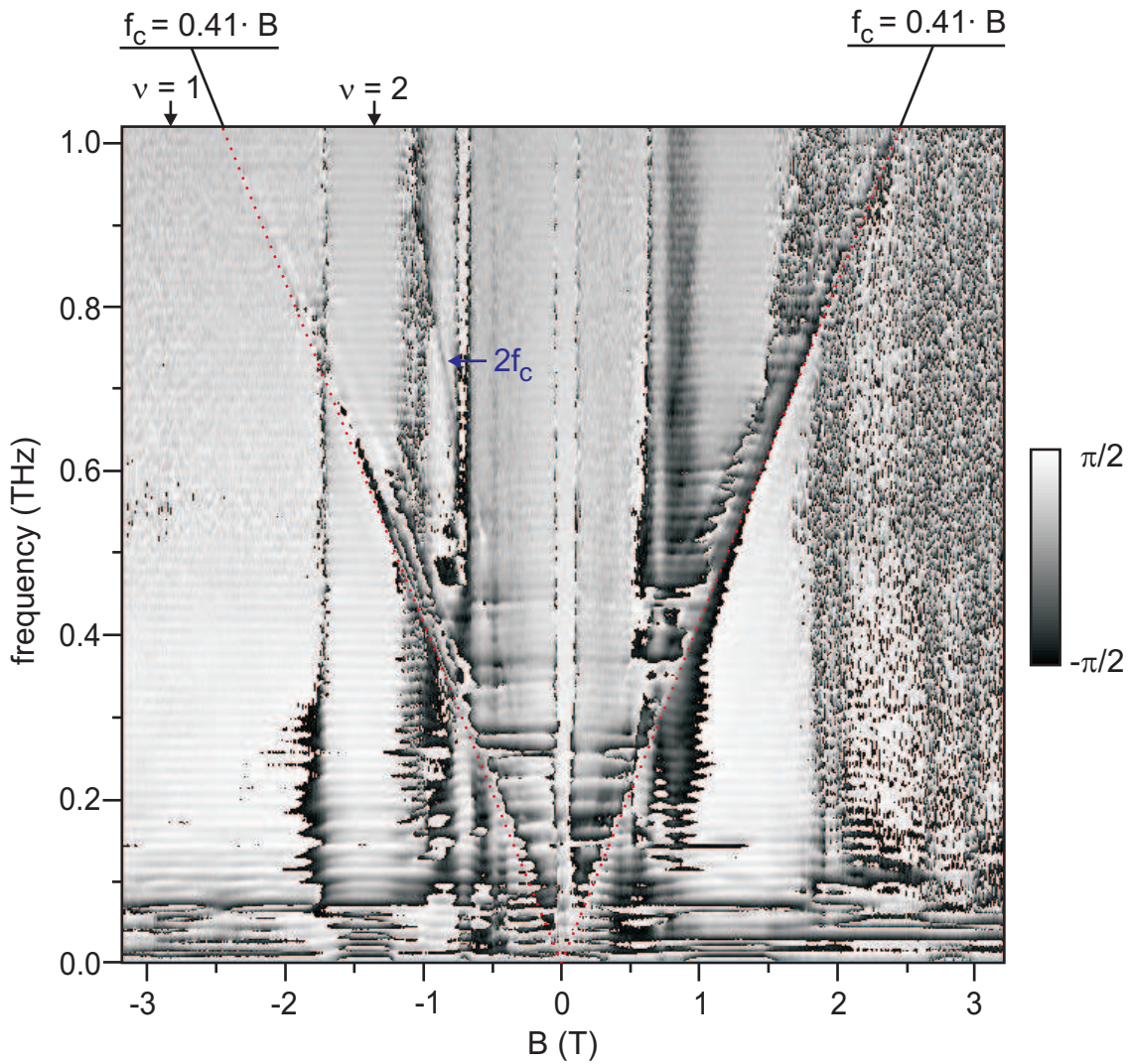


Figure 5.5: Phase of Fourier transformation of correlation signal shown in Fig. 5.3. The red dashed lines indicate the cyclotron resonance line of electrons. The arrow points to the position of the features at the double cyclotron resonance frequency $2f_c$.

5.3 Excitation spectrum

The time domain data presented in the previous section raised a number of questions. Fourier transform of the data can likely help to answer some of them or may give a hint. Each time dependent trace at fixed B plotted in Fig. 5.3 a is transformed. Figure 5.4 and Figure 5.5 depict the real part and the phase of the Fourier transformation respectively. The spectrum does not contain various modes of plasmon excitation, which were reported in the previous chapter. Both plots show, however, a spectral component whose frequency increases in the magnetic field and follows well the electron cyclotron frequency f_c in high magnetic field (red dashed red line in Fig. 5.4). As shown in the previous chapter, the resonance frequency of bulk magnetoplasmons approaches the electron cyclotron resonance frequency in the limit of high magnetic field, but it is finite at zero magnetic field. Unfortunately, the spectrum is blurred in the vicinity of

zero magnetic field and in the low frequency region, where one would expect the plasmon resonance. Hence, it is difficult to tell with certainty, whether this line represents the electron cyclotron resonance or an excitation of a single magnetoplasmon mode. This complicates the identification of the spectral line and thus leaves room for speculation. Moreover, Figure 5.4 exhibits an intriguing feature. It shows a spectral line at double the frequency of the electron cyclotron resonance mode. This fact suggests a generation of the second harmonic, which is a strong evidence for non-linear processes, which take place in the 2DES. The spectral line at the doubled frequency are observed, however, only at the negative magnetic field. Another noticeable feature is that the spectrum in Fig. 5.4 and Fig. 5.5 covers a frequency range of up to 1 THz. Remember, in the previous chapter the spectral range extends only up to 0.45 THz. It is not clear yet why the spectrum, which is obtained from the correlation measurement, covers a larger spectral range.

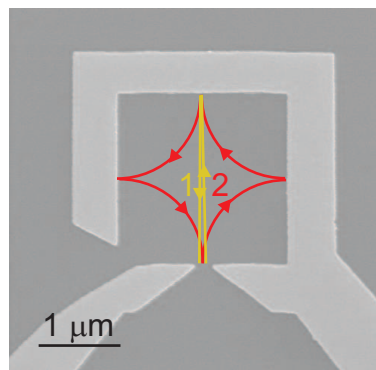


Figure 5.6: Square cavity is a suitable geometry to conduct a time-resolved transport experiment with the measurement technique introduced in this chapter.

The main conclusion of the experiment is that the 2DES most likely exhibits a non-linear behavior, which leads to the signal shown in Fig. 5.2. The origin of the non-linearity is unclear yet and should be addressed in further experiments. This type of the experiment may also be very useful to measure the electron's Fermi velocity in mesoscopic devices. The idea of the measurement is elucidated on the example of a square cavity, which is shown in Fig. 5.6 and was characterized in the DC-transport in Chapter 2. The first electrical pulse injects the electrons through a quantum point contact (QPC) into the cavity. In zero magnetic field the electrons reflect from the opposite wall and return back to the QPC (trajectory 1). The second electrical pulse also injects the electrons into the cavity. When the delay time between two pulses is so that the electrons of the second pulse are being injected into the cavity at the time as the electrons of the first pulse return to the QPC, we expect to observe a dip in the correlation signal. The same consideration holds for the magnetic field, at which electrons reflect on each wall once and then reach eventually the QPC (represented by trajectory 2). The length of electron trajectories for these two different magnetic fields is different, as it was discussed in Chapter 2. Therefore, the dip in the correlation curve will appear at different times at both magnetic fields. And this fulfills the requirement for conducting the time differential measurement as outlined in Chapter 2.

Chapter 6

Summary and Outlook

The work presented brings forward the ambitious objective to perform picosecond time-resolved transport experiments in nanostructures or mesoscopic devices with Composite Fermions. These quasi particles come into play in the regime of the Fractional Quantum Hall Effect, which requires both high magnetic fields and an ultra-cold environment for GaAs-based heterostructures. One level of complexity lower are time-resolved experiments with electrons, which are also performed in a magnetic field and at cryogenic temperatures. These experiments are pursued in this thesis and are presented in four main chapters. It was convenient to explain the photoconductive sampling measurement technique, which is used for time-resolved experiments, and to characterize the mesoscopic devices in DC transport separately in the first two chapters. Thereafter we use the photoconductive sampling technique to study the excitations in the frequency regime up to approximately 1 THz. The last chapter of this thesis deals with measurements which highlight non-linear properties of the device under study. This alternative measurement concept is referred to as electrical pulse correlation. The experiments presented in the chapters have triggered ideas for further experiments as well as suggestions how to improve the existing experiments.

Here we review each chapter and underline the main results of the studies. Subsequently, we suggest further experiments using the photoconductive sampling technique.

Chapter 2 establishes the basis of time-resolved transport experiments. Here we demonstrate the photoconductive sampling technique and study the propagation of a picosecond long electrical pulse along a coplanar waveguide. The waveguide contains two integrated photoconductive switches, each of which acts either as a source of short electrical pulses or as a detector of an ultrafast signal. We directly measured the pulse propagation velocity on the waveguide by employing its symmetry. The measured value of $0.32c$ deviates from the expected value of $0.39c$. Though this deviation is puzzling, it does not influence the further experiments. It was decisive to obtain the value of the propagation velocity, since it eases the understanding of pulse reflection in the waveguide as well as the interpretation of time-resolved transport experiment on a 2DES. Furthermore, the pulse propagation experiment exhibited not only the reflections at the end of the waveguide but also showed that the electrical pulse couples easily into any interruption of a waveguide structure which acts then as a parasitic waveguide. Additional peaks in the pulse propagation trace are the fingerprints of reflections at the ends of the parasitic waveguide. Unfortunately, the interruptions of the waveguide geometry are unavoidable when integrating

the switches or a device to be studied. Thus we suggest several approaches how to suppress or at least reduce these reflections. A waveguide with two switches allows to study either the transmission properties of the active device, when it is integrated between the switches, or its reflection properties, when the device is positioned on one side from the switches. To monitor both properties simultaneously, it is necessary to integrate more than two photoconductive switches. Therefore, we studied the pulse propagation along a waveguide geometry with four integrated switches. Finally, we describe how to configure a chip assembly for time-resolved transport experiments in a device made from a GaAs/AlGaAs heterostructure. Regarding the time-resolved transport experiments on a mesoscopic device, we argue for a device geometry that supports at least two electron trajectories of different lengths depending on the strength of the applied magnetic field. Such a geometry allows us to measure a relative time delay between the trajectories and eliminate other contributions to the delay time, which can not be predicted with sufficient accuracy.

Hence, in Chapter 3 we considered such mesoscopic devices based on a GaAs/AlGaAs heterostructure and characterized them in DC transport experiments. One of the devices is a modification of a conventional transverse magnetic focusing device; it is addressed as a corner device. Even though not anticipated, this novel device geometry enabled us to observe the effect of the disorder potential on the ballistic electron transport in macroscopic DC experiment. A part of the disorder potential originates from the charge fluctuation in the donor layer of the heterostructure, which perturbs the potential landscape of electrons by a few percent of the Fermi energy. This affects, however, considerably the electron ballistic transport - the electron flow forms branches. So far this phenomenon was only observed in scanning imaging experiment. When measuring the magnetoresistance curve in DC transport, the modification of the electron flow manifests itself in a variable shape of the first collimation peak. Its shape depends strongly on the potential landscape through which the electrons move. Hence, it is not surprising that the experiments performed on different pieces of the same heterostructure yield different shapes of the first collimation peak. Beside the collimation peak the corner device exhibits also peaks which appear due to the focusing of the electron trajectories by the magnetic field - magnetic focusing peaks. They are less sensitive to the influence of disorder. And therefore our device allows for studying the competition between two focusing mechanisms: random focusing by the disorder potential and deterministic focusing by the magnetic field. We stress that branching is not specific to the material used, the details of the geometry, it is a consequence of particle flow in a weak disorder potential. Therefore, when interpreting the results of experiments performed in the ballistic regime, one should always be aware of the effect of the disorder potential. The studies of the disorder potential should be performed on a heterostructure with a back gate, which would allow to tune the disorder potential continuously. The results of this experiment will likely allow to infer the structure of the disorder potential. The experiments can also be extended into the regime of high magnetic field, where the picture of composite fermions comes into play, to study the influence of the disorder potential onto the ballistic transport of the composite fermions.

Another type of mesoscopic device is mesoscopic cavity. We performed DC transport experiments on cavities of different shapes: triangular, square and hexagonal shape. These cavities also support electron trajectories of different lengths depending on the strength of the magnetic field. Magnetoresistance traces showed peaks which could be assigned to such electron trajec-

ories. The traces exhibit also additional peaks, which could not be explained in a simple model. Nevertheless, the ballistic cavities were proven to be alternative geometries for time-resolved studies.

In Chapter 4 a corner device was integrated into the waveguide structure. We described the time-resolved experiments on corner devices whose geometries are defined by depleting the 2DES either by wet chemical etching or by applying a voltage on top gates. These experiments did not yield the expected results. Therefore, we took a step back and performed time-resolved experiments in the magnetic field on a non-patterned rectangular stripe of a 2DES. The time domain data contained magnetic field independent signal, which could be related to the waveguide geometry, and magnetic field dependent signal. These latter revealed a wealth of collective plasmon excitations: bulk and edge magnetoplasmons. The various modes of plasmon excitations could be identified by Fourier transforming the time domain data. The Fourier spectrum showed the magnetoplasmon excitations with frequencies up to 0.5 THz. The phase of the Fourier transform eased the assignment of the wave vector to each excitation mode of the bulk magnetoplasmons. The wave vector is given by two numbers, which describe the wave vector quantization along the length and the width of the stripe. The experiments performed on stripes with different lengths and for two electron densities corroborate both the excitation of various plasmon modes and the wave vector assignment to each mode. Beside the excitation spectrum, the time-domain data also allowed to extract the pulse propagation velocity in the 2DES. It is $4.9 \cdot 10^6$ m/s for an electron density of $0.6 \cdot 10^{11}$ cm⁻² and $7.4 \cdot 10^6$ m/s for an electron density of $1 \cdot 10^{11}$ cm⁻².

Chapter 5 demonstrates another measurement method for time-resolved studies, which is referred to as electrical pulse correlation. This method probes the non-linearity of the system and is suggested as an alternative approach to measure the Fermi velocity in a mesoscopic device. The electrical pulse correlation was demonstrated on a stripe of the 2DES. The time domain data did not feature a magnetic field independent signal, like the one observed in the previous chapter. This is one of the advantages of this method - it does not require a pre-filtering of the signal. Further, the signal trace along the field axis at zero delay time can be correlated with the integer filling factor of the Landau levels: the correlation signal exhibits a dip whenever an even number of Landau levels is filled. Also the traces along the time axis at the filling factors 1 and 2 are out of phase. Furthermore, the Fourier transform of the correlation signal did not show the various excitation modes of the electron system, like in the previous chapter. Instead, it shows a single line, which can either be attributed to the ground mode of plasmon excitation or to the electron cyclotron line. This excitation extends up to a frequency of 1 THz. A remarkable feature of the spectrum is a line at the double frequency of the electron cyclotron resonance. The observation of lines at ω_c and $2\omega_c$ is a strong indication of a non-linearity in a two-dimensional electron gas, whose origin is not clear yet.

Beside the experiments with the GaAs-based two-dimensional electron gas, the time-resolved experiments can easily be extended to GaAs-based two-dimensional hole gas [64]. Due to a strong spin-orbit interaction in such a system [65, 66], Rokhinson et al. could demonstrate the spatial separation of hole spin states in a transverse magnetic focusing device [67]. Another GaAs-based system, that has recently attracted a lot of attention, is a bilayer of two-dimensional

electron system [68]. The DC magnetotransport measurements on such a system indicate a condensation of excitons composed of electrons and holes, which are located in two separated two-dimensional electron layers, when the total filling factor in both layers is 1. Commonly such structures contain a top- and back-gate to tune the electron density in each layer. An incorporation of such a structure into the three chip assembly raises a problem. The conducting gate planes change the waveguide structure of the central chip and make it incompatible with the waveguide patterned on the side chips with the photoconductive switches. Recently, an intrinsic density matching in both layers was achieved by proper engineering of the heterostructure [69]. This is an elegant way to omit both gates. Thus the time-resolved dynamical and non-linear properties of the double layer 2DES can be studied in the three chip configuration.

Two-dimensional charge carrier distributions are also found in other materials. One example is an isolated monolayer of carbon atoms - graphene. The linear dispersion of charge carriers in graphene distinguishes this material from the conventional GaAs-based heterostructures. Since the charge carriers in graphene can be described as massless relativistic particles, which obey the Dirac equation, one hopes to observe relativistic effects. This and the fact, that the conductivity in graphene can easily be changed between n-type and p-type, stimulated the research on it. Low dimensional carriers are also found in a novel class of heterostructures - oxide heterostructures. The most prominent are $\text{LaAlO}_3/\text{SrTiO}_3$ heterostructure, in which the superconductivity and its onset via tuning the electron density have been demonstrated [70, 71, 72], and MgZnO/ZnO heterostructure, in which both Integer and Fractional Quantum Hall Effect [73, 74] have been demonstrated. It would be enthralling to apply both the photoconductive sampling technique and the electrical pulse correlation method to learn about the dynamical and non-linear properties of these materials.

The three chip assembly used in this work facilitates the pulse propagation without reflection at the interface between the two adjacent chips due to almost identical dielectric constants of the GaAs-heterostructure and of the photoconductive material. The dielectric constants of alternative materials that contain low-dimensional carriers may differ from that of the photoconductive material used in this work and hence lead to the reflections at the interface. In fact, the dielectric constant of SrTiO_3 might be 300. As for the experiment with graphene, the central chip should contain a back gate to tune the density of charge carriers in the flake. This additional conducting plane modifies the waveguide structure of the central chip and makes it incompatible with the three-chip configuration introduced in the thesis.

Several strategies can be pursued to overcome the complications and to conduct the picosecond time-resolved experiment. One strategy involves the flip-chip bonding technique and can be applied for any suggested materials. The ohmic contacts of graphene/oxide heterostructure are then directly contacted with the corresponding part of the waveguide structure.

Alternatively, graphene, which is usually isolated on a Si substrate, can be transferred onto any other substrate using the method described for nanotubes [75]. We believe that also a controlled positioning of a graphene flake on the substrate is feasible. To conduct the time resolved experiment we suggest to use a GaAs material with an embedded Si-doped layer, that acts as a back gate for a graphene flake deposited on the substrate. On the same substrate the photoconductive LT-GaAs is grown only in the area where the photoconductive switches are patterned. Such a substrate can be easily grown with MBE. The subsequent structuring of the waveguide and the contacting of the graphene is an easy processing step.

As for oxides, we can profit from the interest of integrating oxide materials with the con-

ventional semiconductors [76,77]. There are reports about the growth of both SrTiO_3 and ZnO on GaAs substrate [78,79]. And therefore it is conceivable to grow an oxide heterostructure on the central chip of the three-chip assembly. But, due to a large lattice mismatch between the oxide materials and GaAs, the high-quality of oxide heterostructures grown on GaAs and the phenomena observed in them need to be verified.

Zusammenfassung und Ausblick

Die vorliegende Arbeit treibt das ambitionierte Projekt zur Durchführung der zeitaufgelösten Messungen mit Verbundfermionen in Nanostrukturen und mesoskopischen Bauelementen voran. Diese Quasiteilchen sind relevant in dem Regime des gebrochenzahligen Quanten-Halleffekts, der hohe Magnetfelder und tiefe Temperaturen erfordert. Eine Komplexitätstufe niedriger sind die zeitaufgelösten Messungen mit Elektronen angesiedelt, die aber auch in hohen Magnetfeldern und bei tiefen Temperaturen durchgeführt werden. Diese Experimente werden in vier Hauptkapiteln der vorliegenden Doktorarbeit präsentiert.

Die Photoleitungs-Sampling Methode, die für die zeitaufgelösten Messungen eingesetzt wird, und die Charakterisierung der mesoskopischen Bauelemente in DC Transport werden in den ersten zwei Kapiteln präsentiert. In dem darauf folgenden Kapitel wenden wir die Photoleitungs-Sampling Methode an, um die zeitaufgelösten Messungen an dem zwei-dimensionalen Elektronensystem (2DES) durchzuführen. Das letzte Kapitel beschreibt eine andere Messmethode, die die Nichtlinearität eines zu untersuchenden Bauelements hervorbringt. Die in den Kapitel präsentierten Experimente führten zu neuen Fragestellungen und haben Ideen für weitere Experimente und Verbesserungsvorschläge für den vorhandenen Messaufbau hervorgebracht.

Hier geben wir den Überblick über die einzelnen Kapitel und erläutern die wichtigen Ergebnisse jedes Kapitels. Anschließend schlagen wir weitere Experimente unter Anwendung der Photoleitungs-Sampling Methode vor.

Kapitel 2 bildet die Basis für die zeitaufgelösten Untersuchungen. Wir verwenden die Photoleitungs-Sampling Methode für die Untersuchungen der Propagation eines elektrischen Pulses entlang des Koplanaren Wellenleiters, der zwei Photoleitungsschalter enthält. Jeder dieser Photoschalter agiert entweder als der Erzeuger der kurzen elektrischen Pulsen oder als der Detektor des ultraschnellen Signals. Die Symmetrie des Wellenleiters erlaubt uns, die Pulspropagationsgeschwindigkeit direkt zu bestimmen. Sie beträgt $0.32c$ und weicht damit von dem erwarteten Wert von $0.39c$ ab. Obwohl die Gründe für diese Abweichung unklar sind, beeinflusst das in keiner Weise die weiteren Experimente. Entscheidend war nur die Bestimmung der Propagationsgeschwindigkeit. Dies erleichtert nicht nur die Interpretation der Propagationskurve des Pulses auf dem Wellenleiter, sondern trägt auch zum besseren Verständnis der zeitaufgelösten Messungen an dem 2DES in Kapitel 4 bei. Die zeitaufgelösten Untersuchungen auf dem Wellenleiter zeigen nicht nur Reflektionen des Pulses am Ende des Wellenleiters, sondern auch seine Kopplung in die Wellenleiterunterbrechungen, die als parasitäre Wellenleiter wirken. Zusätzliche Peaks in der Pulspropagationskurve stammen von der Reflektionen am Ende der parasitären Wellenleitern. Leider ist die Wellenleiterunterbrechung unvermeidbar, wenn die Schalter oder das zu untersuchende Bauelement in die Wellenleitergeometrie einge-

baut werden müssen. Daher schlagen wir vor, wie man die Reflektionen unterdrücken bzw. die Amplitude des reflektierenden Signals reduzieren kann. Ein Wellenleiter mit zwei eingebauten Schaltern ermöglicht die Untersuchungen entweder der Transmissionseigenschaften des zu untersuchenden Bauelements, wenn es zwischen den Schaltern eingebaut ist, oder der Reflektionseigenschaften, wenn das Bauelement auf einer Seite von beiden Schaltern positioniert ist. Um beide Eigenschaften gleichzeitig untersuchen zu können, müssen mehr als zwei Schalter in den Wellenleiter eingebaut werden. Deswegen wurde die Pulsausbreitung auf dem Wellenleiter mit vier eingebauten Schaltern untersucht. In dem Kapitel wird auch auf den Chipaufbau eingegangen, der für die zeitaufgelösten Messungen auf der GaAs/AlGaAs-basierten Heterostruktur geeignet ist. Im Hinblick auf die zeitaufgelösten Messungen in den mesoskopischen Bauelementen streben wir nach so einer Geometrie des Bauelements, die mindestens zwei Elektronentrajektorien unterstützt, deren Länge von der Stärke des angelegten Magnetfeldes abhängt. Diese Notwendigkeit ruht daher, dass nicht alle Beiträge zu der gemessenen Zeit mit einer hohen Genauigkeit vorhergesagt werden können. Allerdings schließt die Messung der relativen Transportzeit entlang der zwei Trajektorien derartige Beiträge aus.

Daher betrachten wir im Kapitel 3 solche Bauelemente, die auf einer GaAs/AlGaAs-Heterostruktur basieren. Eines der Bauelemente ist eine modifizierte Geometrie der transversalen Anordnung für die Fokussierung des Elektronflusses im Magnetfeld. Diese neue Geometrie wird in dieser Arbeit als Ecke bezeichnet. Die neue Geometrie ermöglichte den Einfluss des Unordnungspotentials auf den ballistischen Elektronentransport in einem einfachen DC-Transportexperiment zu beobachten. Ein Teil des Unordnungspotentials entsteht durch Ladungsfluktuationen in der Donatorenschicht der Heterostruktur. Diese Störung der Potentiallandschaft der Elektronen beträgt nur weniger Prozent der Fermienergie. Trotz des angeblich kleineren Einflusses auf die Elektronenbewegung, wird der Elektronentransport stark beeinflusst. Der Elektronenfluss wird fokussiert und bildet Zweige aus. Bis jetzt wurde dieses Phänomen nur mit Rastersondenmikroskopie beobachtet. In der DC-Transportmessung äußert sich die Änderung des Elektronenflusses in der Änderung der Form des Kollimationspeaks, die stark davon abhängt, in welcher Potentiallandschaft sich Elektronen bewegen. Deswegen ist es auch nicht verwunderlich, dass die an unterschiedlichen Bereichen der gleichen Heterostruktur durchgeführten Messungen unterschiedliche Formen des Kollimationspeaks zeigen. Außer dem Kollimationspeak werden Peaks beobachtet, die durch die Fokussierung des Elektronflusses in dem Magnetfeld zustandekommen. Sie sind weniger empfindlich auf die von dem Unordnungspotential verursachten Störungen des Elektronflusses als der Kollimationspeak. Damit ermöglicht unser Bauelement die Untersuchungen von zwei Fokussierungsmechanismen: zufällige Fokussierung des Elektronenflusses durch das Unordnungspotential (Verzweigung) und deterministische Fokussierung des Elektronenflusses in dem Magnetfeld. Wir betonen, dass die Verzweigung des Elektronflusses weder die materialspezifisch ist noch von der Geometrie des Bauelements abhängt. Sie ist lediglich die Konsequenz der Elektronenbewegung in einem Unordnungspotential. Daher muss stets der Einfluss des Unordnungspotentials bei der Interpretation der im ballistischen Regime durchgeführten Experimente berücksichtigt werden. Die weiteren Untersuchungen sollten an einer Heterostruktur mit einer Rückseitenelektrode gemacht werden, das eine kontinuierliche Änderung des Unordnungspotentials ermöglicht. Es ist vorstellbar, dass die Struktur des Unordnungspotentials aus solchen Messungen ersichtlicht werden kann. Solche Experimente können in den Bereich hoher Magnetfelder erweitert wer-

den, indem der Transport mit Verbundfermionen beschrieben werden kann. Dabei sind Experimente möglich, die den Einfluss des Unordnungspotentials auf die ballistische Bewegung der Verbundfermionen untersuchen.

Eine andere Klasse der mesoskopischen Bauelemente sind mesoskopische Resonatoren. In DC-Transportexperimenten charakterisieren wir Resonatoren unterschiedlicher Geometrie: Dreieck-, Viereck- und Sechseck-Resonatoren. Auch sie unterstützen Trajektorien unterschiedlicher Länge, die von der Stärke des angelegten Magnetfeldes abhängen. Die Magnetwiderstandskurven zeigen Peaks, die solchen Trajektorien zugeordnet werden können. Zusätzliche Peaks sind ebenfalls vorhanden, die allerdings in einem einfachen Modell nicht erklärt werden können. Trotzdem können diese Resonatoren für die zeitaufgelösten Messungen eingesetzt werden.

Im Kapitel 4 integrieren wir die Ecke in den Wellenleiter. Wir zeigen zeitaufgelöste Messungen an diesem Bauelement, dessen Geometrie durch die Enträumung des 2DESs entweder durch das Anlegen der Spannung an Oberflächen Elektroden oder durch das Ätzen der Heterostruktur definiert ist. Leider ist der Erfolg bei diesen Experimenten ausgeblieben. Daraufhin wurde das Bauelement vereinfacht, in dem die Oberflächenstrukturen entfernt wurden und nur ein Streifen des Elektronengases verblieb. Die auf dem Streifen gewonnenen Zeitbereichsdaten zeigen ein magnetfeldunabhängiges Signal, das mit der Geometrie des Wellenleiters assoziiert ist, und ein magnetfeldabhängiges Signal. Die Fouriertransformation des Signals entlang der Zeitachse zeigte die Anregung mehrerer Moden der Magnetoplasmonen mit Frequenzen bis zu 0.5 THz. Die Phase der Fouriertransformation ermöglichte die Zuordnung des Wellenvektors zu jeder Anregungsmode. Dieser Wellenvektor ist durch zwei Zahlen gegeben, die seine Quantisierung entlang der Länge und der Breite des Streifens beschreiben. Die Experimente wurden für Streifen unterschiedlicher Länge und für zwei Ladungsträgerdichten durchgeführt und bestätigten sowohl die Anregung der unterschiedlichen Moden als auch die Wellenvektorzuzuordnung. Außer dem Anregungsspektrum kann man aus den Zeitbereichsdaten auch die Propagationsgeschwindigkeit des Pulses im 2DES bestimmen. Sie beträgt $4.9 \cdot 10^6$ m/s für eine Elektronendichte von $0.6 \cdot 10^{11} \text{ cm}^{-2}$ und $7.4 \cdot 10^6$ m/s für eine Elektronendichte von $1 \cdot 10^{11} \text{ cm}^{-2}$.

Kapitel 5 behandelt einen anderen Ansatz für die zeitaufgelösten Untersuchungen. Er basiert auf der Korrelation der elektrischen Pulse. Diese neue Methode eignet sich für die Untersuchung der nichtlinearen Eigenschaften des 2DES und wird von uns als alternativer Ansatz zur Messung der Fermigeschwindigkeit in mesoskopischen Bauelementen vorgeschlagen. Diese Methode ist für Experimente am Streifen des Elektronengases angewendet worden. Die Zeitbereichsdaten zeigen kein eindeutiges magnetfeldunabhängiges Signal, wie es in dem vorherigen Kapitel zu sehen war. Dies ist einer der Vorteile dieser Methode - es ist keine zusätzliche Analyse der Messdaten notwendig. Darüberhinaus kann die Messkurve entlang der Magnetfeldachse bei Zeitpunkt Null mit den ganzzahligen Füllfaktoren der Landauniveaus korreliert werden; die Messkurve zeigt einen Dip bei geradzahligen Füllfaktoren. Betrachtet man nun die Kurven entlang der Zeitachse bei Füllfaktor 1 und 2, so sind sie um 180° phasenverschoben. Des Weiteren zeigt das Spektrum des Korrelationssignals keine Anregung der unterschiedlichen Moden, wie in dem vorherigen Kapitel zu beobachten war. Stattdessen ist eine Linie im Spektrum zu sehen, die entweder als die Anregung der Plasmonengrundmode oder als Elektronenzyklotronresonanzlinie interpretiert werden kann. Diese Anregung ist bis zu 1 THz zu sehen.

Bemerkenswert ist das Auftreten einer Spektralkomponente bei der doppelten Frequenz der Elektronzyklotronresonanzfrequenz. Das Vorhanden der Linien bei ω_c and $2\omega_c$ ist ein starker Hinweis auf die Nichtlinearität in dem Elektronengas.

Neben den Experimenten mit dem GaAs-basiert Elektronengas können zeitaufgelöste Messungen leicht auf die GaAs-basierten zwei-dimensionalen Lochgase erweitert werden [64]. Aufgrund der stärkeren Spin-Orbit-Wechselwirkung in solchen System [65,66], zeigten Rokhinson u.a. räumliche Trennung der Spinzustände in dem magnetischen Fokussierungsexperiment [67]. Ein anderes GaAs-basiertes System ist die Doppellage des zwei-dimensionalen Elektrongases [68]. DC-Messungen an solchen Systemen lassen die Kondensation der Exzitonen, die aus einem Elektron in einer Schicht und einem Loch in der anderen Schicht gebildet werden, beim Gesamtfüllfaktor 1 vermuten. Der Einbau eines solchen Bauelements in die Dreichipanordnung führt dazu, dass die Wellenleitergeometrie des mittleren Chips inkompatibel mit der Wellenleitergeometrie der seitlichen Chips wird, da die leitenden Flächen der Elektroden die Wellenleiterstruktur des mittleren Chips verändern. Durch die Änderung des Heterostruktur-aufbaus wurde der intrinsische Ausgleich der Ladungsträgerdichten vor Kurzem erreicht [69]. Das ist ein eleganter Weg, den Einsatz der Oberflächenelektrode und der Rückseitenelektrode zu vermeiden. Somit kann das aus der Doppellage des zwei-dimensionalen Elektrongases bestehende Bauelement in die Dreichipanordnung eingebaut werden, was die Durchführung der zeitaufgelösten Messungen ermöglicht.

Zwei-dimensionale Ladungsverteilungen existieren auch in den anderen Materialien. Ein Beispiel dazu ist eine isolierte Monolage von Kohlenstoffatomen - Graphen. Die lineare Dispersion der Ladungsträger in Graphen unterscheidet dieses Material von der konventionellen GaAs-Heterostruktur. Da die Ladungsträger in Graphen als relativistische Teilchen ohne Masse beschrieben werden, die der Dirac-Gleichung gehorchen, wird es spekuliert, dass relativistische Effekte in Graphene beobachtet werden können. Das und die Tatsache, dass die Graphen-Leitfähigkeit leicht zwischen n-Leitung und p-Leitung geändert werden kann, stimulieren die Forschung an Graphen. Niederdimensionale Ladungsträger können auch in neuartigen Heterostrukturen gefunden werden - Oxid-Heterostrukturen. Zwei Beispiele davon sind die $\text{LaAlO}_3/\text{SrTiO}_3$ -Heterostruktur, in der Supraleitung und ihre Entstehung durch die Änderung der Ladungsdichte demonstriert wurden [70, 71, 72], sowie die MgZnO/ZnO -Heterostruktur, in der der ganzzahlige und gebrochenzahlige Quanten-Halleffekt demonstriert wurden [73, 74]. Es wäre interessant, die Photoleitungs-Sampling Methode und die Pulskorrelationsmethode für die Untersuchungen der Dynamik und Nichtlinearität derartiger Materialien anzuwenden. Dafür müssen die neuen Strukturen in die Dreichipanordnung integriert werden.

Die Dreichipanordnung lebt davon, dass es keine Reflektionen am Übergang zwischen den benachbarten Chips gibt, da die Dielektrizitätskonstanten der GaAs-Heterostruktur und des photoleitenden Materials fast identisch sind. Die Dielektrizitätskonstante eines anderen 2DES enthaltenden Materials kann sich von der des photoleitenden Materials unterscheiden. Dies würde dann zu Reflektionen am Übergang führen. Das ist der Fall für SrTiO_3 ; seine relative Dielektrizitätskonstante beträgt 300. Was die Experimente mit Graphen betrifft, so sollte der mittlere Chip eine Rückseitenelektrode enthalten, um die Ladungsträgerdichte in der Graphenflocke zu verändern. Die leitende Fläche des Backgates verändert allerdings die Wellenleitergeometrie des mittleren Chips und macht diesen Wellenleiter inkompatibel mit den Wellenleitern der

seitlichen Chips.

Wir schlagen Lösungsansätze vor, wie man die mit der Zusammensetzung der unterschiedlichen Materialien verbundenen Schwierigkeiten überwinden kann. Die Flip-Chip Montage ist einer der Ansätze. Hier werden die ohmschen Kontakte von Graphen/Oxid-Heterostruktur direkt mit der Wellenleiterstruktur verbunden.

Alternativ kann Graphen, das meist auf einem Si-Substrat präpariert wird, auf ein anders Substrat mit der Methode übertragen werden, die für Übertragung von Kohlenstoff-Nanoröhrchen beschrieben wurde [75]. Dabei ist eine kontrollierte Positionierung der Graphenflocke auf dem neuen Substrat durchaus vorstellbar. Für die zeitaufgelösten Messungen bietet sich GaAs mit einer Si-dotierten Schicht an, die hier als Rückseitenelektrode agiert. Auf dem gleichen Substrat kann ein photoleitendes LT-GaAs an den Stellen gewachsen werden, wo die Photoschalter strukturiert werden sollen. Ein solches GaAs-Substrat kann problemlos mittels Molekularstrahlepitaxie gewachsen werden. Die darauf folgende Strukturierung des Wellenleiters und die Flockenkontaktierung sind unkomplizierte Prozessschritte.

Was die Oxide betrifft, so können wir von den Anstrengungen profitieren, Oxidmaterialien mit konventionellen Halbleitern zu kombinieren [76, 77]. So wird zum Beispiel darüber berichtet, dass sowohl SrTiO_3 als auch ZnO auf GaAs gewachsen werden können. Somit können die Oxid-Heterostrukturen auf dem mittleren (GaAs) Chip gewachsen und strukturiert werden. Eine der offenen Fragen ist, ob aufgrund der Gitterfehlangepassung zwischen Oxidstrukturen und GaAs-Substrat die gleichen Phänomene zu beobachten sind, wie in den Oxidstrukturen, die auf dem gitterangepassten Substrat gewachsen sind.

Appendix A

Calculations for CPW

In quasi-static approximation the wave impedance of the coplanar waveguide is given by:

$$Z_0 = \frac{1}{4c\epsilon_0} \frac{1}{\sqrt{\hat{\epsilon}_{qs}}} \frac{1}{\mathcal{K}(\hat{q}_{cpw})} \quad (\text{A.1})$$

where

$$\mathcal{K}(\hat{q}_{cpw}) = \frac{K(\hat{q}_{cpw})}{K(\sqrt{1 - \hat{q}_{cpw}^2})} \quad (\text{A.2})$$

with K is the complete elliptic integral of the first kind and \hat{q}_{cpw} given by

$$\hat{q}_{cpw} = \frac{s + \Delta}{s + 2w - \Delta}. \quad (\text{A.3})$$

Here s is the width of the central conductor, w is the distance from the central conductor to the ground plane. The parameter Δ is given by

$$\Delta = \frac{1.25d}{\pi} (1 + \ln(\frac{4\pi s}{d})), \quad (\text{A.4})$$

where d is the thickness of the evaporated metal. The parameter $\hat{\epsilon}_{qs}$ is the effective quasistatic dielectric constant give by:

$$\hat{\epsilon}_{qs} = \epsilon_{qs} - \frac{0.7(\epsilon_{qs} - 1)\frac{d}{w}}{\mathcal{K}(q_{cpw}) + 0.7\frac{d}{w}} \quad (\text{A.5})$$

with

$$\epsilon_{qs} = \frac{\epsilon_r + 1}{2} \left\{ \tanh \left[1.785 \log \frac{h}{w} + 1.75 \right] + \frac{wq_{cpw}}{h} [0.04 - 0.7q_{cpw} + 0.01(1 - 0.1\epsilon_r)(0.25 + q_{cpw})] \right\}, \quad (\text{A.6})$$

where ϵ_r is the dielectric constant of the substrate, h is the thickness of the substrate and the geometrical factor q_{cpw} is given by

$$q_{cpw} = \frac{s}{s + 2w}. \quad (\text{A.7})$$

In the quasistatic limit the signal propagates with a velocity:

$$v_{qs} = \frac{c}{\sqrt{\hat{\epsilon}_{qs}}} \quad (\text{A.8})$$

According to Eq. A the wave impedance of a CPW with $s = 20 \mu\text{m}$ and $w = 10 \mu\text{m}$ is $Z_0 = 43 \Omega$. Here we assumed the typical experimental values for the substrate thickness $h = 500 \mu\text{m}$ and the thickness of the evaporated metal $d = 300 \text{nm}$.

The quasi-static approximation is valid only for the wavelength which are larger than the dimension of the coplanar waveguide. Beyond the quasi-static approximation, i.e. the wavelength is comparable with the CPW dimension, the dielectric constant becomes frequency dependent [80]. This leads to a frequency dependent dispersion and influences therefore the pulse propagation in a CPW [80, 81]. The pulse propagation is also influenced by the skin effect, which implies the frequency dependence of the CPW conductivity. We neglect the skin effect here, as its contribution is small compared with the modal dispersion. The total dispersion can be written as:

$$\frac{\omega}{c} \sqrt{\hat{\epsilon}_{qs}} + \frac{\omega}{c} \sqrt{\epsilon_{mod}(\omega)} \quad (\text{A.9})$$

The modal dispersion is given [82] by

$$\sqrt{\epsilon_{mod}(\omega)} = \frac{\sqrt{\epsilon_r} - \sqrt{\hat{\epsilon}_{qs}}}{1 + u_0 \left(\frac{\omega_{TE}}{\omega}\right)^{1.8}}. \quad (\text{A.10})$$

The cut-off frequency ω_{TE} of the lowest TE mode is given by

$$\omega_{TE} = \frac{\pi c}{2h\sqrt{\epsilon_r - 1}}. \quad (\text{A.11})$$

The parameter u_0 is given by

$$\log u_0 = u_1 \log \left(\frac{s}{w}\right) + u_2 \quad (\text{A.12})$$

and

$$u_1 = 0.54 - 0.64u_3 + 0.015u_3^2 \quad (\text{A.13})$$

$$u_2 = 0.43 - 0.86u_3 + 0.540u_3^2 \quad (\text{A.14})$$

$$u_3 = \log \left(\frac{s}{h}\right). \quad (\text{A.15})$$

Appendix B

Fiber Alignment and Gluing

The time-resolved transport experiments presented in this thesis use photoconductive switches to generate the short electrical pulses and to detect the ultrafast signals. Each switch is driven by an optical fiber, which is glued above it. Here we describe the procedure how to position the fiber above the switch and to fix it there. The fiber end is fixed on a wedge shaped holder with a piece of a soft magnet. The wedge is placed on a nanomanipulator¹, which moves the wedge in three spatial directions. This allows for the positioning of the fiber tip above the switch. Figure B.1 shows the circuit scheme, which is used during the alignment. A chopper modulates the optical pulse train before it is being coupled into the fiber. The modulation frequency is 800 Hz. A DC voltage is applied across the switch. It is typically 5 V. Due to the modulated irradiation of the photoconductive switch, an AC photocurrent is induced in the switch. A lock-in amplifier measures the voltage drop, which is induced in the secondary coil of the transformer. This signal is monitored during the fiber alignment. An optimal fiber position is achieved once the signal on two lock-in amplifiers is equal. In our experiment we use only one switch. Therefore, the optimal position is achieved once the induced signal is the largest. With a piece of a steel wire we apply a drop of optical glue² on the switch. To fix the fiber at place we cure the glue with a UV-light for about 40 minutes. Due to the mechanical tension the fiber tip is being moved as the curing begins. It is possible to slightly reposition the fiber at the begin of curing process. At the end of the curing procedure the induced signal drops usually by 20 % from its original value. Since the experimental setup allows to fix only one fiber at time, the gluing procedure described above is repeated for all switches which are involved in the experiment.

¹Melles Griot piezoelectric controller

²adhesive NOA61 purchased by Thorlabs

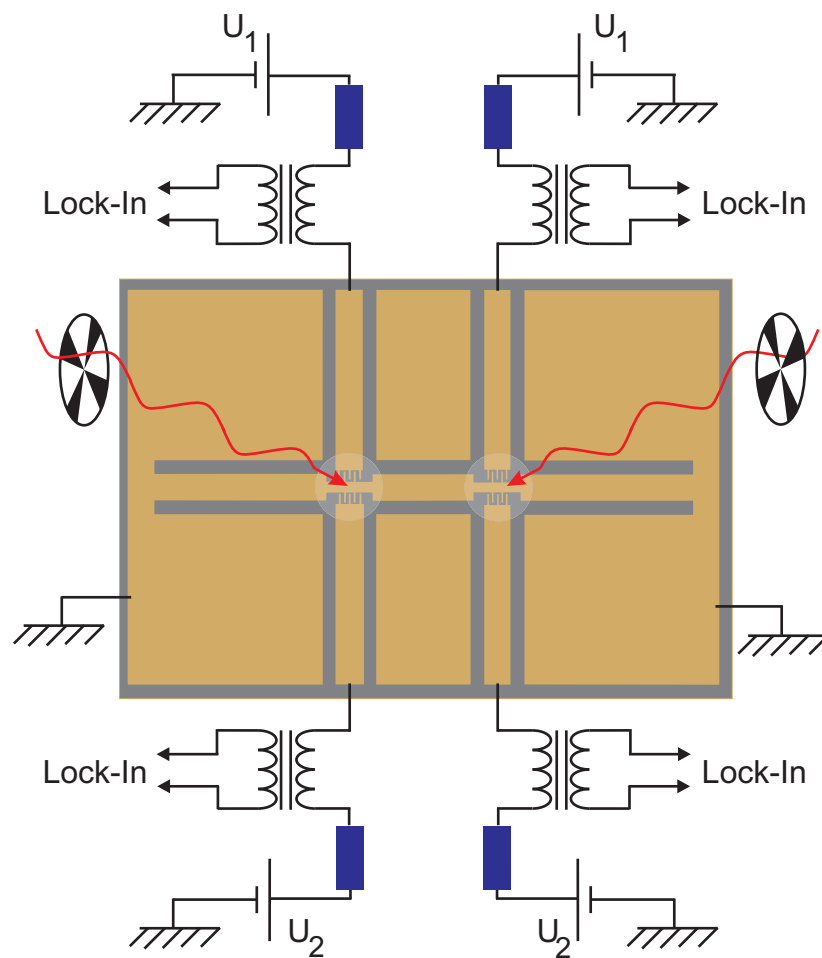


Figure B.1: Circuit scheme to monitor the photocurrent in the photoconductive switch during the fiber alignment.

Appendix C

Sample Fabrication

The experiments presented in this thesis are performed on two material classes: photoconductive material and GaAs/AlGaAs heterostructure, which contains a two-dimensional electron system. The heterostructure VU-495 is kindly provided by Dr. Vladimir Umansky (Weizmann Institute of Science, Israel). The 2DES in this structure is 147 nm beneath the surface and the spacer thickness is 65 nm. The photoconductive material was supplied by two groups. At the begin of the thesis Prof. Werner Dietsche (Max-Planck Institute for Solid State Research, Stuttgart) provided GaAs grown at low temperature. Later the experiments were adopted to the 1550 nm wavelength. The group of Prof. A. C. Gossard (Materials Department, UCSB, USA) provided ErAs:In_{0.53}Ga_{0.47} photoconductive material with 20 nm period and the active layer thickness of 2 μm ¹.

The three chip assembly, which is used in this thesis, is configured out of the photoconductive material and the GaAs/AlGaAs heterostructure. Before assembling the chip, we have to reassure that all three chips have the same thickness. The thickness of a chip is measured looking at its facet under the optical microscope with a calibrated scale. If necessary, the thicker material has to be abraded down to the thickness of the thinner material. In this work the photoconductive material was roughly 100 μm thicker than the GaAs heterostructure.

In following we describe the processing steps to fabricate the sample.

C.0.1 Mesa definition

Mesa is defined only on a high mobility sample with optical lithography.

- clean the pieces
- spin S1805 photoresist for 30 seconds at 4500 min^{-1} .
- bake at 90°C for 2 minutes.
- align the sample and expose it for 6 seconds with the MESA part of the mask.
- develop for 30 seconds in AZ726.

We use the following mixture to etch the mesa

¹wafer number 070326A.

- mixture $\text{H}_2\text{O}:\text{H}_2\text{O}_2:\text{H}_2\text{SO}_4$ 1000:4:1.

The etch rate of this mixture is about 40 nm/sec. To calibrate the etching rate use a dummy sample out of GaAs. Note, the etch rate of a heterostructure is 1.2 times faster than that of the dummy material.

C.0.2 Ohmic contacts

The following receipt for making of the ohmic contacts worked well

- clean the pieces
- spin AZ photoresist for 30 seconds at 6000 min^{-1} .
- bake at 90°C for 4 minutes.
- expose it for 6 seconds with the Ohmic Contact part of the mask.
- bake it for 1 minute at 123°C .
- float exposure for 35 seconds.
- develop for 35 seconds.

cleaning procedure

- process sample in O_2 -plasma for 30 seconds at pressure 0.3 Torr and power 200W.
- immerse sample in "Semico Clean" for 120 seconds .
- Dip sample in DI-water for 5 seconds.
- Dip HCl for 2 seconds.
- Dip in DI-water for 1 second.

After cleaning place the sample in evaporation machine within 5 minutes. Pump the evaporator until the pressure reached the region of 10^{-6} mbar. Evaporate consequently the metal films.

- 7 nm Ni
- 140nm Ge
- 280nm Au
- 36nm Ni

After metal evaporation, immerse sample into acetone, wait for the photoresist to dissolve, metal will only stick at the predefined areas. After liftoff the ohmic contact has to be annealed. Use annealing oven AZ500 with forming gas. Make sure the following settings of the annealing procedure

- 370°C for 120 seconds
- 440°C for 120 seconds

C.0.3 Alignment marks for ebeam lithography

If the active device is intended for the experiments with corner device, one structures the alignment marks with optical lithography.

- clean the pieces
- spin AZ5214 photoresist for 30 seconds at 6000 min^{-1} .
- bake at 90°C for 4 minutes. Here it is important to remove the photoresist from the sample edges. For this expose the edges of the sample for 5 minutes and develop thereafter for 40 seconds.
- expose the sample for 6 seconds with the Alignment Marks part of the mask.
- bake it for 1 minute at 123°C .
- float exposure for 30 seconds.
- develop for 35 seconds.

evaporate

- 20 nm Cr
- 120nm Au

The devices were written by Ulrike Waizmann from the Max-Planck-Institute, Stuttgart, Germany, specialized in e-beam lithography. The structures were written with Leica EBL 100-03 e-beam lithography machine.

C.0.4 Pads

Pads are needed to contact the structure written with e-beam lithography.

- clean the sample.
- spin AZ5214 photoresist for 30 seconds at 6000 min^{-1} .
- bake at 90°C for 4 minutes.
- expose it for 6 seconds with the Pad part of the mask.
- bake it for 1 minute at 123°C .
- float exposure for 35 seconds.
- develop for 35 seconds.
- Deposit metallization 20 nm Cr/ 120 nm Au.
- Liftoff.

C.0.5 Coplanar waveguide

The coplanar wave guides are patterned the photoconductive material as well as on the GaAs heterostructure.

- clean the pieces
- spin AZ5214 photoresist for 30 seconds at 6000 min^{-1} .
- bake at 90°C for 4 minutes.
- expose the sample for 6 seconds with the Waveguide part of the mask.
- bake it for 1 minute at 123°C .
- float exposure for 30 seconds
- develop for 35 seconds

evaporate

- 20 nm Cr
- 300nm Au

C.0.6 Three-chip assemble

After the samples are structured a three chip assemble, which consists of photoconductive and high mobility materials, can be built up. We separate a single active device from the processed chip by cleaving it. Commonly several active devices are fabricated on a single chip. Also the chip with a CPW structure is cleaved between photoconductive switches. The surface of a cleaved facet should be mirror like, i.e. it may not contain any crystal lattice defects, for instance crystal steps. The presence of this defect complicates the building of the assemble. When handling the samples after the cleaving one has to be careful not to touch the cleaved edges.

Now the samples has to be configured in three chip assemble. Figure C.1 shows the appliance for this. We put a dummy piece (shown in blue in Fig. C.1) of GaAs or InAs with a size, which is slightly larger than the size of the three chips together. A piece of the thermoplastic epoxy film ² with the same size is put on top of the dummy piece. The three chips (photoconductive material is shown in green and GaAs heterostructure is shown in red in Fig. C.1) are put on top of the film. The center conductors of CPWs on both interfaces are aligned under microscope with a needle. The spring pins sticking from the side arm push the assemble aside and fix the assemble's alignment. Another piece of GaAs wafer is put on top of the configuration and covers it completely. A square shaped head applies a pressure over the whole assemble and assures that the assemble's surface is flat. To cure the thermoplastic film we put the appliance with the assembled chip in an oven at 150°C for about 13 minutes. Thereafter the system should cool down in a natural way. After taking the assemble from the appliance, one should check for

²Cookson electronics, Staystick 472 with 3mil thickness

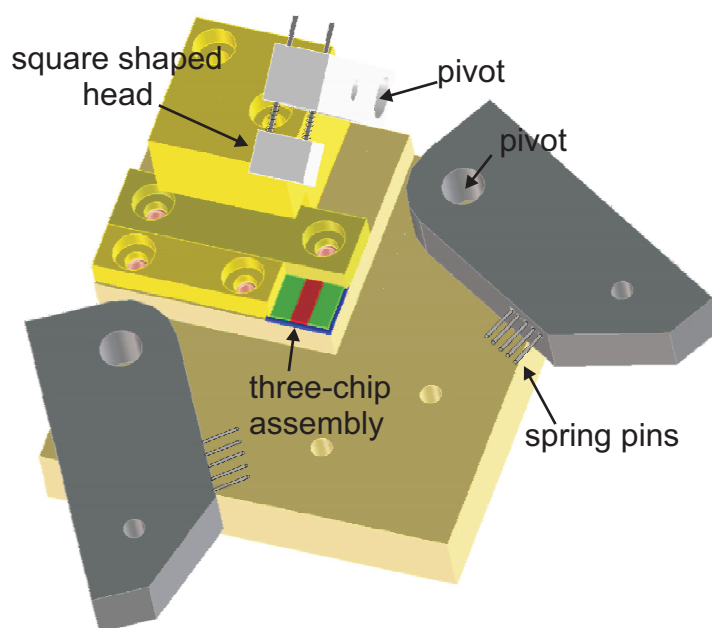


Figure C.1: Appliance to assemble three chip configuration.

a step and a gap at the interface under the microscope. This is a crucial check before applying a silver epoxy. A too large step or a too wide gap retards the application of the silver epoxy. If the gap is smaller than $1\ \mu\text{m}$ and the step is smaller than $2\ \mu\text{m}$ the sample is put in a chip carrier.

The silver epoxy droplets are applied between the corresponding parts of the coplanar waveguide. We use a stamp³ with a tip diameter of $12.7\ \mu\text{m}$. It is fixed in a bonder machine, which operates in manual modus. To cure the silver epoxy we put the chip assemble in an oven at 90°C for 90 minutes.

³Micronnect BV

Bibliography

- [1] K. von Klitzing, G. Dorda, and M. Pepper. New method for high-accuracy determination of the fine-structure constant based on quantized hall resistance. *Phys. Rev. Lett.*, 45:494, 1980.
- [2] D. C. Tsui, H. L. Störmer, and A. C. Gossard. Two-dimensional magnetotransport in the extreme quantum limit. *Phys. Rev. Lett.*, 48:1559, 1982.
- [3] R. B. Laughlin. Quantized hall conductivity in two dimensions. *Phys. Rev. B*, 23:5632, 1981.
- [4] B. I. Halperin. Quantized hall conductance, current-carrying edge states, and the existence of extended states in a two-dimensional disordered potential. *Phys. Rev. B*, 25:2185, 1982.
- [5] R. B. Laughlin. Anomalous quantum hall effect: An incompressible quantum fluid with fractionally charged excitations. *Phys. Rev. Lett.*, 50:1395, 1983.
- [6] J. K. Jain. Composite-fermion approach for the fractional quantum hall effect. *Phys. Rev. Lett.*, 63:199, 1989.
- [7] B. I. Halperin, Patrick A. Lee, and Nicholas Read. Theory of the half-filled landau level. *Phys. Rev. B*, 47:7312, 1993.
- [8] V. J. Goldman, B. Su, and J. K. Jain. Detection of composite fermions by magnetic focusing. *Phys. Rev. Lett.*, 72:2065, 1994.
- [9] J. H. Smet, D. Weiss, R. H. Blick, G. Luetjering, K. von Klitzing, R. Fleischmann, R. Ketzmerick, T. Geisel, and G. Weimann. Magnetic focusing of composite fermions through arrays of cavities. *Phys. Rev. Lett.*, 77:2272, 1996.
- [10] I. V. Kukushkin, J. H. Smet, K. von Klitzing, and W. Wegscheider. Cyclotron resonance of composite fermions. *Nature*, 415:409, 2002.
- [11] Martin Griebel. *Ultraschnell Ladunsträgerdynamik in LTG-GaAs und ErAs:GaAs-Übergittern – Grundlagen und Anwendungen*. PhD thesis, Max-Planck-Institut für Festkörperforschung, 2002.
- [12] D. H. Auston. Picosecond optoelectronic switching and gating in silicon. *Appl. Phys. Lett.*, 26:101, 1975.

- [13] P. R. Smith, D. H. Auston, A. M. Johnson and J. C. Bean. Picosecond optoelectronic detection, sampling, and correlation measurements in amorphous semiconductors. *Appl. Phys. Lett.*, 37:371, 1980.
- [14] Chi H. Lee. *Picosecond optoelectronic devices*. 1984.
- [15] S.Y. Chou, Y. Liu, W. Khalil, T.Y. Hsinag, and S. Alexandrou. Ultrafast nanoscale metal-semiconductor-metal photodetectors on bulk and low-temperature grown GaAs. *Appl. Phys. Lett.*, 61:819, 1992.
- [16] S.Y. Chou and M. Y. Liu. Nanoscale terahertz metal-semiconductor-metal photodetectors. *IEEE J. Quantum Electron.*, 28:2358, 1992.
- [17] David C. Look. Molecular beam epitaxial GaAs grown at low temperatures. *Thin Solid Films*, 231:61, 1993.
- [18] Gerald L. Witt. LTMBE–GaAs: present status and perspectives. *Materials Science and Engineering*, B22:9, 1993.
- [19] M. Griebel, J. H. Smet, D. C. Driscoll, J. Kuhl, C. Alvarez Diez, N. Freytag, C. Kadow, A. C. Gossard, and K. von Klitzing. Tunable subpicosecond optoelectronic transduction in superlattices of self-assembled ErAs islands. *Nature Materials*, 2:122, 2003.
- [20] F. Ospald, D. Maryenko, K. von Klitzing, D. C. Driscoll, M. P. Hanson, H. Lu, A. C. Gossard, and J. H. Smet. 1.55 μm ultrafast photoconductive switches based on ErAs:InGaAs. *Appl. Phys. Lett.*, 92:131117, 2008.
- [21] D. C. Driscoll, M. P. Hanson, A. C. Gossard, and E. R. Brown. Ultrafast photoresponse at 1.55 μm in InGaAs with embedded semimetallic ErAs nanoparticles. *Appl. Phys. Lett.*, 86:051908, 2005.
- [22] K. C. Gupta, Ramesh Garg, and I. J. Bahl. *Microstrip Lines and Slotlines*. 1979.
- [23] N.Zamdmer, Qing Hu, S.Vergheese, and A.Förster. Mode-discriminating photoconductor and coplanar waveguide circuit for picosecond sampling. *Appl. Phys. Lett.*, 74:1039, 1999.
- [24] N. G. Paulter, D. N. Sinha, A. J. Gibbs, and W. R. Eisenstadt. Optoelectronic measurements of picosecond electrical pulse propagation in coplanar waveguide transmission lines. *IEEE Transactions on Microwave Theory and Techniques*, 37:1612, 1989.
- [25] U. Rössler and D. Strauch. Group IV elements, IV–IV and III–V compounds. part b - electronic, transport, optical and other properties, 2002.
- [26] B. J. van Wees, H. van Houten, C. W. J. Beenakker, J. G. Williamson, L. P. Kouwenhoven, D. van der Marel, and C. T. Foxon. Quantized conductance of point contacts in a two-dimensional electron gas. *Phys. Rev. Lett.*, 60:848, 1988.
- [27] D. A. Wharam, T. J. Thornton, R. Newbury, M. Pepper, H. Ahmed, J. E. F. Frost, D. G. Hasko, D. C. Peacock, D. A. Ritchie, and G. A. C. Jones. Quantized conductance of point contacts in a two-dimensional electron gas. *J. Phys. C: Solid State Phys.*, 21:L209, 1988.

- [28] H. Z. Zheng, H. P. Wei, D. C. Tsui, and G. Weimann. Gate-controlled transport in narrow GaAs/Al_xGa_{1-x}As heterostructures. *Phys. Rev. B*, 34:5635, 1986.
- [29] H. van Houten, C. W. J. Beenakker, and B. J. van Wees. *Quantum Point Contacts*, volume 35 of *Semiconductors and Semimetals*. 1992.
- [30] L. W. Molenkamp, A. A. M. Staring, C. W. J. Beenakker, R. Eppenga, C. E. Timmering, J. G. Williamson, C. J. P. M. Harmans, and C. T. Foxon. Electron-beam collimation with a quantum point contact. *Phys. Rev. B*, 41:1274, 1990.
- [31] C. W. J. Beenakker and H. van Houten. *Quantum Transport in Semiconductor Nanostructures*, volume 44 of *Solid State Physics*. 1991.
- [32] J. D. Lawrence. *A Catalog of Special Plane Curves*. New York: Dover, 1972.
- [33] E. H. Lockwood. *A Book of Curves*. Cambridge University Press, 1967.
- [34] H. van Houten, C. W. J. Beenakker, J. G. Williamson, M. E. I. Broekaart, P. H. M. van Loosdrecht, B. J. van Wees, J. E. Mooij, C. T. Foxon, and J. J. Harris. Coherent electron focusing with quantum point contacts in a two-dimensional electron gas. *Phys. Rev. B*, 39:8556, 1989.
- [35] J. H. Smet, D. Weiss, R. H. Blick, G. Lütjering, K. von Klitzing, R. Fleischmann, R. Ketzmerick, T. Geisel, and G. Weimann. Magnetic focusing of composite fermions through arrays of cavities. *Phys. Rev. Lett.*, 77:2272, 1996.
- [36] R. Lassnig. Remote ion scattering in GaAs-AlGaAs heterostructures. *Solid State Communications*, 65:765, 1988.
- [37] V. Umansky, R. de Picciotto, and M. Heiblum. Extremely high-mobility two dimensional electron gas: Evaluation of scattering mechanism. *Appl. Phys. Lett.*, 71:683, 1997.
- [38] V. Umansky, M. Heiblum, Y. Levinson, J. H. Smet, J. Nübler, and M. Dolev. MBE growth of ultra-low disorder 2DEG with mobility exceeding $35 \times 10^6 \text{ cm}^2/\text{Vs}$. *Journal of Crystal Growth*, 311:1658, 2009.
- [39] M. A. Topinka, B. J. LeRoy, R. M. Westervelt, S. E. J. Shaw, R. Fleischmann, E. J. Heller, K. D. Maranowski, and A. C. Gossard. Coherent branched flow in a two-dimensional electron gas. *Nature*, **410**:183, 2001.
- [40] M. P. Jura, M. A. Topinka, L. Urban, A. Yazdani, H. Shtrikman, L. N. Pfeiffer, K. W. West, and D. Goldhaber-Gordon. Unexpected features of branched flow through high-mobility two-dimensional electron gas. *Nature Physics*, **3**:841, 2007.
- [41] Jiří Vaniček and Eric J. Heller. Uniform semiclassical wave function for coherent two-dimensional electron flow. *Phys. Rev. E*, 67:016211, 2003.
- [42] P. T. Coleridge. Small-angle scattering in two-dimensional electron gas. *Phys. Rev. B*, 44:3793, 1991.

- [43] J. Spector, H. L. Störmer, K. W. Baldwin, L. N. Pfeiffer, and K. W. West. Electron focusing in two-dimensional systems by means of an electrostatic lens. *Appl. Phys. Lett.*, 56:1290, 1990.
- [44] D. Maryenko, J. Metzger, F. Ospald, R. Fleischmann, V. Umansky, K. von Klitzing, and J. H. Smet. Evidence for the branch formation of the electron flow in DC transport experiment. *to be published*.
- [45] Katherine E. Aidala, R. E. Parrott, T. Kramer, E. J. Heller, R. M. Westervelt, M. P. Hanson, and A. C. Gossard. Imaging magnetic focusing of coherent electron waves. *Nature Physics*, 3:464, 2007.
- [46] H. Linke, L. Christensson, P. Omling, and P. E. Lindelof. Stability of classical electron orbits in triangular electron billiards. *Phys. Rev. B*, 56:1440, 1997.
- [47] L. Christensson, H. Linke, P. Omling, P. E. Lindelof, I. V. Zozulenko, and K-F. Berggren. Classical and quantum dynamics of electrons in open equilateral triangular billiards. *Phys. Rev. B*, 57:12306, 1998.
- [48] P. Boggild, A. Kristensen, and P. E. Lindelof. Magnetic focusing in triangular electron billiards. *Phys. Rev. B*, 59:13067, 1999.
- [49] Charls Kittel. *Introduction to Solid State Physics*. Wiley & Sons, 1995.
- [50] Frank Stern. Polarizability of a two-dimensional electron gas. *Phys. Rev. Lett.*, 18:546, 1967.
- [51] Alexander L. Fetter. Electrodynamics of a layered electron gas. I. single layer. *Annals of Physics*, 81:367 – 393, 1973.
- [52] S. A. Mikhailov. *Edge and Inter-Edge Magnetoplasmons in Two-Dimensional Electron Systems*, volume 236 of *Horizons in World Physics*. Nova Science Publishers, 1990.
- [53] V. A. Volkov and S. A. Mikhailov. *Electrodynamics of Two-dimensional Electron Systems in High Magnetic Fields*, volume 27 of *Modern Problems in Condensed Matter Physics*, chapter 15. North-Holland, 1991.
- [54] R. H. Ritchie. Plasma losses by fast electrons in thin films. *Phys. Rev.*, 106:874, 1957.
- [55] I. V. Kukushkin, V. M. Muravev, J. H. Smet, M. Hauser, W. Dietsche, and K. von Klitzing. Collective excitations in two-dimensional electron stripes: Transport and optical detection of resonant microwave absorption. *Phys. Rev. B*, 73:113310, 2006.
- [56] I. V. Kukushkin, J. H. Smet, S. A. Mikhailov, D. V. Kulakovskii, K. von Klitzing, and W. Wegscheider. Observation of retardation effects in the spectrum of two-dimensional plasmons. *Phys. Rev. Lett.*, 90:156801, 2003.
- [57] I. L. Aleiner and L. I. Glazman. Novel edge excitations in two-dimensional electron liquid in magnetic field. *Phys. Rev. Lett.*, 72:2935, 1994.

- [58] V. A. Volkov and S. A. Mikhailov. Edge magnetoplasmons - low-frequency weakly damped excitations in homogeneous two-dimensional electron systems. *Zh. Eksp. Teor. Fiz.*, 94:217, 1988.
- [59] V. A. Volkov and S. A. Mikhailov. Edge magnetoplasmons: low frequency weakly damped excitations in inhomogeneous two-dimensional electron systems. *Sov. Phys. JETP*, 67:1639, 1988.
- [60] I. L. Aleiner, Dongxiao Yue, and L. I. Glazman. Acoustic excitations of a confined two-dimensional electron liquid in a magnetic field. *Phys. Rev. B*, 51:13467, 1995.
- [61] I. V. Kukushkin, J. H. Smet, V. A. Kovalskii, S. I. Gubarev, K. von Klitzing, and W. Wegscheider. Spectrum of one-dimensional plasmons in a single stripe of two-dimensional electrons. *Phys. Rev. B*, 72:161317, 2005.
- [62] S. A. Mikhailov and N. A. Savostianova. Microwave response of a two-dimensional electron stripe. *Phys. Rev. B*, 71:035320, 2005.
- [63] Peter Y. Yu and Manuel Cardona. *Fundamentals of Semiconductors*. Springer, 1999.
- [64] H. L. Störmer and W.-T. Tsang. Two-dimensional hole gas at a semiconductor heterojunction interface. *Appl. Phys. Lett.*, 36:685, 1980.
- [65] H. L. Stormer, Z. Schlesinger, A. Chang, D. C. Tsui, A. C. Gossard, and W. Wiegmann. Energy structure and quantized hall effect of two-dimensional holes. *Phys. Rev. Lett.*, 51:126, 1983.
- [66] J. P. Lu, J. B. Yau, S. P. Shukla, M. Shayegan, L. Wissinger, U. Rössler, and R. Winkler. Tunable spin-splitting and spin-resolved ballistic transport in GaAs/AlGaAs two-dimensional holes. *Phys. Rev. Lett.*, 81:1282, 1998.
- [67] L. P. Rokhinson, V. Larkina, Y. B. Lyanda-Geller, L. N. Pfeiffer, and K. W. West. Spin separation in cyclotron motion. *Phys. Rev. Lett.*, 93:146601, 2004.
- [68] J. P. Eisenstein and A. H. MacDonald. Bose-Einstein condensation of excitons in bilayer electron systems. *Nature*, 432:691, 2004.
- [69] S. Schmult, private communication.
- [70] A. Ohtomo and H. Y. Hwang. A high-mobility electron gas at the LaAlO₃/SrTiO₃ heterointerface. *Nature*, 427:423, 2004.
- [71] S. Thiel, G. Hammerl, A. Schmehl, C. W. Schneider, and J. Mannhart. Tunable quasi-two-dimensional electron gases in oxide heterostructures. *Science*, 313:1942, 2006.
- [72] A. D. Caviglia, S. Gariglio, N. Reyren, D. Jaccard, T. Schneider, M. Gabay, S. Thiel, G. Hammerl, J. Mannhart, and J.-M. Triscone. Electric field control of the LaAlO₃/SrTiO₃ interface ground state. *Nature*, 456:624, 2008.

- [73] A. Tsukazaki, A. Ohtomo, T. Kita, Y. Ohno, H. Ohno, and M. Kawasaki. Quantum hall effect in polar oxide heterostructures. *Science*, 315:1388, 2007.
- [74] A. Tsukazaki and M. Kawasaki, private communication.
- [75] Liying Jiao, Li Zhang, Xinran Wang, Georgi Diankov, and Hongjie Dai. Narrow graphene nanoribbons from carbon nanotubes. *Nature*, 458:877, 2009.
- [76] M. Hong, J. Kwo, A. R. Kortan, J. P. Mannaerts, and A. M. Sergent. Epitaxial Cubic Gadolinium Oxide as a Dielectric for Gallium Arsenide Passivation. *Science*, 283:1897, 1999.
- [77] R. A. McKee, F. J. Walker, M. Buongiorno Nardelli, W. A. Shelton, and G. M. Stocks. The interface phase and the schottky barrier for a crystalline dielectric on silicon. *Science*, 300:1726, 2003.
- [78] Z. P. Wu, W. Huang, K. H. Wong, and J. H. Hao. Structural and dielectric properties of epitaxial SrTiO₃ films grown directly on GaAs substrates by laser molecular beam epitaxy. *J. Appl. Phys.*, 104:054103, 2008.
- [79] Y. R. Ryu, S. Zhu, J. D. Budai, H. R. Chandrasekhar, P. F. Miceli, and H. W. White. Optical and structural properties of ZnO films deposited on GaAs by pulsed laser deposition. *J. Appl. Phys.*, 88:201, 2000.
- [80] J.F. Whitaker, R. Sobolewski, D.R. Dykaar, T.Y. Hsiang, and G.A. Mourou. Propagation model for ultrafast signals on superconducting dispersive striplines. *IEEE Transactions on Microwave Theory and Techniques*, 36:277, 1988.
- [81] D.S. Phatak and A.P. DeFonzo. Dispersion characteristics of optically excited coplanar striplines: Pulse propagation. *IEEE Transactions on Microwave Theory and Techniques*, 38:654, 1990.
- [82] G. Hasnain, A. Dienes, and J. R. Whinnery. Dispersion of picosecond pulses in coplanar transmission lines. *IEEE Transactions on Microwave Theory and Techniques*, 34:738, 1986.

Acknowledgements

I would like to thank Prof. Dr. Klaus von Klitzing for welcoming me in his department and for his continuous interest in progress of the work. I am indebted to Dr. Jurgen H. Smet, who was my direct supervisor, for giving me interesting research topic, for providing all necessary equipment for the experiment, for discussions on various topics, which concerned not only the physics, and for giving me the chance to work independently. Few questions of him pushed me to think beyond my project and to develop own ideas for experiments. Both Dr. Jurgen H. Smet and Prof. Dr. Klaus von Klitzing gave an opportunity to participate on several conferences and to visit other labs. I would like to thank them also for their support of my future research plans. And I'm looking forward to collaborating with them. I thank Prof. Dr. Harald Giessen who kindly agreed to co-advise the thesis.

This work would not be possible without the support of:

- Jakob Metzger and Dr. Ragnar Fleischmann (Max-Planck-Institute for Dynamics and Self-Organization in Göttingen). I enjoyed the collaboration with them. They were very much interested in the experimental results of ballistic transport in the corner device. Their theoretical considerations and numerical simulations completed the part of the thesis on ballistic transport in the corner device.
- Dr. Bernd Rosenow (Max Planck Institute for Solid State Research) and Dr. Sergey Mikhailov (now Augsburg University). I profited from the discussion with them on plasmon excitations and was glad to get suggestions for data analysis.
- Frank Ospald, whom I know since the studies at Munich University. I was glad to have shared with him both the lab and the office. His friendship and his sense of humor are invaluable.
- Stefan Schmult, Myrsini Lafkioti, Andre Schwagmann and Eleonora Storace. I enjoyed extensive discussions about life, science, etc. They've been a good company both in the institute and beyond.
- Manfred Schmid, Ingo Hagel and Steffen Wahl. A great bunch of people, whose technical support was much valued in the lab.
- Monika Riek, Achim Güth. They were always ready to help in the cleanroom and were busy with the sample preparations at the final stage of my work.
- Ulrike Waizmann. She did a fabulous job on fabricating the e-beam structures.

- Frank Schartner and Benjamin Stuhlhofer from the Technology Service group. Their expertise on the bonding technique made it possible to controllably apply the silver epoxy droplets with the size of 20 μm and less with a 100% yield.

I thank my parents and my brother for supporting me morally throughout the extend of this thesis. I owe my special gratitude to my girlfriend Rita for her love, for her patient, for an always good piece of advise and for her endless support of my plans.

Curriculum Vitae

Persönliche Daten

Name Denis Maryenko
Geburtsdatum 10. Juni 1977
Geburtsort Kiew, Ukraine

Ausbildung

1991-1994 Naturwissenschaftliche Schule No.145, Kiew
Allgemeine Hochschulreife

09/1994-04/1996 **Taras Schewtchenko Universität, Kiew**

05/1997-05/1998 Studienkolleg bei den Universitäten des Freistaates Bayern

09/1998-04/2003 **Ludwig-Maximilians-Universität München**
Diplom in Physik
*Experiments in Solid State NMR in Dipolar Crystals for
Quantum Computation*

04/2002-04/2003 **Ginzton Labor, Stanford Universität**
wissenschaftlicher Mitarbeiter bei Prof. Y. Yamamoto

seit 09/2003 **Max Planck Institut für Festkörperforschung, Stuttgart**
Promotion in Physik bei Prof. Klaus v. Klitzing